Università degli Studi di Ferrara

DOTTORATO DI RICERCA IN
SCIENZE CHIMICHE

CICLO XXVIII

COORDINATORE Prof. Carlo Alberto Bignozzi

Surface and interface modification of nanostructured hematite for solar water splitting

Settore Scientifico Disciplinare CHIM/03

Dottorando
Dott. Dalle Carbonare Nicola

Tutore
Dott. Argazzi Roberto

Anni 2013/2015

CONTENTS

7.4 Photoelectrochemical properties…….. ……152
7.5 Impedance analysis of the un-modified and 5%-Ti modified electrodes… ……154
7.6 Conclusions…… ……158
7.7 References…… ……159

CHAPTER 8. PLD deposition of transparent iron oxide catalyst for the water oxidation reaction…… ……

8.1 Introduction …….. ……161
8.2 Amorphous iron oxide pulsed laser deposition …….. ……163
8.3 Morphological investigation..…… ……..……164
8.4 Optical quantum confinement effect …… ……166
8.5 Electrochemical characterization of iron oxide samples…..... ……168
8.6 Hematite photoanodes modified with PLD-deposited iron oxides…… ……169
8.7 Conclusions…….. ……170
8.8 References…… ……172

CHAPTER 9. Characterization techniques: experimental details and theoretical aspects…… ……

9.1 Electrochemical and photoelectrochemical setup ……... ……175
9.2 DC photoelectrochemical techniques…… ……177
9.3 Photoaction spectra: IPCE and APCE..…… ……..……178
9.4 AC technique: Electrochemical Impedance Spectroscopy …….. ……180
9.5 Optical absorption and emission spectroscopy…….. ……186
9.6 Nanosecond laser flash photolysis…….. ……187
9.7 Investigation of morphology and crystalline structure…….. ……188
9.8 Determination of roughness factor…….. ……189
9.9 List of materials employed in the samples preparation…… ……190
9.10 References……..……..……..

ABSTRACT

Inspired by nature and pursuing the concrete option of an economy based on hydrogen as a fuel for the everyday energetic consumption, scientists from different fields have based their research activity on the possibility to decompose water in its elementary constituents using only sunlight as external energy supply. In the last four decades there has been an exciting growth of knowledge about semiconductor physico-chemical properties with regard to their leading role in photo-electrochemical (PEC) device able to convert light into chemical energy stored in the bond between hydrogen atoms, in a more elegant and powerful way with respect to conventional photovoltaic technology. Metal oxides have been from the beginning the most examined materials for PEC application due to their great stability in aqueous solution and to the easy access to various nanostructured morphologies that guarantee good optical and catalytic properties. During my PhD I have investigated the charge transfer dynamics in hematite (α-Fe_2O_3) thin film electrodes modified with iron oxide-based structures by using mainly both AC/DC electrochemical techniques in combination with laser photolysis and spectroscopy for the morphological characterization. Hematite is a well known semiconductor able to drive the bias-assisted water oxidation reaction at its surface, although important drawbacks related to its poor charge transport properties have limited the overall efficiency achieved so far. Using cheap and environmentally safe starting materials and solution-based procedure for all the preparative and modification steps, we have been able to efficiently modify mesoporous iron oxide films achieving excellent performances in term of photocurrent generation and stability. Mechanistic and kinetic insights about the effect of an iron-based water oxidation catalyst and of a thin underlayer are fundamental to a deeper understanding of the photogenerated carriers fate for a more useful design of these electrodes. Besides electrochemical performance, the possibility to obtain efficient devices with common and simple procedures is a key point for a future and concrete implementation of this technology for a large scale application.

RIASSUNTO

La possibilità di produrre idrogeno dalla scissione fotoindotta dell'acqua imitando ciò che la natura fa in ogni istante attraverso la fotosintesi, senza la necessità quindi di utilizzare alcuna fonte aggiuntiva di energia esterna, ha suscitato enorme interesse nella comunità scientifica, stimolata dal sogno di poter sviluppare una società che utilizzi idrogeno come fonte energetica primaria. Negli ultimi quattro decenni abbiamo assistito ad una straordinaria accelerazione nella razionalizzazione delle proprietà chimico-fisiche di materiali semiconduttori su cui si basano sistemi foto-elettrochimici adibiti alla conversione della luce solare in energia chimica e non in corrente elettrica da utilizzare istantaneamente, come nei comuni dispositivi fotovoltaici. Sin dai primi esperimenti di fotolisi, gli ossidi metallici sono stati i protagonisti di tali dispostivi, grazie alla loro eccellente stabilità in soluzioni acquose e alla possibilità di ottenere facilmente morfologie nano-strutturate che hanno garantito un notevole incremento in termini di assorbimento della radiazione luminosa e di capacità catalitiche nei confronti delle reazioni di riduzione ed ossidazione dell'acqua. Nel corso del mio Dottorato di Ricerca ho studiato le dinamiche di trasferimento di carica di elettrodi di ossido ferrico modificati con strutture sia amorfe che cristalline a base di ferro utilizzando, per la caratterizzazione, principalmente tecniche elettrochimiche sia in corrente continua che alternata, affiancate da spettroscopie di superficie e laser per una completa descrizione delle proprietà catalitiche. L'ossido ferrico è un materiale notoriamente impiegato per la foto-ossidazione dell'acqua, anche se la sua scarsa capacità di condurre e trasferire carica richiedono l'applicazione di un potenziale esterno. Utilizzando materiali non nocivi ed economici e semplici procedure in soluzione per la preparazione dei campioni e per le successive modifiche, siamo stati in grado di migliorare le prestazioni degli elettrodi sia in termini di foto-correnti generate che di stabilità, razionalizzando al contempo aspetti meccanicistici coinvolti nei processi di trasferimento di carica responsabili dell'ossidazione dell'acqua.

LIST OF SYMBOLS AND ABBREVIATIONS

α	Wavelength absorption coefficient [L mol^{-1} dm^{-1}]
α^{-1}	Light penetration depth [nm]
AACVD	Aerosol Assisted Chemical Vapour Deposition
AC	Alternate Current
AFM	Atomic Force Microscopy
AM 1.5 G	Air Mass 1.5 Global condition: irradiance of sunlight incident on a clear day upon a sun-facing 37°-tilted surface with the sun at an angle of 41.81° above the horizon, correspond to an illumination intensity of 100 mW cm^{-2} (1 sun)
APCE	Absorbed Photon-to-Current Efficiency
APCVD	Atmosferic Pressure CVD
B.E.	Binding Energy [eV]
CB	Conduction band
CT	Charge Transfer
CV	Cyclic Voltammetry
CVD	Chemical Vapor Deposition
ΔE_{ph}	Photopotential
$\Delta_r G^0$	Standard Gibbs free energy
DC	Direct Current
E_C	Conduction band edge energy
E_F	Fermi level Energy
E_g	Band gap Energy
$E_{red\text{-}ox}$	Electrochemical potential
E_V	Valence band edge energy
$E^0_{H2/H+}$	Water reduction potential
$E^0_{O2/OH-}$	Water oxidation potential
EIS	Electrochemical Impedance Spectroscopy
FTO	Fluorine Tin-doped Oxide
i_{ph}	Photocurrent
IHP	Inner Helmholtz Plane
IPCE	Incident Photon-to-Current Conversion Efficiency
ITO	Indium Tin Oxide
L_h	Hole diffusion length [nm]
L_e	Electron diffusion length [nm]
LFP	Laser Flash Photolysis
LHE	Light Harvesting Efficiency

MS	Mott Schottky
NHE	Normal Hydrogen Electrode
OEC	Oxygen Evolving Catalyst
OER	Oxygen Evolving Reaction
OHP	Outer Helmholtz Plane
PEC	Photoelectrochemical
PIA	Photoinduced Absorption
PL	Photoluminescence
PLD	Pulsed Laser Deposition
PMOD	Photo-chemical Metal-Organic Deposition
PV	Photovoltaic
RHE	Reversible Hydrogen Electrode
SCE	Saturated Calomel Electrode
SCLJ	Semiconductor-liquid junction
SEM	Scanning Electron Microscopy
SILAR	Successive Ionic Layer Adsorption and Reaction
TEOS	Tetraethyl orthosilicate
TAS	Transient Absorption Spectroscopy
V or $V_{applied}$	Applied bias potential
V_{fb}	Flat band potential
VB	Valence band
J-V	Current-voltage
W_{SC}	Space charge layer width
XRD	X-Ray Diffraction
XPS	X-Ray Photoelectron Spectroscopy

LIST OF PUBLICATIONS

Doping or passivation? Effect of titanium(IV) on the photoelectrochemical performance of mesoporous hematite electrodes for solar water oxidation.
N. Dalle Carbonare, P. Rudatis, S. Berardi, S. Carli, R. Argazzi, S. Caramori and C. A. Bignozzi, *manuscript in preparation*.

A transparent water oxidation catalyst for photoanodes functionalization.
M. Orlandi, N. Dalle Carbonare, A. Mazzi, Z. El Koura, N. Bazzanella, S. Caramori, N. Patel, C. A. Bignozzi and A. Miotello, *manuscript in preparation*.

Heterogeneous and homogeneous routes in water oxidation catalysis starting from Cu(II) complexes with tetraaza macrocyclic ligands.
A. Prevedello, I. Bazzan, N. Dalle Carbonare, A. Giuliani, S. Bhardwaj, C. Africh, C. Cepek, R. Argazzi, M. Bonchio, S. Caramori, M. Robert and A. Sartorel, *Chem.-Asian J.*, **2016**, DOI: 10.1002/asia.201501446R1.

Improvement of the electron collection efficiency in porous hematite using a thin iron oxide underlayer: towards efficient all-iron based photoelectrodes.
N. Dalle Carbonare, S. Carli, R. Argazzi, M. Orlandi, N. Bazzanella, A. Miotello, S. Caramori and C. A. Bignozzi, *Phys. Chem. Chem. Phys.,* **2015**, 17, 29661.

Molecular assemblies and nanostructured semiconductors for photoinduced water splitting.
S. Caramori, R. Argazzi, V. Cristino, N. Dalle Carbonare, F. Ronconi and C. A. Bignozzi, *La Chimica & l'Industria,* **2015**, *4*, 13.

Thinking about ‘rust’ not only as a waste.

N. Dalle Carbonare, *La Chimica & l’Industria,* **2014**, *3*, 48.

Hematite photoanodes modified with an Fe(III) water oxidation catalyst.

N. Dalle Carbonare, V. Cristino, S. Berardi, S. Carli, R. Argazzi, S. Caramori, L. Meda, A. Tacca and C. A. Bignozzi, *ChemPhysChem.,* **2013**, *15*, 1164.

LIST OF ORAL AND POSTER PRESENTATION

1st ENERCHEM Congress

Firenze (Italy) - February 2016

Poster presentation: “Split with rust! Modified hematite photoanodes for solar water splitting”

1st International Solar Fuels Conference / ISF-1-Young

Uppsala (Sweden) - April 2015

Flash and poster presentation: “All-iron modification of hematite electrodes for solar water splitting”

XIV Giornata della Chimica dell’Emilia Romagna

Parma (Italy) - December 2014

Oral presentation: “Charge separation dynamics in hematite electrodes modified with an iron oxide underlayer”. This presentation was awarded in *ex-aequo* as best flash presentation.

XIV SCI-S.A.Y.C.S.

Riccione (Italy) - October 2014

Oral presentation: “Split with us! Solar water splitting using semiconductor oxides”

XXV Congresso Nazionale della Società Chimica Italiana

Rende (Italy) - September 2014

Oral presentation: “Hematite photoanodes modified with a Fe(III) water oxidation catalyst”

65th Annual Meeting of the International Society of Electrochemistry

Lausanne (Switzerland) - September 2014

Poster presentation: “Hematite photoanodes modified with a Fe(III) water oxidation catalyst”

XIII Giornata della Chimica dell’Emilia Romagna

Bologna (Italy) – December 2013

Poster presentation: “Hematite photoanodes modified with a Fe(III) water oxidation catalyst”. This presentation was awarded in *ex-aequo* as best poster presentation.

CHAPTER 1

GENERAL INTRODUCTION

1.1 Climate change

Earth's climate has changed throughout history. In the last 650,000 years there have been seven cycles of glacial advance and retreat until the last ice age about 7,000 years ago, marking the beginning of human civilization. Most of these climate changes are attributed to very small variations in Earth's orbit that change the amount of solar energy our planet receives, but the current warming trend is of particular significance because most of it is very likely human-induced and proceeds at a rate that is unprecedented in the past 1300 years.[1]

In recent decades, changes in climate have caused impacts on natural and human systems on all continents and across the oceans, evidencing the sensitivity of natural and human systems to these alterations, regardless of their causes.

i) Earth has warmed since 1880, with all 10 of the warmest years occurring in the past 12 years and, although in the 2000's the solar output declined reaching a

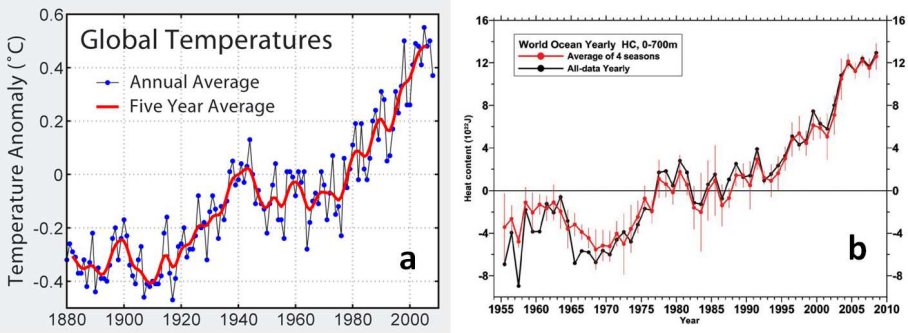

Figure 1.1. (a) Record of global average temperature anomalies (credits: NASA's Goddard Institute for Space Studies). (b) Yearly time series of ocean heat content (10^{+22} J) for the 0-700 m layer based on the all-data yearly fields and the average of the four seasonal yearly fields (from reference [3]).

minimum in the 2007-2009 period, the temperature continues to increase and shows an increase of approximately 1.0 °C since the early 20th century (Figure 1.1-a).[2]

ii) Oceans, storing more 90% of the energy accumulated in the planet, has warmed up by 0.11 °C per decade since 1970's (Figure 1.1-b).[3]

iii) The acidity of ocean water, due to the higher carbon dioxide concentration, has been increasing since the beginning of the Industrial Revolution with dramatic consequences on oceanic species: the pH has fallen by 0.1 units, that represents approximately a 30% increase in acidity. Estimations of future carbon dioxide levels, based on business as usual emission scenarios, indicate that by the end of this century the surface waters of the oceans could be nearly 150 percent more acidic, resulting in a pH that the oceans have not experienced for more than 20 million years. (Figure 1.2).[4]

iv) The continent of Antarctica has been losing about 134 billion metric tons of ice per year since 2002, while the Greenland ice sheet has been losing an estimated 287 billion metric tons per year.[6]

v) Over the period 1901 to 2010, global mean sea level rose by 0.19 meters. The rate of sea level rise since the mid-19th century has been larger than the mean rate during the previous two millennia.

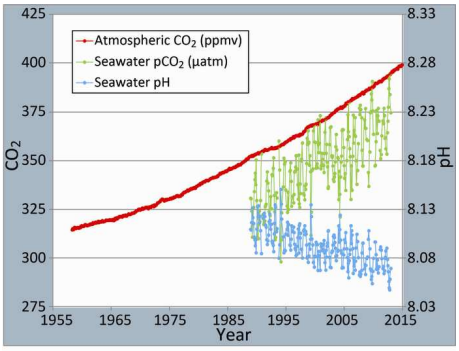

Figure 1.2. Correlation between rising levels of carbon dioxide (CO_2) in the atmosphere in Manua Loa and in the nearby ocean at Station Aloha with the pH of seawater (from reference [5]).

The scientific community agreed that the main cause of this constant and rapid warming of the Earth is due to an increase of the so-called 'greenhouse effect', directly linked to human activities. Greenhouse gases in the atmosphere absorb most of the thermal radiation emitted by the Earth's surface after the absorption of solar radiation and emit energy both upwards and downwards: the part radiated downwards is absorbed by the Earth's surface leading to a higher equilibrium temperature than if the atmosphere were absent. This effect is critical to support life in our planet. The four major gases contributing to the greenhouse effect on Earth are, by their percentage, water vapour, carbon dioxide, methane and ozone. Other anthropogenic greenhouse gases are N_2O and CFC's (chlorofluorocarbons). On Earth, human activities are inevitably changing the natural greenhouse effect. CO_2 is produced by fossil fuel burning, like coal and oil: this happens because the coal or oil burning process combines carbon with oxygen in the air to make CO_2. The industrial activities that our modern civilization depends upon have raised atmospheric carbon dioxide levels from 280 parts per million to 400 parts per million in the last 150 years. To a lesser extent, the clearing of land for agriculture, industry, and other human activities have increased concentrations of greenhouse gases (Figure 1.3).

There are no more doubts about the position of the scientific community on the subject: "*global climate change caused by human activities is occurring now, and it is a growing threat to society*".[7] The Intergovernmental Panel on Climate Change (IPCC), honoured with the 2007 Nobel Peace Prize which includes more than 1,300 scientists, has clearly

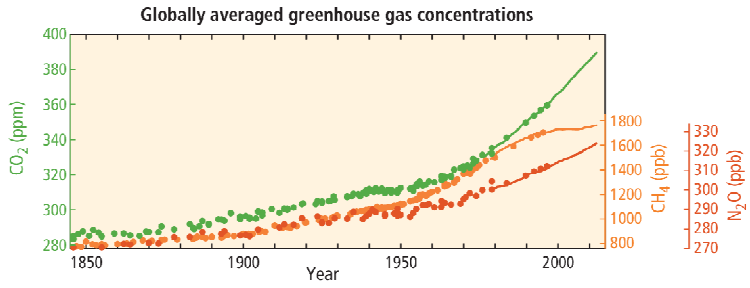

Figure 1.3. Atmospheric concentrations of the greenhouse gases carbon dioxide (CO_2, green), methane (CH_4, orange) and nitrous oxide (N_2O, red) determined from ice core data (dots) and from direct atmospheric measurements (lines) (from reference [8]).

stated that *"anthropogenic greenhouse gas emissions have increased since the pre-industrial era, driven largely by economic and population growth, and are now higher than ever. This has led to atmospheric concentrations of carbon dioxide, methane and nitrous oxide that are unprecedented at least in the last 800,000 years. Their effects, together with those of other anthropogenic drivers, have been detected throughout the climate system and are extremely likely to have been the dominant cause of the observed warming since the mid-20th century"*.[8] Moreover, they have a clear vision of what is going to happen in the future: "*Many aspects of climate change and associated impacts will continue for centuries, even if anthropogenic emissions of greenhouse gases are stopped. The risks of abrupt or irreversible changes increase as the magnitude of the warming increases*".[9] The IPCC strongly recommends in the above cited report the necessity of limiting warming to below 2 °C relative to pre-industrial levels: this achievement would require substantial emissions reduction over the next few decades and near zero emissions of CO_2 and other long-lived greenhouse gases by the end of the century to reduce climate risks in the 21st century and beyond.

On December 12th, 2015, during the UN Convention of the Climate Changes in Paris, the Conferences of the Party have adopted a protocol that follows the IPCC guidelines. 180 countries (which contribute to at least to the 95% of global emissions in 2012) voluntarily commit to reduce the CO_2 emission of about 8 $GtCO_2$ per year until 2020 and of 11 $GtCO_2$ until 2030. In particular, Europe has committed to reducing emissions by 40% by 2030 and it will have to identify the ways in which each of its member states must act on the areas of their respective competence. The purpose of mitigation is to *"keep the increase*

in global average temperature well below 2 degrees compared to pre-industrial levels and make efforts to limit temperature increase to 1.5 °C, acknowledging that this would significantly reduce the risks and the impacts of climate change".[10]

Both the politic and the scientific community play a fundamental role in the rescue of our planet by limiting the global energy consumption without repercussions on our economies and lifestyle, increasing the efficiencies of the infrastructures dedicated to energy production and distribution based on renewable, no-fossil and clean energy sources.

1.2 Global energy situation

The world energy consumption in 2012 was estimated in $5.6 \cdot 10^{20}$ joules. Although a slight decline was recorded in 2009 when, for the first time in 30 years, world energy consumption decreased as a result of the financial and economic crisis, energy consumption in the G20 area increased by more than 5% in 2010.

Fossil fuels (petroleum, natural gas and coal) continue to meet more than 80% of total primary energy demand and over 90% of energy-related emissions are due to CO_2, originating fossil-fuel combustion. Global emissions of carbon dioxide from the combustion of fossil fuels has reached 36 billion tons in 2013.[11] While smaller in magnitude and less long-lasting in the atmosphere (though with higher global warming potential), methane and nitrous oxide are other powerful greenhouse gases emitted by the energy sector.[12] Methane accounts for around 10% of energy sector emissions and originates mainly from oil and gas extraction, transformation and distribution. Much of the remainder is nitrous oxide emissions from energy transformation, industry, transport and buildings (Figure 1.4). Although the necessity to reduce the CO_2 emission is now mandatory without any further delay, energy production from fossil fuels will remain a necessity over the next decades because of a lack of infrastructures and technologies for the economically competitive harvesting of renewable energy sources. But, even if

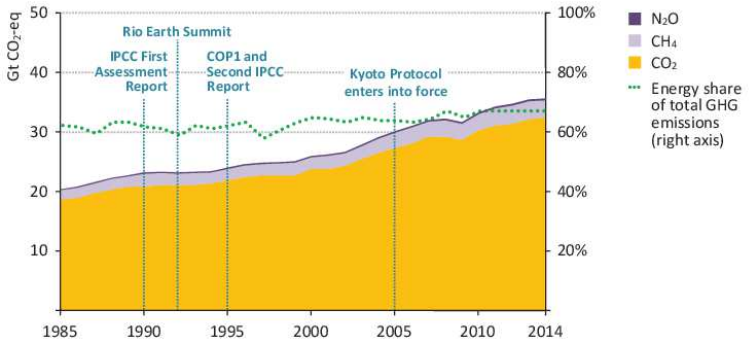

Figure 1.4. Global anthropogenic energy-related greenhouse-gas emissions by type (from reference [14]).

estimation about resources availability and recoverability are often highly uncertain,[13] fossil fuels stocks are limited and not naturally replenished on a human timescale. So, the necessity to find other forms of energy supply is not limited to a reduction in emission of greenhouse gases, but, in a longer perspective, to a sustainment of our economy and society. The use of low-carbon energy sources is expanding rapidly, and there are signs that growth in the global economy and energy-related emissions may be starting to decouple. The global economy grew by around 3% in 2014, but energy-related carbon dioxide emissions stayed flat: from the first time in at least 40 years such an outcome has occurred outside the economic crisis. An important change in the energy sector from 2014 to 2015 has been the rapid drop in world oil prices and, to a lesser extent, natural gas and coal prices. At the global level, lower fossil-fuel prices are likely to act as a form of economic stimulus. Data for 2014 indicate that global energy intensity decreased by 2.3% relative to the previous year, more than double the average rate of change over the last decade, but not for a reduction of global energy consumption, but as the result of energy efficiency improvements and structural changes in the global economy. Renewable and low-carbon technologies are becoming increasingly cost competitive in a bigger number of countries. Renewable-based power generation capacity is estimated to have increased by 128 GW in 2014, of which 37% is wind power, almost one-third solar power and more than a quarter from hydropower (Figure 1.5).[14] This amounted to more than 45% of world power generation capacity additions in 2014, consistent with the general upward trend in recent years, leaded by China, that remains the largest wind power market, with

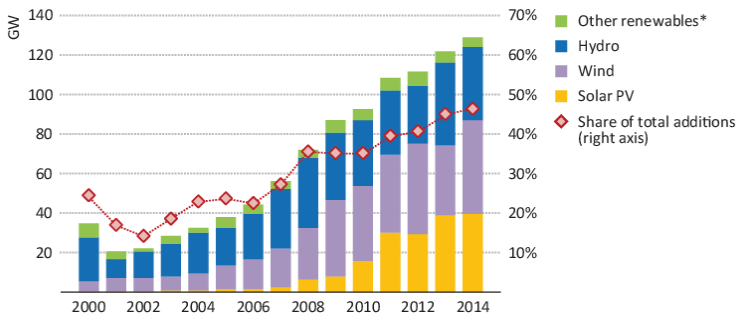

Figure 1.5. Global renewable-based power capacity additions by type and share of total capacity additions. * Includes geothermal, marine, bio-energy and concentrating solar power (from reference [14]).

20 GW of new capacity. Lower oil prices proved to be a challenge for other forms of renewable energy, including bio-fuels in transport and renewable heat, as

the latter competes directly with natural gas heating (the price of which is still, in many cases, linked to the oil price).

Nuclear power is the second-largest source of low-carbon electricity generation worldwide, after hydropower. China continues to lead in new capacity additions, with 28 GW under construction at the end of 2014, while plants with a combined capacity of 46 GW are under construction in Russia, India, Korea, United States and several other countries.

1.3 Solar energy

Among the different types of renewable sources, solar energy surely represents the most powerful and promising energy provider. The total solar energy absorbed by Earth's atmosphere, oceans and land masses is approximately $3.85 \cdot 10^{24}$ Joule per year: in 2002, this was more energy in one hour than the world used in one year. The potential solar energy that could be used by humans depends on the amount of irradiation near the surface, influenced by factors as geography, day and night alternation, cloud cover and land availability.

Photovoltaic (PV) cells and concentrating solar thermal power are active techniques to obtain electricity from solar energy. PV cells directly convert sunlight into electricity using the photovoltaic effect and are predominantly made of semiconductors such as crystalline silicon or various thin-film materials. The average efficiency of commercial silicon modules has improved in the last ten years by about 0.3% per year, reaching 16% in 2013. Modules are usually guaranteed for a lifetime of 25 years at minimum 80% of their rated output, and sometimes for 30 years at 70%.[15] Thin Film (TF) modules also saw increase in efficiencies, with commercial CdTe TF, reaching a remarkable 15%. In the last ten years, cumulative installed capacity has grown at an average rate of 49% per year and PV has become a mainstream electricity source thanks also to its scalability: PV cells can provide small amount of power for various application (e.g. outdoor illumination) as well as grid-connected PV systems can range from few kilowatts for domestic use up to megawatts for injection into electric grid (Figure 1.6). Concentrating Solar Power (CSP) systems use lenses or mirrors to focus a large area of sunlight into a small beam that is used to heat a working fluid that, ultimately, drive a water turbine to produce electricity.
These technologies can instantaneously produce electricity or hear that, unfortunately, can not be easily stored and moved where they are necessary. An attractive option is represented by the possibility to generate molecular hydrogen (H_2) using solar energy as energetic input, obtaining not only a precious chemical for various important synthetic procedure (e.g. ammonia synthesis), but also a powerful and clean chemical vector.

Figure 1.6. Satellite view of Topaz Solar Farm, a 550-megawatt photovoltaic power station made up of 9 million CdTe PV modules in San Luis Obispo County, California.

1.4 Hydrogen as a fuel?

Hydrogen is a non-toxic, colourless and odourless diatomic gas. It is a zero-emission fuel, forming only water vapour and warm air when burned with oxygen, and the most energy-dense fuel per mass: the energy in 1 kg of hydrogen gas contains about the same as the energy in 1 gallon of gasoline. Like oil and natural gas, hydrogen can be transported via pipeline or be stocked under pressure in tanks and then directly burned with oxygen to produce heat or be converted into electricity in fuel cells. NASA has used hydrogen for space flight since the 1950s and recently some automotive company have launched in the market electrical car models based on fuel cell technology (e.g. Toyota, Hyundai).[16] Although the development of a hydrogen-based economy is really attractive there are many several aspects that are limiting its widespread use in the everyday life, aspects that are mainly connected to the hydrogen production (still related to fossil sources) and storage, in particular for mobile application.

1.4.1 Fuel cells

Fuel cells are energy conversion devices that can efficiently convert hydrogen into electricity: they can power almost any portable application that typically uses batteries, from hand-held devices to portable generators, and also our trans-portation, including personal vehicles, trucks, buses, as well as provide auxiliary power to traditional transportation technologies. A single fuel cell consists of an electrolyte sandwiched between two electrodes, an anode and a cathode (Figure 1.7). Bipolar plates on either side of the cell help distributing gases and serve as current collectors. Hydrogen gas flows through channels to the anode, where a catalyst causes the hydrogen molecules to separate into protons and electrons. The membrane allows only the protons to pass through it. While the protons are conducted through the membrane to the other side of the cell, the stream of negatively-charged electrons follows an external circuit to the cathode. This flow of electrons is electricity that can be used to do work, such as power a

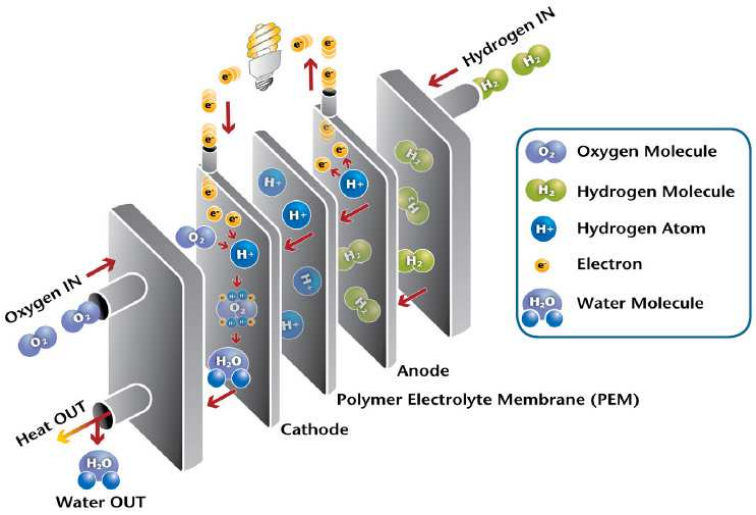

Figure 1.7. Schematic view and working based principles of a Polymer Electrolyte Membrane (PEM) fuel cell.

motor. On the other side of the cell, air flows through channels to the cathode. When the electrons reach the cathode, they react with oxygen from air and the hydrogen protons (which have moved through the membrane) at the cathode to form water. This is an exothermic reaction, generating heat that can be used outside the fuel cell.

Hydrogen-powered fuel cells are not only pollution-free, but can also have more than two times the efficiency of traditional combustion technologies. The gasoline engine in a conventional car is less than 20% efficient in converting the chemical energy of gasoline into power that moves the vehicle, under normal driving conditions. Hydrogen fuel cell vehicles, which use electric motors, are much more energy efficient and use 40-60% of the fuel's energy, corresponding to more than a 50% reduction in fuel consumption, compared to a conventional vehicle with a gasoline internal combustion engine. The power produced by a fuel cell depends on several factors, including the fuel cell type, size, temperature at which it operates, and pressure at which gases are supplied. To increase the voltage, individual fuel cells are combined in series to form a stack. Depending on the application, a fuel cell stack may contain only a few or as many as hundreds of individual cells layered together. This "scalability" makes fuel cells ideal for a wide variety of applications, from laptop computers (20-50 W) to houses (1-5 KW), vehicles (50-125 kW), and central power generation (1- 200 MW or more).[17]

Fuel cell systems must be cost-competitive with, and perform as well or better than, traditional power technologies over the life of the system. Ongoing research is focused on identifying and developing new materials that will reduce the cost and extend the life of fuel cell stack components including membranes, catalysts, bipolar plates, and membrane-electrode assemblies.

1.4.2 Hydrogen storage

The storage of hydrogen is nowadays the main issue that is slowing down the development of a hydrogen based society, especially for mobile applications. Although hydrogen possesses the highest energy density per weight, it has very a low energy density by volume as a gas at ambient conditions (4 times less than gasoline for example). This is a challenging aspect because it makes difficult to store in large quantities hydrogen without taking up a significant amount of space. Hydrogen can be physically stored as compressed hydrogen gas in high pressure tanks (up to 700 bar) or as cryogenic hydrogen (cooled to -253 °C, at pressures of 6-350 bar) in insulated tanks. Increasing the pressure of a gas increase both the amount of energy per volume and the weight of the tank. Using currently available high-pressure tank storage technology, placing a sufficient quantity of hydrogen onboard a vehicle to provide a 300-mile driving range (which is generally regarded as the minimum for widespread public acceptance) would require a very large tank, larger than the trunk of a typical automobile, reducing not only the cargo available space but also the fuel economy. Moreover, considerable energy costs are necessary to maintain high pressure and low temperature in the tank. Alternatively, hydrogen can be stored on the surface of solids by adsorption either as hydrogen molecules (H_2) or hydrogen atoms (H) or within a solid, being incorporated in the lattice frameworks after the molecules dissociation. This method enable to store larger quantities of hydrogen in smaller volumes at low pressure and at temperatures close to room temperature: materials under main investigation are metal organic frameworks (MOF),[18] carbon nanostructures and complex hydrates.[19] Finally, hydrogen

can be forced to react with other elements and stored in hydrides or hydrogen rich compounds, easier to store and transport: limitations are due to the high pressure and temperature conditions required to stored and the released hydrogen.[20,21]

1.4.3 Hydrogen production

Hydrogen is not available as a free gas but it is locked up in enormous quantities in water (H_2O), hydrocarbons (such as methane), and other organic matter. One of the challenges of using hydrogen as a fuel relates with its efficient extraction from these compounds. It can be produced using different resources including fossil fuels, such as coal, natural gas, and biomass or using nuclear energy. The environmental and health benefits are even greater when hydrogen is produced from low- or zero-emission renewable sources, such as wind, solar, geothermal, and hydroelectric power, to split water. Currently, the majority of hydrogen (~95%) is produced from fossil fuels by natural gas reforming and coal gasification with only a small quantity by other routes such as biomass gasification or electrolysis of water.[22]

The production of hydrogen from natural gas is the cheapest and most common procedure to obtain hydrogen nowadays and represents 38% of the world's hydrogen production, with an approximately 80% efficiency. Syngas, a mixture of hydrogen, carbon monoxide, and a small amount of carbon dioxide, is created by reacting natural gas with high-temperature steam (700–1100 °C) (Reaction 1.1).

$$CH_4 + H_2O \rightarrow CO + 3H_2 \quad (1.1)$$

The carbon monoxide is reacted with water to produce additional hydrogen through the lower-temperature, exothermic, water gas shift reaction (Reaction 1.2).

$$CO + H_2O \rightarrow CO_2 + H_2 \quad (1.2)$$

The disadvantage of this process is the by-production of CO, CO_2 and other greenhouse gases: moreover, although the water gas shift reaction provides energy to maintain the process, the additional heat is generally supplied by burning some portion of methane.

Gasification is a process in which coal or biomass is converted into gaseous components by applying heat under pressure and in the presence of air/oxygen and steam. A subsequent series of chemical reactions produces a synthesis gas, which is then reacted with steam to produce a gas stream with an increased hydrogen concentration which can be separated and purified. With carbon capture and storage, hydrogen can be produced directly from coal with near-zero greenhouse gas emissions. Since growing biomass consumes CO_2 from the atmosphere, producing hydrogen through biomass gasification releases near-zero net greenhouse gases.

Electrolysis uses an electric current to split water into hydrogen and oxygen. This source of hydrogen is by far the most expensive since the energy input required for water splitting is higher than the energy that could be obtained from the produced hydrogen and it counts for only the 4% of the world's hydrogen production. But, due to the use of water as main reactant and the production of oxygen as the only by-product, water splitting reaction has attracted the interest of the scientific community. The electricity required can be generated using any of a number of resources: however, to minimize greenhouse gas emissions, electricity generation using renewable energy technologies, such as wind, solar, geothermal, and hydroelectric power is preferred.

Hydrogen can be produced directly from water using some semiconductor material that, after the absorption of light, are able to split water constituents without any external assistance. This approach will be discussed in detail in the next chapter.

Certain microbes, such as green algae and cyanobacteria, produce hydrogen by splitting water in the presence of sunlight as a by-product of their natural metabolic processes. It seems that H_2 production through this route is now economically feasible by surpassing the 7–10 percent energy efficiency of the conversion of sunlight into hydrogen, with a hydrogen production rate of 10-12 ml per litre of culture per hour.[23]

The greatest technical challenge for the hydrogen production is cost reduction. As regards transportation, the cost of hydrogen must be in the range of $2-$4/gallon of gasoline

equivalent. Some technologies, such as steam methane reforming, are well-developed and related researches are focused on reducing capital equipment, operations, and maintenance costs as well as improving carbon sequestration technology to ensure that coal-based hydrogen production leads to almost no greenhouse gas emissions. Others technologies, as such biological and photoelectrochemical water splitting, are in early stages of laboratory development but are considered potential pathways as long-term scenario.

1.5 References

1 http://climate.nasa.gov/evidence/ (visited on December 14th, 2015).

2 https://www.ncdc.noaa.gov/indicators/ (visited on December 14th, 2015).

3 S. Levitus, J. I. Antonov, T. P. Boyer, R. A. Locarnini, H. E. Garcia and A. V., *Geophys. Res. Lett., 2009*, *36*, L07608.

4 http://www.pmel.noaa.gov/co2/story/What+is+Ocean+Acidification%3F (visited on December 16th, 2015).

5 http://www.pmel.noaa.gov/co2/file/Hawaii+Carbon+Dioxide+Time-Series (visited on December 17th 2015).

6 http://climate.nasa.gov/vital-signs/land-ice/ (visited on December 14th, 2015).

7 AAAS Board Statement on Climate Change (2006).

8 IPCC Climate Change 2014 Synthesis Report Summary for Policymakers, page 4.

9 *ivi*, page 16.

10 http://unfccc.int/resource/docs/2015/cop21/eng/l09r01.pdf.

11 C. Le Quéré, G. P. Peters, R. J. Andres, R. M. Andrew, T. A. Boden, P. Ciais, P. Friedlingstein, R. A. Houghton, G. Marland, R. Moriarty, S. Sitch, P. Tans, A. Arneth, A. Arvanitis, D. C. E. Bakker, L. Bopp, J. G. Canadell, L. P. Chini, S. C. Doney, A. Harper, I. Harris, J. I. House, A. K. Jain, S. D. Jones, E. Kato, R. F. Keeling, K. Klein Goldewijk, A. Körtzinger, C. Koven, N. Lefèvre, F. Maignan, A. Omar, T. Ono, G. H. Park, B. Pfeil, B. Poulter, M. R. Raupach, P. Regnier, C. Rödenbeck, S. Saito, J. Schwinger, J. Segschneider, B. D. Stocker, T. Takahashi, B. Tilbrook, S. van Heuven, N. Viovy, R. Wanninkhof, A. Wiltshire and S. Zaehle, *Earth Syst. Sci. Data* **2014**, *6*, 235.

12 CH_4 has a global warming potential of 28 to 30 times that of CO_2, while the global warming potential of N_2O is 265 higher than that of CO_2.

13 J. Speirs, C. McGlade and R. Slade, *Energy Policy,* **2015**, *87*, 654.

14 International Energy Agency, *World Energy Outlook Special Report*, **2014**.

15 International Energy Agency, *Technology Roadmap Solar Photovoltaic Energy*, **2014.**

16 https://ssl.toyota.com/mirai/][https://www.hyundaiusa.com/tucsonfuelcell/ (Visited on December 20th 2015).

17 http://www.afdc.energy.gov/fuels/hydrogen (Visited on December 20th 2015).

18 M. P. Suh, H. J. Park, T. K. Prasad and D.-W. Lim, *Chem. Rev.,* **2012**, *112*, 782.

19 A. M. Seayad and D. M. Antonelli, *Adv. Mater.,* **2004**, *16*, 765.

20 A. Godula-Jopek, W. Jehle and J. Wellnitz, *Hydrogen Storage Technologies: New Materials, Transport, and Infrastructure*, **2012**, John Wiley & Sons, Inc.

21 L. Klebanoff, *Hydrogen Storage Technology: Materials and Applications*, **2012**, CRC Press, Taylor & Francis Group.

22 R. J. Press, K. S. V. Santhanam, M. J. Miri, A. V. Bailey and G. A. Takac, *Introduction to Hydrogen Technology*, **2008**, John Wiley & Sons, Inc.

23 A. Melis, *Energy Environ. Sci.*, **2012**, *5*, 5531.

CHAPTER 2

SEMICONDUCTORS FOR HYDROGEN PRODUCTION

2.1 Photoelectrochemical cells

The generation of hydrogen from the splitting of water molecules using solar light represents one of the major challenges towards the development of an efficient technology for the sustainable production of a clean and powerful fuel as H_2. Other candidates such as methanol and methane can be obtained using renewable energy sources, but given the amount of water available on our planet, as well as the high power content of hydrogen and the benefit in the emissions using carbon-free fuels, solar water splitting is the most attractive solar fuel-forming process.

Generally, to refer to any scheme for capturing and storing the energy from sunlight into fuels, the term '*artificial photosynthesis*' is used, due to the inspiration given by nature. Photosynthesis is a process used by plants and green algae to convert sunlight into chemical energy, fixing atmospheric CO_2 in carbohydrates by the splitting of water molecules. Porphyrin-antenna complex (*chlorophyll*) absorbs visible photons and transfers

electrons through a chain of transporters to the ultimate reduction of NADP to NADPH, that enters the Calvin cycle for the synthesis of sugars. The chlorophyll molecule ultimately regains the electrons lost from the splitting of a water molecule through a process catalyzed by a complex that contains four manganese ions in mixed oxidation states ($Mn^{3/4+}$) and a calcium ion (Ca^{2+}) (Figure 2.1).

The water splitting reaction proceeds through the reduction of protons to hydrogen and the oxidation of hydroxyl ions to oxygen molecules (Reactions 2.1 - 2.2). The overall reaction is endoergonic, with a standard Gibbs free energy of $\Delta_r G^0$ = 237.2 kJ, that correspond to 1.23 eV (Reaction 2.3).

$$4h^+ + 4OH^- \rightarrow 0_2 + 2H_2O \qquad E^0_{O2/OH-} = 1.23 \text{ V vs. NHE} \quad (2.1)$$

$$4e^- + 4H^+ \rightarrow 2H_2 \qquad E^0_{H2/H+} = 0 \text{ V vs. NHE} \quad (2.2)$$

$$\text{net reaction:} \quad 2H_2O \rightarrow 2H_2 + O_2 \quad (2.3)$$

The energetic barrier can be overcome with high temperature (thermolysis) or with an electric current (electrolysis) but, in principle, these reactions can be performed with semiconductor materials under irradiation without any external energetic supply. The absorption of suitable photons by the semiconductor leads to the formation of electrons and holes that, depending on their potential, are able to perform the cathodic and anodic reactions respectively, after being transferred to the solution directly from the semiconductor surface or after the extraction through an external circuit: this is the working principle of the so-called photoelectrochemical (PEC) cell. From a kinetic point of view, the overall generation of one molecule of oxygen requires the transfer of four holes through the semiconductor surface after the absorption of four photons, while only two electrons are required to evolve one hydrogen molecule. Moreover, the oxygen evolving reaction involves a higher number of steps with respect to the hydrogen evolving one. That said, the oxidation of water on a semiconductor surface is indeed the rate determining step of the overall process, and usually catalysts are employed to increase its rate.

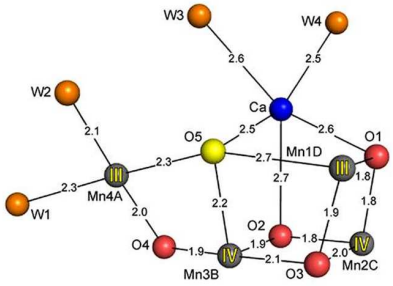

Figure 2.1. The catalytic centre for water oxidation is a Mn_4CaO_5-cluster organized as an asymmetric, distorted chair form embedded within the protein matrix of Photosystem II. The bridge oxygen atoms are named as O, while the coordinated water molecule as W (from reference [1]).

Photocatalysis on a semiconductor surface (both in the form of an electrode film or dispersed nanoparticles) involves three main steps: (i) absorption of photons with higher energies than the semiconductor band gap (1) leading to the generation of electron–hole pairs (2), (ii) charge separation followed by migration of these photogenerated carriers (3) and (iii) surface chemical reactions with water (4) (Figure 2.2). The efficiency of the conversion of photons to hydrogen is influenced by light absorption, charge separation and transport and by the reaction kinetics. The former two are strictly related to the intrinsic properties of the material, while the latter can be boosted adding catalysts (especially for the oxygen evolution reaction).

Thus different requirements have to be considered for the application of a semiconductor in a PEC device. It must to be stable in aqueous solutions under photoirradiation and gas evolution condition. The band gap should be narrow to absorb the widest portion of the solar spectrum but, on the other hand, it has to be large enough to overcome the 1.23 eV required by the water splitting reaction (considering kinetic limitations, some overpotential is necessary and band gap of 1.6 – 2 eV are the best compromise). The edge of the valence band has to be more positive than the oxidation potential of water to produce O_2 as well as the conduction band edge has to be more negative than the reduction potential of water to produce H_2 (Figure 2.3).

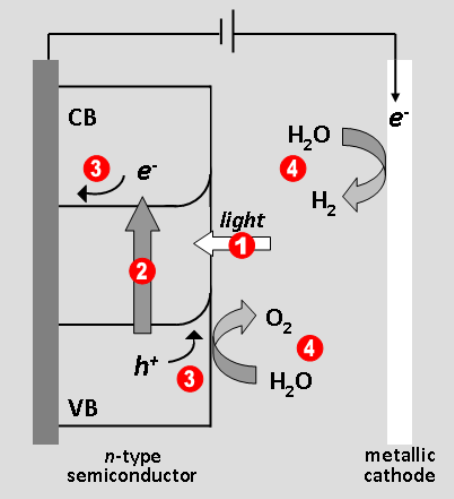

Figure 2.2. Scheme of the relevant processes involved in the solar water splitting process using a n-type semiconductor as a photoanode connected to a metallic cathode. The different steps (1 to 4) are detailed in the text.

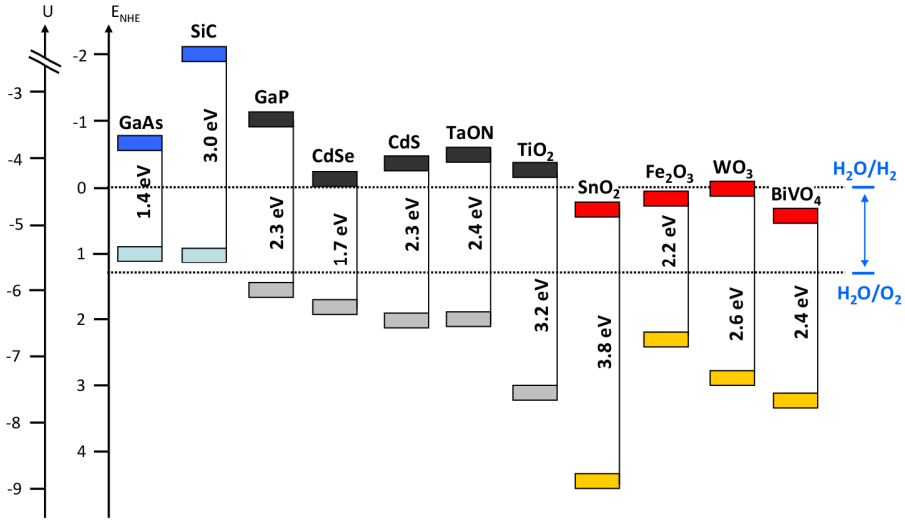

Figure 2.3. Energy levels of Conduction and Valence band edges of a selection of semiconductors relative to the reversible oxidation and reduction potentials of water (at pH = 0) are also reported as dashed lines. The energy scale is referred both to Normal Hydrogen Electrode and to the vacuum.

In 1972, Fukushima and Honda reported photoelectrolysis of water using a TiO_2 electrode illuminated with UV light.[2] TiO_2 is a n-type semiconductor that, in its anatase phase, has a band gap of 3.2 eV. Because of its n-type character, TiO_2 is able to transfer in solution holes from its Valence Band, while electrons have to travel through an external circuit to

a metal cathode, where the reduction of protons takes place. Its band gap is large enough to overcome the 1.23 eV required for water splitting and its bands are in the correct position to perform the two reactions. That said, no external energy is required for the two gas evolving reactions. By the way, the large band gap makes the TiO_2 unable to absorb visible photons, and so to appreciate gas evolution is necessary to work with UV light, that counts for a very limited part of the solar spectrum.

Visible light-absorbing materials with a sufficiently high potential to split water in one step (oxynitrides,[3,4] oxysulfides,[5] $(Ga_{1-x}Zn_x)(N_{1-x}O_x)$[6] generally suffer of a lack of stability and deactivate through photocorrosion or self-oxidation, rather than evolving O_2. For example, although cadmium sulfide (CdS) nanoparticles loaded with Pt as co-catalyst exhibit high H_2 production under visible light irradiation, S^{2-} anions are oxidized by photogenerated holes in the absence of a sacrificial electron donor, and consequently Cd^{2+} cations are released in the solution (Reaction 2.4)[7]

$$CdS + 2h^+ \rightarrow Cd^{2+} + S \qquad (2.4)$$

Until today, there is no material that meets all the requirements to carry the water splitting reaction by itself, and so it is more convenient to study and develop semiconductors for the two single reactions separately.

Oxide semiconductors are generally highly stable against photocorrosion, cheap and easy to fabricate, all important features for large-scale PEC water-splitting systems. However, because of the highly positive valence band due to the O 2p orbitals, it is intrinsically difficult to obtain oxide semiconductors with both a narrow band gap to absorb visible light and a conduction band sufficiently negative to reduce protons. Electrons and holes are generated in a n-type semiconductor by the absorption of photons with higher energies than its band gap. The photoexcited electrons are transferred to a counter electrode (e.g. Pt) through the outer circuit where they reduce water to H_2, whereas the holes are transferred to the semiconductor surface and then oxidize water to O_2 (Figure 2.4-a). An external bias is thus usually applied to the electrodes to overcome both energy level mismatching and the resistance produced at the

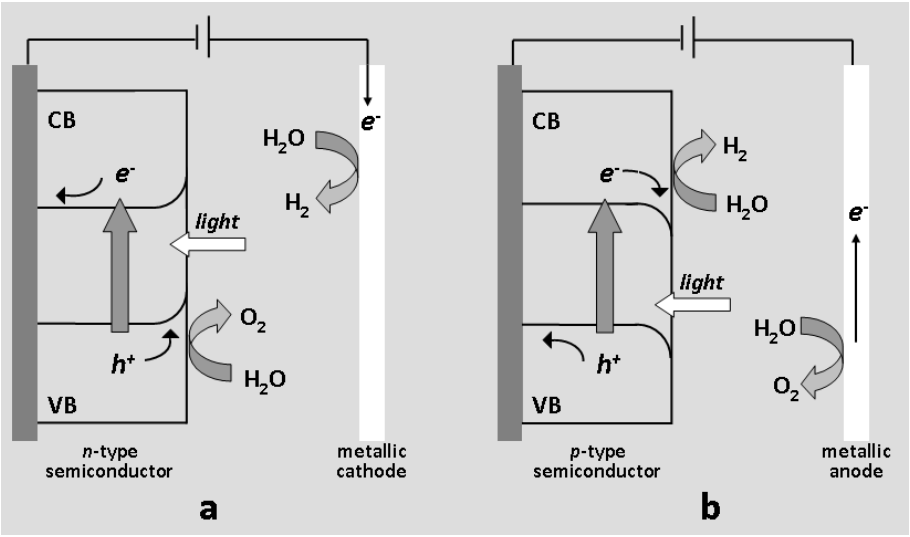

Figure 2.4. Schematic representation of the light-induced water splitting process using a (a) n-type and a (b) p-type semiconductor electrode connected to a metallic counter electrode in an electrolyte solution.

semiconductor interface: this bias can be supplied using an external photovoltaic cell (e.g. dye-sensitized solar cells, DSSC,[8] or perovskite solar cell).[9] Examples of n-type semiconductors able to oxidize water are WO_3,[10,11] $BiVO_4$,[12,13] Fe_2O_3,[14,15] n-Si,[16] Ta_3N_5[17] and n-CdTe.[18]

There have been relatively few reports on highly efficient p-type semiconductor photocathodes for the production of H_2 (Figure 2.4-b). Delafossite ($CuFeO_2$)[19,20] and $CaFe_2O_4$[21] have been reported as promising candidates for the direct PEC solar water reduction in alkaline conditions, due also to the abundance of the constituent elements, advantageous for large scale applications. Cu_2O has been extensively studied although it readily degrades due to self-reduction by photogenerated electrons.[22,23] Domen *et al.* have recently demonstrated PEC water splitting under visible light using polycrystalline $Cu(In,Ga)Se_2$ (CIGS)[24] the band gap of CIGS can be tuned over the range 1.0 - 1.7 eV by varying the Ga/In ratio.

Finally, a possibility to split water harvesting at the same time a wide range of the visible light spectrum consists in the connection of an n-type semiconductor electrode with an appropriate p-type electrode in a PEC system called tandem cell (Figure 2.5).[25] An example of a full PEC cell based on semiconductors without any external energetic supply has recently been reported.[26] One way to provide a bias is using a multijunction device,

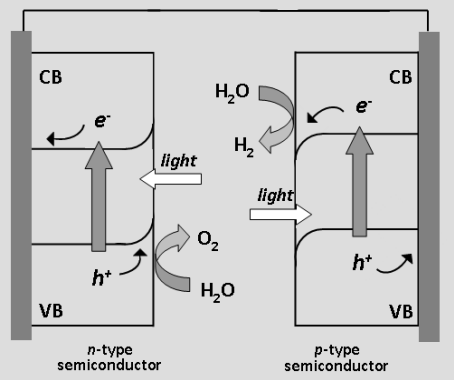

Figure 2.5. Scheme of a *tandem* cell made of a n-type and a p-type semiconductor connected through an external wire.

In which the bottom layer of the semiconductor structure provides the bias needed for the top-layer semiconductor to drive the water-splitting reaction. The monolithic p-$GaInP_2$/n/p-GaAs PEC-PV tandem cell device is a classic example of such a device. The device, consisting of a top p-$GaInP_2$ layer connected in series to an n/p GaAs bottom cell on a GaAs substrate, showed a 12.4% solar-to-hydrogen conversion efficiency (STH) with a 24 h lifetime.[27]

A strategy that will not be discussed here further employs homogeneous catalysts in solution mimicking the oxygen evolving catalyst used in the photosynthetic process.[28,31] These catalysts are usually associated to dye molecules for the harvesting of photons and sacrificial agents to help their regeneration after the water oxidation. Many semiconductors have also been employed to support these catalysts on electrodes.[32,33]

2.2 Band energy model for semiconductors

The electronic distribution of a solid can be derived from quantum mechanical assumptions by the analysis of how the periodic potential generated by the nuclei of the crystal influences the electronic motion. From a qualitative point of view, it is possible to imagine the formation of the crystal lattice starting from the gaseous atoms by studying

the behaviour of the electronic potential during the progressive reduction of the inter-atomic distance.

The electrons of a solid can be formally classified in valence and core electrons: the former occupy the external atomic orbitals, while the core ones lie in the internal and more stabilized orbitals. When two or more isolated atoms start approaching to each other until a distance comparable to the bond length, the atomic valence orbitals of each atom start to overlap, giving rise to an equal number of new orbitals: in a crystal, the interaction of N atoms cause the formation of N energetic states. The larger is N, like in a solid crystal, the smaller is the energetic difference between two consecutive levels, to such a degree to form a continuum of energetic states called band. Differently, the core electrons, being stabilized by the strong interaction with the atomic nuclei, do not interact and so they do not form any band.

Valence orbitals form the so-called valence band (VB), partially or fully filled with electrons, while the overlap among higher energetic orbitals give rise to the formation of the empty conduction band (CB): the presence of empty orbitals in the two bands allow the migration of electrons under the potential generated by an external electric field. The energy difference between the two bands is called band gap energy (E_g).

When the valence and the conduction band do overlap each other, since the difference in energy between two successive levels is small (<< kT), a very little amount of energy is necessary to promote electrons in upper levels inside the band (or across the two bands) and the solid acts as a conductive material (Figure 2.6-a), this is the case of metals. If the band gap energy is much bigger than the average thermal energy, the material acts as an insulator (Figure 2.6-b). Then, if the gap between the valence and the conduction bands is comparable with kT, valence electrons can be promoted under a suitable energetic input to the empty CB and freely move in it driven by an external electric field: these materials are called semiconductors (Figure 2.6-c). The promotion of an electron to the CB leaves an empty level in the VB, formally occupied by a hole, which can in turn accept an electron from a lower level sustaining the conduction in the material. Electrons formally move in the opposite direction of holes.

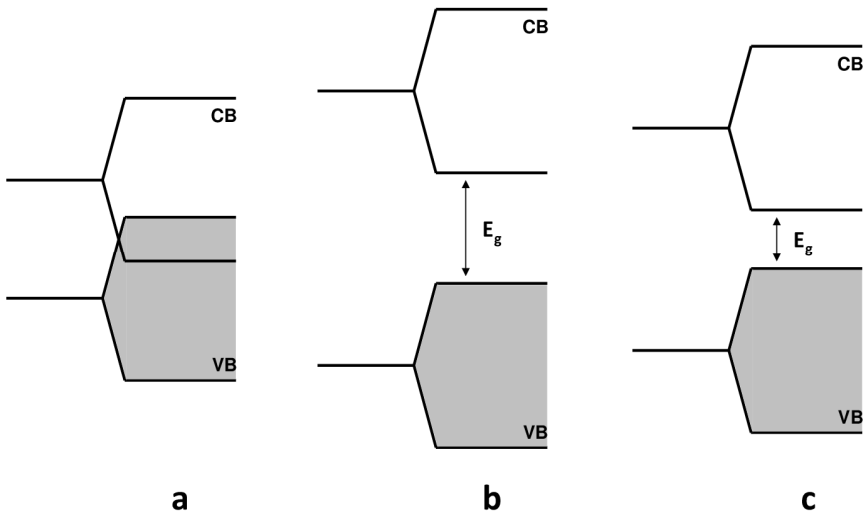

Figure 2.6. Scheme representing the energy band position for (a) a conductive solid, (b) an insulator and (c) a semiconductor.

The conductivity of a semiconductor is strongly influenced by temperature and irradiation (photons with a suitable energy can promote electrons throughout the bands).

The presence of external doping agents or imperfections in the crystal lattice strongly influence the electronic structure, forming localized states inside the band gap. The gap between these energy states and the nearest energy band is usually referred to as dopant-site bonding energy or E_B and is relatively small. If the dopant is electron rich with respect to the lattice elements, there will be the formation of intra-band states underneath the CB edge acting as donor states: these electrons can be easily promoted to the CB becoming the majority carrier species in the semiconductor. By doping pure silicon (IV group) with phosphorus (V group), extra valence electrons are added that become un-bonded from individual atoms and allow the compound to be an electrically conductive n-type semiconductor. By doping the semiconductor with electron poor elements, partially filled energy levels are added above the VB edge and they can accept electrons from the underneath VB leaving holes that become the majority charge carriers. A typical example of a p-type semiconductor is silicon doped with boron (III group). These semiconductors are called extrinsic. There are also a lot of materials that spontaneously have n or p-type character due to the presence of defects in the lattice: un-doped TiO_2 presents n-type

behaviour originated by the presence of surface defective atoms such as Ti^{3+} ions that act as electron donor species. Other examples of n-type semiconductors are WO_3, Fe_2O_3, ZnO, whereas Cu_2O and NiO present p-type character.

In a semiconductor, it is important to evaluate carefully the energy of the VB and the CB, to fully exploit the conductive properties of the material. The Fermi function (*f(E)*) corresponds to the average number of electrons per energy level at the energy E and is given by:

$$f(E) = \frac{1}{1 + e^{\frac{E - E_F}{k_B T}}} \tag{2.1}$$

where E_F is the energy of the Fermi level that is the level where the probability to find an electron per available state is 0.5, k_B is the Boltzmann constant and T the temperature (in K). The probability for an energy level to be occupied by an electron increases and decreases rapidly for, respectively, levels with energy < E_F and > E_F. It should be mentioned here that the Fermi distribution is valid only at thermodynamic equilibrium. The Fermi level position also distinguishes the different classes of materials, as E_F is located in the VB for metals (providing good electron conduction) and in the forbidden gap for semiconductors and insulators: for a n-type semiconductor the Fermi level lies between the energy level introduced by the dopant and the CB edge, and so very close to the CB, whereas in a p-type semiconductor it lies close to the VB.

Electrochemically, the E_F corresponds to the electrochemical potential of electrons in the solid and is given by:

$$E_F = \frac{(E_C + E_V)}{2} + \frac{k_B T}{2} \ln \frac{N_V}{N_C} \tag{2.2}$$

where E_C and E_V are the energy of the CB and the VB edge and N_C and N_V are the density of population of the levels in the two bands.[34] In Figure 2.3 are reported E_g, E_V and E_C

values for some semiconductors in contact with an electrolyte solution at pH=0 referred both to the Normal Hydrogen Electrode (NHE) and to the vacuum scale.

2.3 Electrochemistry of the semiconductor/liquid junction

When a semiconductor is brought in contact with an electrolyte solution, the equilibration of the Fermi level of the semiconductor with the electrochemical potential of the red-ox species in solution ($E_{red\text{-}ox}$, sometimes called the Fermi level of the electrolyte in analogy to energy levels in the semiconductor) takes place by electronic transfer through the semiconductor-liquid junction (SCLJ).[35] The direction of the electronic flux depends on the relative position of the potentials in the two phases.

In Figure 2.7 is reported the example of a n-type semiconductor in contact with an electrolyte solution characterized by a more positive electrochemical potential than the E_F of the semiconductor. In this situation, electrons are transferred from the semiconductor to the solution to achieve an equilibration of the two potentials. Being the semiconductor density of charge carriers lower than the concentration of red-ox species in solution (ca. 10^9 times lower), the material will be depleted of his majority charge carriers to a certain extent far from the surface (W_{SC}, space charge layer width). In this depletion layer inside the material, named space charge layer, there will be now an excess of minority charge carriers that, in a n-type semiconductor are holes (positive charges). On the solution side, the electrostatic interaction between negative ions and the now positive semiconductor surface generates the so-called electric Helmholtz double layer (Figure 2.8-a). The first part of this double layer, the inner Helmholtz plane (IHP), is composed by solvent molecules and partially solvated negative ions that directly stack on the material surface, while solvated ions form a second layer (the outer Helmholtz plane, OHP). Thus, the Helmholtz double layer compensates the positive charge in the depletion layer of the semiconductor, forming an electrical double layer (or Schottky junction) (Figure 2.8-b). Beyond the outer Helmholtz plane, the interaction between ions in solution and the semiconductor is less intense, due

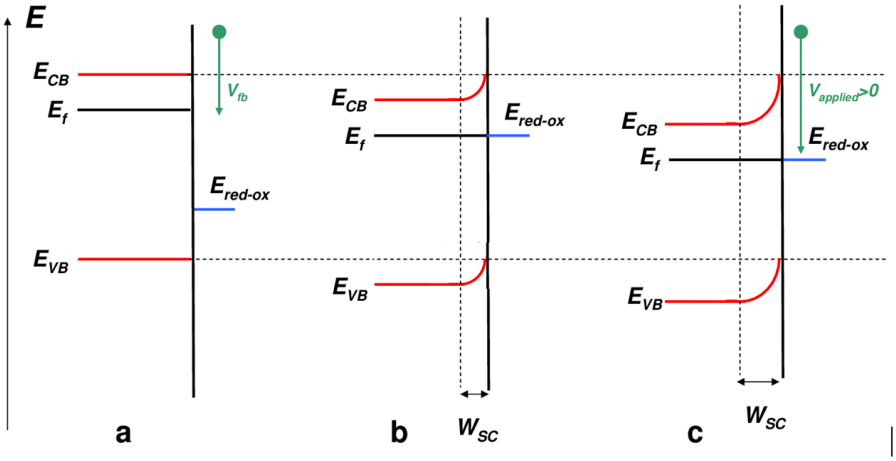

Figure 2.7. Scheme representing a n-type electrode in contact with an electrolyte solution at different external applied bias. (A) Before equilibration of the potentials: bands in the semiconductor are flat. (B) After equilibration of the Fermi level (E_F) and the electrochemical potential of the red-ox species in solution ($E_{red\text{-}ox}$) without any external potential applied: electrons are transferred from the semiconductor to the solution. (C) After the application of an external positive bias ($V_{applied} > 0$): the space charge layer width (W_{SC}) is increased as well as the band bending. In any case, bands are pinned on the semiconductor surface.

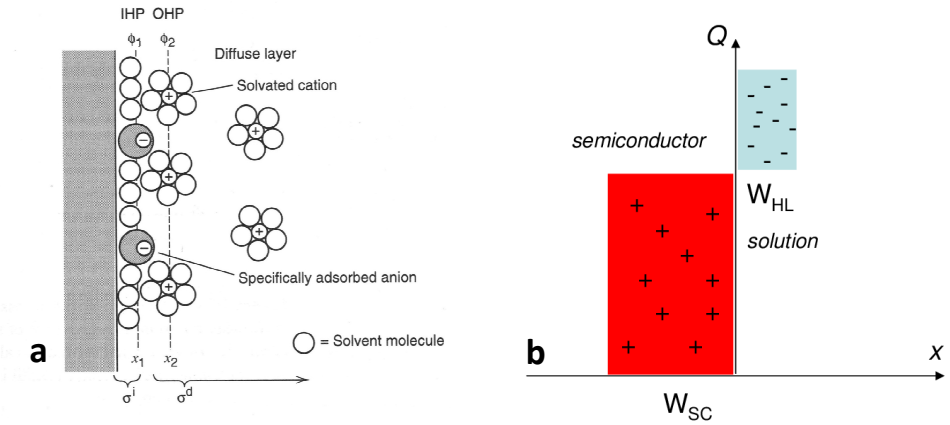

Figure 2.8. (a) Schematic representation of the Helmholtz double layer structure. (b) Schematic representation of the Schottky junction. The width of the depletion layer is usually bigger than the Helmholtz double layer due to the different concentration between charge carrier in the semiconductor and red-ox species in solution.

essentially to a shield effect of the two first layers: in this region ions are basically under diffusive control.

The depletion of electrons from the semiconductor surface induces an electric field throughout the space charge layer: it is necessary to spend work to bring an electron from the bulk of the semiconductor to its surface, due to the repulsive interaction with

the attracted negative ions in the Helmholtz layer. If we consider the system as a capacitor in which the space between the two plates (the bulk of the semiconductor and the Helmholtz layer) is represented by the space charge layer, it is possible to obtain the expression for both the electric field (Equation 2.3) and the potential (Equation 2.4) generated in the junction:

$$E(x) = \frac{eN_D}{\varepsilon} x \tag{2.3}$$

$$-\phi(x) = \frac{eN_D}{2\varepsilon} x^2 \tag{2.4}$$

where ε is the relative dielectric constant of the material, e the electronic charge and N_D the donor density. The electric field ($E(x)$) and potential ($-\varphi(x)$) increase moving from the bulk ($x \leq 0$), where there is no appreciable interaction between electrons and the Helmholtz layer; to the SCLJ ($x = W_{SC}$), where they both reach their maximum. The hyperbolic behaviour of the potential is graphically reported as an upper bending of both the VB and the CB, pinned on the surface of the semiconductor (Figure 2.7-b). So, with the illumination of a n-type semiconductor it is possible to exploit the oxidation power of holes accumulated on the surface to perform reactions in solution: after the formation of the electron-hole pair by the absorption of the energy of a suitable photons, the electron will be repelled from the semiconductor surface and extracted in an external circuit generating a current, while the hole will be attracted by the negative charge in the Helmholtz layer and transferred to the solution. In the same way, a p-type semiconductors can transfer electrons to the solution to perform reductive reactions (the behaviour of a p-type semiconductor can be derived with the same assumptions made here for the n-type one, considering that to equilibrate the red-ox potentials electrons will be transferred from the solution to the semiconductor: bands will be bent in the opposite direction).

The development of a space charge region is fundamental for the application of semiconductor electrodes in a PEC cell: without the formation of a depletion layer, the photogenerated carriers cannot be efficiently separated and extracted from the materials

and so, after their generation, recombination will take place. No current can be generated without the presence of a space charge layer.

By tuning the external potential, it is possible to modify the space charge layer characteristics. When a positive potential difference is applied ($V_{applied}$) between a n-type semiconductor and a reference electrode (fixed to the electrolyte red-ox potential), both the W_{SC} and the band bending are increased (Figure 2.7-c): qualitatively, the positive applied potential increases the donor concentration in the semiconductor surface and so the potential drop in the depletion layer. By the way, if the potential is too positive, the depletion of electrons involves not only the VB but also the CB, with the formation in this case of an inverted region (the n-type semiconductor will act as a p-type semiconductor at the surface). If a negative bias is applied, the injection of electrons slowly compensates the positive holes in the space charge layer until there will be no difference at all. The potential at which the bands become flat again is called the flat band potential (V_{fb}) that is, for instance, the E_f of the semiconductor. If the negative polarization is larger, an accumulation layer of electrons (the majority charge carriers for a n-type material) will be formed in the semiconductor itself.

2.4 Semiconductor/liquid junction under illumination

When a semiconductor electrode is irradiated using a light with energy greater than the E_g of the semiconductor, the electrode absorbs the photon energy and promote electrons from the VB to the CB: for n-type semiconductors, the photoexcited electrons hardly influence the concentration of the electrons in the conduction band (because electrons are the majority charge carriers), but the number of photoproduced holes significantly increase the total concentration of holes (the minority charge carriers), in the VB. Since under the condition of photoexcitation no thermal equilibrium is established between phonons and electrons and holes in the CB and VB, the photoexcitation process has the effect to split the Fermi level of the semiconductor into

two quasi-Fermi levels: the quasi-Fermi level of electrons ($_n\varepsilon^*_F$) and the quasi-Fermi level of holes ($_p\varepsilon^*_F$):

$$ {}_n\varepsilon^*_F = \varepsilon_{F(SC)} + kT\ln\frac{n+\Delta n^*}{n} \tag{2.5} $$

$$ {}_p\varepsilon^*_F = \varepsilon_{F(SC)} + kT\ln\frac{p+\Delta p^*}{p} \tag{2.6} $$

where $\varepsilon_{F(SC)}$ is the Fermi level energy of the semiconductor in dark conditions, n and p are the concentration of electrons and holes in the dark and Δn and Δp are the increases in the concentration of electrons and holes produced by photoexcitation ($\Delta n = \Delta p$). For a n-type semiconductor, under the conditions of photoexcitation, the quasi-Fermi level of electrons (the majority charge carriers) remains close to the original Fermi level ($n >> \Delta n^*$), but the quasi-Fermi level of holes (minority charge carriers) shifts away from the original Fermi level, because the concentration of photoexcited holes, (Δp^*) exceeds the concentration of holes in the dark ($p << \Delta p^*$) (Figure 2.9).

In the presence of a space charge layer, the photoexcited electrons and holes are separated and move in opposite directions under the electric field in the space charge layer: such a migration induces in the electrode an inverse potential, called photopotential (ΔE_{ph}), which reduces the potential across the space charge layer and retards the migration of electrons and holes in the opposite directions. As a consequence, the maximum ΔE_{ph} of a semiconductor is given by the difference between the electrode potential in the dark and the V_{fb}, at which the band bending disappears.

Photoexcited electrons or holes migrate in a space charge layer towards the electrode interface, where they participate in transfer reactions to provide a photocurrent: the photocurrent can be observed only for the reaction in which the minority charge carriers participate, namely, the transfer reaction of anodic holes at n-type electrodes and the transfer reaction of cathodic electrons at p-type electrodes. No photocurrent occurs at V_{fb} because no electric field, that is required to separate the photoexcited electron-hole pairs, is present. The photocurrent occurs at any potentials different from V_{fb}.[36]

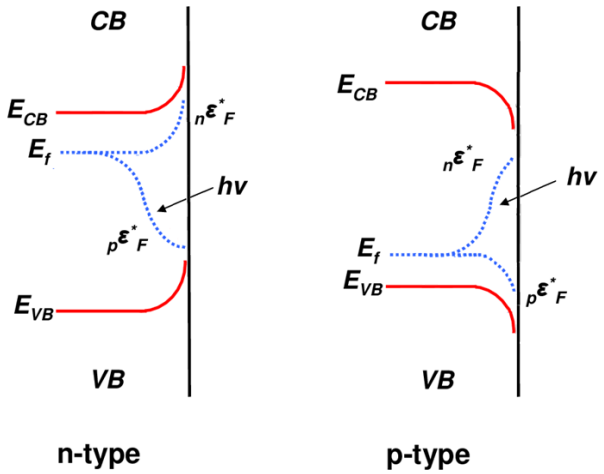

Figure 2.9. Splitting of the Fermi level of an electrode, E_F, into thequasi-Fermi levels of electrons, $_n\varepsilon^*_F$, and of holes, $_n\varepsilon^*_F$, in a photoexcited n-type and p-type semiconductors: the shift of quasi-Fermi levels from the original Fermi level is larger for minority charge carriers than for majority charge carriers.

The simplest way to describe the current/voltage (*J*-*V*) behaviour under illumination conditions is to separate the current in two separate components: one that originates from majority carriers and one from minority carriers. This is convenient because, as already told before, illumination does not significantly perturb the majority carrier behaviour both in the semiconductor or in the SCLJ: majority carriers thus exhibit a *J*-*V* characteristic that is well described by the diode equation (2.7), regardless the exposure of semiconductor to illumination:

$$i = -i_0\left(e^{-\frac{eV}{kT}} - 1\right) \tag{2.7}$$

being i_o the exchange current, which is the value of the current presents at equilibrium. For a n-type semiconductor, a value of $V > 0$ will yield a larger electric potential drop in the semiconductor, which will exponentially reduce the surface concentration of electrons and, consequently, the rate of electrons leaving the semiconductor. However, because the rate of electrons entering the semiconductor will remain unchanged, for this direction of the voltage, called reverse bias region, the net current will be independent from the voltage and electrons are injected into the semiconductor from the solution. In

forward bias regime, where $V < 0$, the surface concentration of electrons increases exponentially with the increased bias resulting in an exponential increase in the forward reaction of interfacial charge transfer (transfer of electrons to the solution), but has no effect on the reverse rate of the charge transfer: because the rate of electrons leaving the solid at high forward bias dominates the rate at which they enter it, the net current will depend exponentially on the applied voltage (it is possible to deduce the behaviour of a p-type semiconductor with the exact same deduction considering that the majority charge carriers are holes).

Calculation of the minority carrier current is simplified by the presence of the space charge layer that separates photogenerated holes and electrons: if we consider that the electric field is so strong that essentially all of the photogenerated minority carriers are separated and then collected, the minority carrier current is simply related to the rate of the formation of photoexcited electron-hole pairs, *G(x)*, [37] given by

$$G(x) = I_0 e^{-\alpha x} \tag{2.8}$$

being I_0 the intensity of photon beam, α the absorption coefficient of the photons and x the depth of photon penetration.

Thus, the net current is given by simply adding together the majority and minority components of the current. The majority carrier current (i.e. electrons) obey the diode equation while the minority carrier photocurrent (i.e. holes), i_{ph}, is directly proportional to the photon flux.

$$i = i_{ph} - i_o\left(e^{\frac{eV}{kT}} - 1\right) \tag{2.9}$$

The minus sign underscores the fact that majority carrier component flows opposite to the minority carrier current flow. The diode equation is thus offset by the i_{ph} term and the

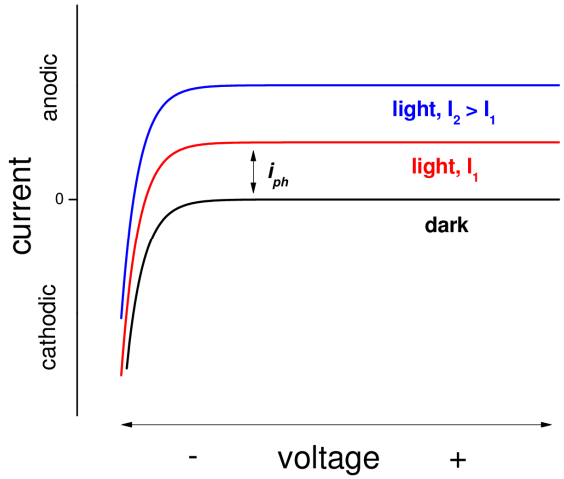

Figure 2.10. Current-voltage curve for a n-type semiconductor in the dark and under two different illumination intensities.

plateau photocurrent (where there is no more dependence of i_0 with the potential) is proportional to the photons flux (Figure 2.10).[38]

2.5 Determination of the flat band potential: the Mott-Schottky equation

The determination of V_{fb} of a semiconductor in contact with an electrolyte solution is a key point for a complete description of the properties of the junction, because it allows to define the energy of the Fermi level, to correctly place the edge of the VB and the CB and so to determine the band gap of the semiconductor. Moreover, the maximum photopotential that can be generated by a PEC cell is function of V_{fb}.

The possibility to define V_{fb} is also a proof of the development of a space charge layer within a semiconductor. Actually, the current profile alone cannot reveal that charge separation in the semiconductor is assisted by a depletion layer: the exponential section arising from the diode equation can be correctly described also by the Butler-Volmer model, based on the presence of an activation barrier for the generation of a net current.

The Mott-Schottky (MS) equation (Equation 2.10) is one of the most common method to used obtain the value of V_{fb} by plotting the inverse of the square of the differential capacitance of the semiconductor (C_{sc}^{-2}) versus V:

$$\frac{1}{C_{SC}^2} = \frac{2}{\varepsilon\varepsilon_0 N_D}\left(V - V_{fb} - \frac{kT}{e}\right) \tag{2.10}$$

being ε and ε_0 the relative dielectric constant of the material and the permittivity of vacuum respectively, N_d the donor density of the semiconductor and V the external applied potentials. A positive slope of the MS plot is indicative of a n-type semiconductor, while a negative one is obtained for a p-type (Figure 2.11). In addition to V_{fb}, it is also possible to get the concentration of the donor species N_d [cm^{-3}] of the semiconductor (electrons for a n-type and holes for a p-type) from the slope of the curve.

The MS equation in the form reported above is obtained by solving the Poisson equation that describes the density of charge carriers in the space charge layers (Equation 2.11), making an important assumption: the potential drop of the junction after the application of an external potential occurs only in the space charge region and not in the Helmholtz layer.

$$\frac{d^2E}{dx^2} = \frac{e}{\varepsilon\varepsilon_0}\left[N_D - N_A - n(x) + p(x)\right] \tag{2.11}$$

In Equation 2.11, N_D and N_A are the concentrations of donor and acceptor species of the semiconductor respectively, $n(x)$ and $p(x)$ are the electron and hole densities in the absence of any current.

To clearly understand this assumption, it can be useful to describe the different behaviour of a metal electrode in contact with a solution with respect to a semiconductor in the same situation. For a metal, the charge, and, thus, the associated potential drop, is mainly located at the surface penetrating at most a few Angstroms into the material: in other words, the high electronic conductivity of a metal cannot sustain an electric field within it.

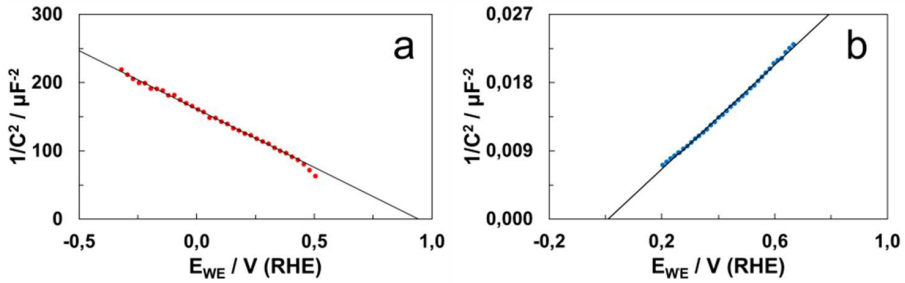

Figure 2.11. Mott-Schottky plots for (a) p-GaP and (b) n-TiO_2 in 1 M $KClO_4$ in dark conditions (from reference [39]).

Thus, when a metal electrode comes in contact with an electrolyte, almost all the potential drop at the interfaces occurs within the Helmholtz region in the electrolyte phase. Differently, the interfacial potential drop across a SCLJ is partitioned between both the semiconductor and the Helmholtz layer, leading to a simple equivalent circuit model comprising two capacitors, respectively relative to the space charge region in the semiconductor (C_{SC}) and in the SCLJ (C_H) (Figure 2.12). The total capacitance of the system is thus given by:

$$\frac{1}{C_{TOT}} = \frac{1}{C_{SC}} + \frac{1}{C_H} \qquad (2.12)$$

Because $C_H >> C_{SC}$ due to the difference in the charge carrier concentration between the semiconductor and the solution, the capacitance of the semiconductor dominates over the Helmholtz one. That said, any variation of the external potential has effect only in the space charge region capacitance, modifying the magnitude of the band bending and the width of the space charge region. The use of sufficiently high concentrated electrolyte solution allows to consider as negligible any contribution of the diffusive layer to the total capacitance.

The MS model does not consider the presence of bulk traps (i.e. defects in the crystal lattice) or surface states, that arise after surface reconstruction or bonding with different species (e.g. solvent), due to the abrupt termination of the crystal lattice at the surface

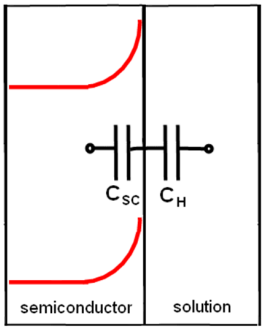

Figure 2.12. Simplified electric circuital model of the semiconductor-electrolyte interface at equilibrium.

(dangling bonds). The bulk traps act as recombination centres between photogenerated charges, decreasing the efficiency of charge separation. The surface states distributed in the band gap influence the property of the interfacial electric double layer. When the Fermi level of the electrode is pinned at a surface state (Fermi level pinning), these states are charged or discharged changing the surface state potential, as well as the potential of the compact layer. The interfacial capacity is thus determined by the capacity of the compact layer (the maximum capacity of the surface state) and remains constant in a range of potential where the Fermi level is pinned. When the Fermi level at the interface is located away from the surface state level (band edge level pinning) the surface state is either fully occupied or vacant with electrons and the charge in the surface state remains constant. As long as the Fermi level is located away from the surface state, the interfacial capacity is determined by the capacity of the depletion layer that obeys to the MS relation.

2.6 References

1 M. Suga, F. Akita, K. Hirata, G. Ueno, H. Murakami, Y. Nakajima, T. Shimizu, K. Yamashita, M. Yamamoto, H. Ago and J.-R. Shen, *Nature*, **2015**, *517*, 99.

2 A. Fujishima and K. Honda, *Nature* **1972**, *238*, 37.

3 A. Kasahara, K. Nukumizu, G. Hitoki, T. Takata, J. N. Kondo, M. Hara, H. Kobayashi and K. Domen, *J. Phys. Chem. A*, **2002**, *106*, 6750.

4 W.-J. Chun, A. Ishikawa, H. Fujisawa, T. Takata, J. N. Kondo, M. Hara, M. Kawai, Y. Matsumoto and K. Domen, *J. Phys. Chem. b*, **2003**, *107*, 1798.

5 A. Ishikawa, Y. Yamada, T. Takata, J. N. Kondo, M. Hara, H. Kobayashi and K. Domen, *Chem. Mater.*, **2003**, *15*, 4442.

6 K. Maeda, T. Takata, M. Hara, N. Saito, Y. Inoue, H. Kobayashi and K. Domen, *J. Am. Chem. Soc.,* **2005**, *127*, 8286.

7 D. Meissner, R. Memming, B. Kastening and D. Bahnemann, *Chem. Phys. Lett.*, **1986**, *127*, 419.

8 J. Brillet, J.-H. Yum, M. Cornuz, T. Hisatomi, R. Solarska, J. Augustynski, M. Grätzel and K. Sivula, *Nat. Photon.*, **2012**, *6*, 824.

9 Gurudayal, D. Sabba, M. H. Kumar, L. H. Wong, J. Barber, M. Grätzel and N. Mathews, *Nano Lett.*, **2015**, *15*, 3833.

10 C. Santato, M. Ulmann and J. Augustynski, *J. Phys. Chem B,* **2001**, *105*, 936.

11 V. Cristino, S. Caramori, R. Argazzi, L. Meda, G. L. Marra and C. A. Bignozzi, *Langmuir*, **2011**, *27*, 7276.

12 K. Sayama, A. Nomura, Z. Zou, R. Abe, Y. Abe and H. Arakawa, *Chem. Comm.*, **2003**, 2908.

13 L. Cai and H. Kisch, *J. Phys. Chem. C*, **2008**, *112*, 548.

14 A. Kay, I. Cesar and M. Grätzel, *J. Am. Chem. Soc.*, **2006**, *128*, 15714.

15 N. Dalle Carbonare, V. Cristino, S. Berardi, S. Carli, R. Argazzi, S. Caramori, L. Meda, A. Tacca and C. A. Bignozzi, *ChemPhysChem.*, **2014**, *15*, 1164.

16 S. Hu, M. R. Shaner, J. A. Beardslee, M. Lichterman, B. S. Brunschwig and N. S. Lewis, *Science*, **2014**, *344*, 1005.

17 M. Li, W. Luo, D. Cao, X. Zhao, Z. Li, T. Yu and Z. Zou, *Angewandte Chemie International Edition*, **2013**, *52*, 11016-11020.

18 M. F. Lichterman, A. I. Carim, M. T. McDowell, S. Hu, H. B. Gray, B. S. Brunschwig and N. S. Lewis, *Energy Environ. Sci.*, **2014**, *7*, 3334.

19 M. S. Prevot, Y. Li, N. Guijarro and K. Sivula, *J. Mater. Chem. A*, **2016**, 10.1039/C5TA06336A.

20 M. S. Prévot, N. Guijarro and K. Sivula, *ChemSusChem.*, **2015**, *8*, 1359.

21 S. Ida, K. Yamada, T. Matsunaga, H. Hagiwara, Y. Matsumoto and T. Ishihara, *J. Am. Chem. Soc.*, **2010**, *132*, 17343.

22 J.-N. Nian, C.-C. Hu and H. Teng, *Int. J. Hydrogen Energy*, **2008**, 33, 2897-2903.

23 A. Paracchino, V. Laporte, K. Sivula, M. Grätzel and E. Thimsen, *Nat. Mater.*, **2011**, *10*, 456.

24 D. Yokoyama, T. Minegishi, K. Maeda, M. Katayama, J. Kubota, A. Yamada, M. Konagai and K. Domen, *Electrochem. Commun.*, **2010**, *12*, 851.

25 M. S. Prévot and K. Sivula, *J. Phys. Chem. C*, **2013**, *117*, 17879.

26 A. Kargar, J. Khamwannah, C.-H. Liu, N. Park, D. Wang, S. A. Dayeh and S. Jin, *Nano Energy*, **2016**, *19*, 289.

27 O. Khaselev and J. A. Turner, *Science*, **1998**, *280*, 425.

28 Y. V. Geletii, B. Botar, P. Kögerler, D. A. Hillesheim, D. G. Musaev and C. L. Hill, *Angew. Chem. Int. Edit.* **2008**, *47*, 3896.

29 N. D. McDaniel, F. J. Coughlin, L. L. Tinker and S. Bernhard, *J. Am. Chem. Soc.*, **2008**, *130*, 210.

30 J. L. Fillol, Z. Codolà, I. Garcia-Bosch, L. Gómez, J. J. Pla and M. Costas, *Nat. Chem.*, **2011**, *3*, 807.

31 S. Piccinin, A. Sartorel, G. Aquilanti, A. Goldoni, M. Bonchio and S. Fabris, *PNAS*, **2013**, *110*, 4917.

32 L. Li, L. Duan, Y. Xu, M. Gorlov, A. Hagfeldt and L. Sun, *Chem. Comm.*, **2010**, *46*, 7307.

33 M. Yamamoto, L. Wang, F. Li, T. Fukushima, K. Tanaka, L. Sun and H. Imahori, *Chem. Sci.*, **2016**, *7*, 1430.

34 J. O. M. Brockis and A. K. N. Reddy, *Modern Electrochemistry*, **1970**, Plenum Press-New York.

35 H. Gerischer, *J. Electroanal. Chem. Interfacial Electrochem.*, **1975**, *58*, 263.

36 N. Sato, *Electrochemistry at Metal and Semiconductor Electrodes*, **1998,** Elsevier.

37 M. A. Butler, *J. Appl. Phys.*, **1977**, *48*, 1914.

38 M. X. Tan, P. M. Laibnis, S. T. Nguyen, J. M. Kesselman, C. E. Stanton and N. S. Lewis, *Progress in Inorganic Chemistry*, **1994**, N. Y. John Wiley & Sons.

39 M. Malizia, B. Seger, I. Chorkendorff and P. C. K. Vesborg, *J. Mater. Chem. A*, **2014**, *2*, 6847.

CHAPTER 3

HEMATITE FOR SOLAR WATER SPLITTING

3.1 Introduction

Since the discovery of water photoelectrolysis on illuminated TiO_2 electrodes in 1971,[1] hematite (α-Fe_2O_3) has been one of the most popular materials among the various metal oxides semiconductor for application in photoelectrochemical cells. While a photovoltaic device can capture and convert light into electricity that has to be used immediately or to be stored in batteries, PEC devices introduce a more elegant way to exploit the enormous power of solar energy, converting the incident photons in chemical energy, stored in the bond between two hydrogen atoms, mimicking what nature does every instant in the photosynthetic process. During the last decades, the rationalization of the electrical, chemical and optical properties of an increasing number of semiconductors and the easy access to various nanostructured materials led to an intense research in this field, reaching high conversion efficiencies in terms of hydrogen production.

Hematite has been soon proposed as a promising candidate to build photoanodes (where the oxidation of water to O_2 takes place) for several favourable characteristics.

i) With an average estimate of 2 to 3% in sedimentary rocks, rising to 8.5% in basalt and gabbro, iron is the fourth most abundant element in the earth's crust. Moreover, iron compounds commonly used for the preparation of hematite electrodes are generally cheap, non-toxic and biocompatible.[2]

ii) Hematite has a reported band gap of ca. 2.2 eV which allows it to absorb a substantial fraction of visible light: integration with the AM 1.5G solar spectrum produces a maximum photocurrent of 12.6 mA cm^{-2} with a potential to convert 12.9% of the sun's energy into hydrogen.[3]

iii) Hematite's valence band edge is sufficiently lower than the water oxidation potential thus allowing the transfer of photogenerated holes throughout the SCLJ to perform this reaction. Hematite's conduction band is instead too positive to reduce water, requiring an external bias that can be supplied with a photovoltaic cell (e.g. DSSC,[4] perovskite solar cell)[5] or in a tandem configuration with a small bandgap photocathode.[6,7]

iv) Hematite is perfectly stable in aqueous solution and in the basic conditions, usually employed for water oxidation due to the thermodynamical requirements. It can sustain intense illumination for prolonged time without photocorrosion also in the presence of an intense evolution of bubbles from its surface.

Although hematite fulfils the basic requirements for solar water splitting, initial attempts to use hematite electrodes for solar energy conversion have resulted in very poor performances, mainly attributed to poor charge collection efficiency.[8] An important step forward has been made using nanostructured materials (not only limited to hematite but in general for metal oxide semiconductors) that allowed to maximize light absorption and charge collection pathways. This strategy has been adopted to prepare iron oxide nano-cauliflowers,[9] oriented nanorods,[10,11] nanowires,[12] nanotubes[13] and nanonets.[14] The combination of the increased surface, active area of these nanostructured materials with a shorter pathway to transport the charges from the bulk of the semiconductor to the

surface represents the key point for a more efficient applications. Other issues related to poor electronic conductivity and slow kinetic of the oxidation of water molecules on the hematite surface have been respectively addressed with the incorporation of dopant elements in the crystal structure of the semiconductor and with the functionalization of its surface with both oxygen evolving catalysts and thin metal oxide overlayers.

3.2 Crystal structure

There are thirteen iron oxides, oxyhydroxides and hydroxides known to date. The more important ones are listed in Table 3.1. In addition to these, $Fe(OH)_2$, FeO (wüstite), β-Fe_2O_3 and ε-Fe_2O_3 and a high pressure FeOOH exist. Except for ferrihydrite and feroxyhyte, the iron oxides can be obtained in a well crystallized form. Inter-conversions between the different compounds listed in Table 3.1 are possible and often occur readily. In particular, the hydroxyl-oxides dehydrate to their anhydrous counterparts and ultimately to hematite upon heating (Scheme 3.1).[15-18]

The basic structural units of all iron oxides is an octahedron, in which each Fe atom is surrounded by six O^{2-} anions: the O^{2-} anions form layers which are either approximately hexagonally close-packed (*hcp*), as in hematite, or approximately cubic close-packed (*ccp*), as in maghemite. In both *hcp* and *ccp* structures, tetrahedral interstices also exist

Table 3.1. Major iron oxides and hydroxides.

Oxyhydroxides		**Oxides**	
formula	**mineral**	**formula**	**mineral**
α-FeOOH	Goethite	$Fe_5HO_8 \cdot 4H_2O$	Ferrihydrite
β- FeOOH	Akaganeite	α-Fe_2O_3	Hematite
γ- FeOOH	Lepidocrocite	γ- Fe_2O_3	Maghemite
δ'- FeOOH	Feroxyhyte	Fe_3O_4	Magnetite

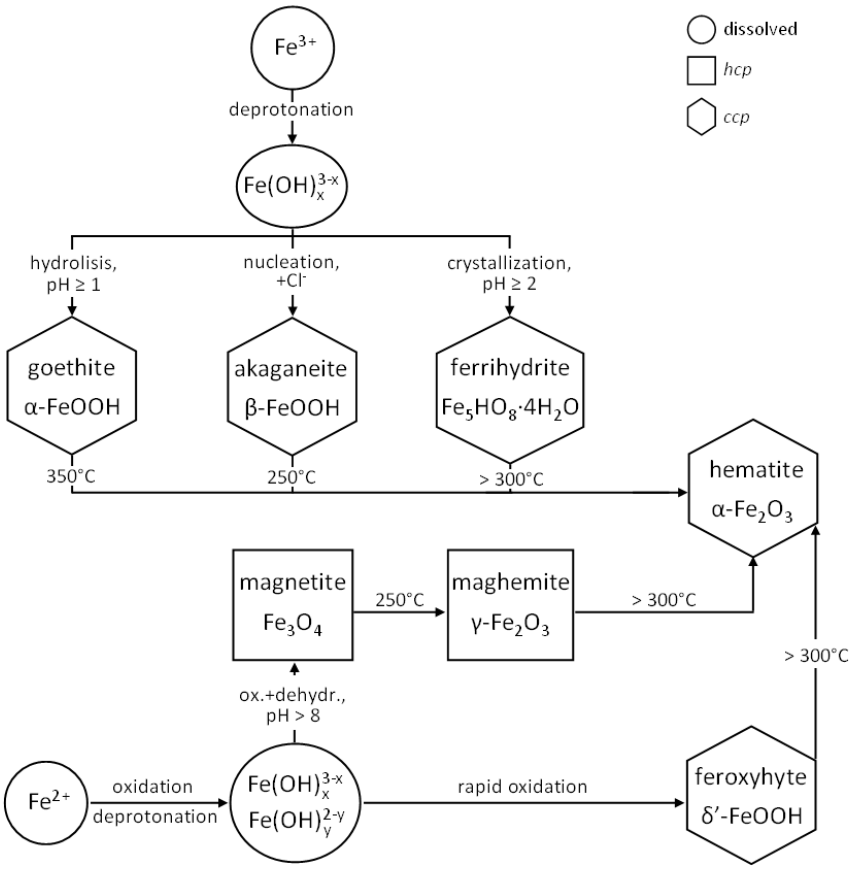

Scheme 3.1. Scheme of formation and transformation pathways of common iron oxides and oxyhydroxides with transformation conditions.

between three O^{2-} in one plane and the anion in the plane above. The *hcp*-form is termed *α*–phase, whereas the corresponding *ccp*-form is termed *γ*–phase: the *α*–phase is thermodynamically more stable than the *γ*–phase. The same considerations can be done for the oxyhydroxide species, considering both the O^{2-} and OH^{-} ions. The Fe^{3+} cations in the octahedral position may be partially replaced by other trivalent metal cations of similar size such as Al^{3+}, Mn^{3+} and Cr^{3+} without modifying the structure (isomorphous substitution).

Hematite consists of layers of FeO_6 octahedra which are connected by edge- and face-sharing (as in *corundum*, *α*-Al_2O_3) and stacked perpendicular to the *c* direction. Two thirds of the octahedral interstices are filled with Fe^{3+} ions. The face-sharing is possible through a slight distortion of the octahedra which causes a regular displacement of the Fe ions

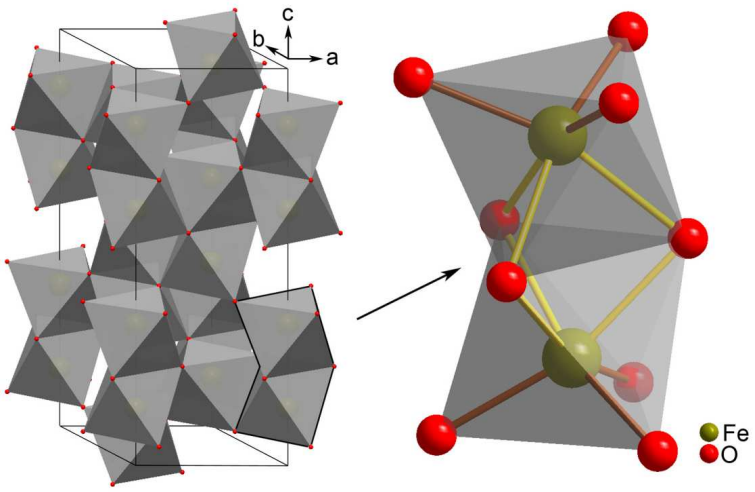

Figure 3.1 (right) Model representation of the unit cell of hematite and (right) detailed view of two FeO_6 octahedra (from reference [20]).

(Figure 3.1). The distortion and the absence of H bonds yield a compact structure which is responsible for its high density of 5.26 g cm^{-3}.[19]

3.3 Electronic structure and optical properties

The electronic structure of hematite comprises an empty conduction band with Fe 3d character and a valence band originating from Fe 3d ($2t_{2g}$) and O 2p orbitals.[21] Hematite's strong absorption from yellow to ultraviolet photons in the visible region and transmission of orange to infrared photons gives it a characteristic red colour.

Hematite has optical absorption bands in the near IR and UV regions due to crystal field and charge transfer (CT) transitions. The absorption of photons in the near-IR region give rise to weak absorption bands due to d-d transition states between electronic energy level of Fe^{3+} ions which are split by an intrinsic crystal field ($t_{2g} \rightarrow e_g$).[22] The band gap ranges from 1.9 – 2.2 eV with an indirect phonon-assisted band gap transition. Initial assignments of the band gap nature suggested that the transitions responsible for visible light absorption in hematite are indirect Fe^{3+} d–d transitions at 485-500 nm, while strong direct charge transfer transitions between O 2p and Fe 3d orbitals occur only for energies higher than 3.2 eV (400 nm), resulting in the evolution of a broad absorption band in the

range 400-600 nm.[23] This is consistent with the wavelength dependency of the photochemical response of hematite due to the formations of two types of holes (Reactions 3.1 - 3.2).[24]

$$Fe^{3+} + Fe^{3+} \xrightarrow{h\nu} Fe^{4+}(h^+) + Fe^{2+}(e^-) \quad (3.1)$$

$$O^{2-} + Fe^{3+} \xrightarrow{h\nu} O^-(h^+) + Fe^{2+}(e^-) \quad (3.2)$$

Although recently transient absorption spectroscopy measurements have revealed for the first time the unique signature of photogenerated holes,[25] it is not still possible to distinguish between Fe^{4+} (or higher valence Fe states) and O^- photoholes. Moreover, *ab initio* calculations[26] corroborated by oxygen K-edge soft X-ray[27] and photoemission spectroscopy,[28] indicate that two ligand-to-metal charge transfer (LMCT) bands occur in the region 440–800 nm, in contradiction with the previous assignment of band gap transition.

3.4 Hematite for PEC application

Iron(III) oxide was firstly investigated as photoanodic material for water photolysis by Hardee and Bard in 1976using chemically vapour deposited (CVD) films.[29] Their samples, prepared from $Fe(Acac)_3$ both on Ti and Pt substrates, showed electrochemical stability in different electrolytes solution (0.5 M KCl, 0.5 M Na_2SO_4, 1 M NaOH) under anodic polarization (from -0.6 to +1.5 V vs. the saturated calomel electrode, SCE) with a little photocurrent beginning from ca. +0.2 V vs. SCE under visible white light. Soon after, different works established the role of hematite as a promising candidate for solar application considering in particular the excellent stability of this material and the high Faradaic efficiency towards water oxidation. However, one after the other, these studies revealed several important limitations responsible for the low photocurrents recorded so far.[8,30-33]

The intrinsic difficulty in the development of an efficient photoelectrode is to bridge the photovoltaic features (light absorption, charge separation and charge transport) with catalytic ones (for water reduction and/or oxidation): most of these functions are connected and jointly depend on the optical, electrical and chemical properties of the material. It is now well established that the main limitations of hematite are due to a combination of medium light penetration depth, short diffusion length of holes (i.e. the minority charge carriers) and poor electron conductivity (i.e. the majority charge carriers) and slow water oxidation kinetics at the semiconductor surface, that requires large external overpotential to perform the reaction.

For a more systematic description of the intrinsic factors that influence the performance of a photoelectrode, it can be useful to analyse the single different processes involved in the working principle of the device. Given that, the overall efficiency can be divided in three main contributions:

i) the light harvesting efficiency, that relates to the absorption properties of the material, influencing the amount of charge carriers that can be photogenerated;
ii) the charge separation efficiency, that depends to the capability to effectively separate and transport the species to the interfaces of interest (i.e. holes to the SCLJ and electrons to the back contact);
iii) the efficiency of the water oxidation reaction, influenced by kinetic and thermodynamic aspects.

The application of nanostructuring technique to obtain rough and mesoporous films has been an important step forward to improve the efficiency of metal oxides based devices for solar water splitting, due in particular to an increase in the active surface area in contact with the electrolyte solution and to a shortening of charge transport pathways between the bulk of the material and its active interfaces. In addition, controlled doping of the material has been used to increase the ionized donor concentration to improve its conductivity. Finally, surface treatments both with oxygen evolving catalysts (OECs) and thin metal oxide overlayers have been adopted to improve the electron/hole separation and to accelerate the water oxidation kinetics at the semiconductor surface. These

strategies are nowadays essential tools commonly employed in the design process and fabrication of a hematite photoanode: they are the result of deep investigations of the intrinsic properties of the material in correlation with its PEC characteristics.

3.4.1 Charge generation and separation

The ability of a material to absorb light is determined by the Lambert-Beer law and the wavelength absorption coefficient α. The light penetration depth α^{-1} refers to the distance after which 63% of the photons are absorbed, for hematite, it is 118 nm for photon wavelengths of 550 nm. This means that to ensure > 90% absorption of the incident light, the film thickness should be at least ca. 2.3 times higher the value of α^{-1} requiring 400-500 nm thick films for complete light absorption. Most of the electron/hole pairs are thus generated deep in the semiconductor bulk, and their low mobility combined with the small diffusion length of holes (L_h is ca. 2-4 nm) results in high probability of recombination: this means that after the absorption of photons and the generation of electrons and holes, they have few possibilities to reach the interface before recombination. On the other hand, efficiency is greater with short wavelengths due to the generation of the electron/hole pair near the surface where a space charge layer exists: in this case the photognerated holes do not have to diffuse a long distance to reach the SCLJ and then be transferred to the solution to perform the reaction (Figure 3.2). Low efficiencies are due to the fact that the distribution of photons in the solar spectrum puts half of hematite's maximum possible solar photocurrent density in the wavelength range of 550-600 nm (that correspond to band gap absorption).

The average diffusion length of photogenerated carriers (i.e. L_h for holes and L_e for electrons) is an important parameter to evaluate. Photoexcitation produces charge carriers that have to reach the interfaces and, in the absence of an external electric field or a space charge region, they move by diffusion inside the material. Their range is defined by L, that depends on the carrier diffusion constant D and the carrier lifetime τ,

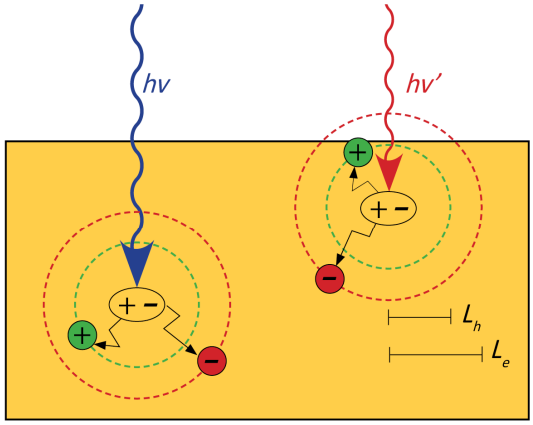

Figure 3.2. Charge collection in a flat electrode under different wavelengths illumination: with shorter wavelengths (*hv'*), holes and electrons are generated closer to the semiconductor surface and the possibilities for holes to reach the SCLJ are higher. L_h and L_e are the diffusion length of holes and electrons respectively.

that are peculiar for each material (q defines the diffusion in one-, two- or three dimensions and assumes respectively values of 2, 4 and 6):

$$\tilde{L}^2 = Dq\tau \tag{3.1}$$

For hematite, L_h is ca. 2-4 nm, an extremely low value compared to other n-type semiconductors such as TiO_2 (10^5 nm) and WO_3 (150 nm). This short diffusion length is ascribable to the very short lifetime of photogenerated carriers: metal oxides with partially filled d-shells typically exhibit low electron/hole lifetimes and the first row transition metal oxides also suffer from low electron/hole mobility (hematite is indeed classified as a Mott insulator).[23] Luminescence and ultrafast dynamic studies on both nanoparticles,[34] single crystals[35] and nanostructured thin films[36] revealed lifetimes that do not exceed hundreds of picoseconds, due to fast non-radiative processes such as recombination in mid-gap trap states.

For these reasons, standard planar films or single crystals are thus not suitable geometries for efficient hematite photoelectrodes. For a high charge separation efficiency, L_h should be comparable with the film thickness or, at least, holes should be generated very close to the hematite surface: this is not possible with flat iron oxide electrodes, that has to be thick enough to absorbs most of the incident photons to

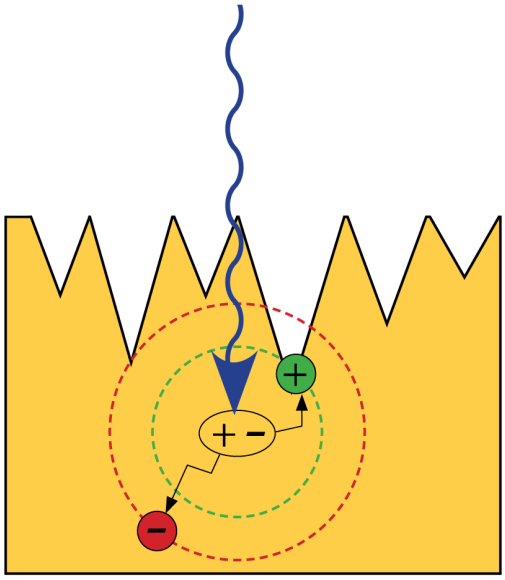

Figure 3.3. Charge collection in a nanostructured electrode. Also with long wavelength photons, the roughness of the surface decreases the distance that holes need to travel to reach the SCLJ.

guarantee a high degree of carriers generation. Surface structuring on the nano- or micro-scale gives a shortcut to overcome this problem: the presence of a very rough surface allows the generation of a high number of electron/hole pairs close to the semiconductor surface, reducing the distance that holes have to travel to reach the SCLJ (Figure 3.3).

Furthermore, there is also an enhancement in the degree of light harvesting *via* light scattering that would be otherwise lost by direct reflection in the case of a flat surface (Figure 3.4). This allows to prepare thinner electrodes with respect to the thickness required for a complete absorption of the photon flux, with enormous advantages for both the charge generation and separation efficiency.

Some disadvantages originate from the intrinsic properties of nanostructured semiconductors. Surface and interfacial recombination rates are enhanced both in the bulk and at defects present on the surface: these processes diminish the steady state concentration of usable charge carriers and reduce the rates of water electrolysis and carrier extraction. One of the reasons is the larger specific interfacial area, as well as the not perfect connection of the single nanoparticles fused together, that can generate significant resistance losses due to an imperfect charge transport. Finally, charge

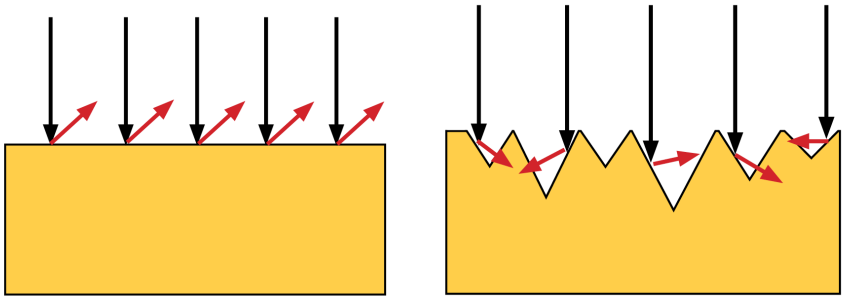

Figure 3.4. Different behaviour of incident (black arrows) and scattered light (red arrows) in flat and nanostructured electrodes.

separation can suffer from a non-effective space charge layer assistance due to the nanoscale environment: in the absence of internal electrical forces, the electron/hole injection in the electrolyte is mainly governed by the kinetics of the interfacial charge transfer alone, limiting its efficiency and increasing at the same time the amount of recombination. For these reasons, usually surface treatments are employed to passivate the surface from defects in the morphology that act as recombination centres and an external bias assists the charge separation process.

3.4.2. Electronic conductivity

As a Mott insulator, α-Fe_2O_3 suffers not only from slow hole transport but also from very slow electron transport, an inadequate feature for PEC applications. Conductivity of hematite has been explained with electrons hopping from Fe^{2+} to Fe^{3+} by thermal excitation or with the presence of Fe^{4+} ions that may introduce electrons into the conduction band.[37] Impurity doping of ferric oxide by higher or lower valent ions produces a mixed valence state that alters the electrical resistivity of the material, making it more suitable for PEC studies. For example, when Ti^{4+} is introduced into the α-Fe_2O_3 lattice, it produces Fe^{2+} sites (to maintain the average charge per cation at +3), that act as donor centres and can provide an electron to the surrounding Fe^{3+} ions.[38] Indeed, it is possible to increase the conductivity and to obtain both p-type or n-type α-Fe_2O_3 by substitutionally doping with atoms such as Mg^{2+}, Cu^{2+} (p-type) or with Sn^{4+}, Zr^{4+} and Nb^{5+}

(n-type). For example, in hematite film prepared by colloidal dispersion on FTO (Fluorine doped-Tin Oxide, a transparent and conductive glass substrate) and composed by nanoparticles of 5-10 nm in diameter, no water splitting photocurrent was observed upon sintering at 400 or 700 °C, while 20 minutes at 800 °C were sufficient to diffuse and activate dopants (Sn^{4+} from the substrate) affording relatively high photocurrents.[39] Qin *et al.* used the Mott–Schottky technique to quantify carrier concentrations in Sn-doped α-Fe_2O_3 nanowire arrays: increasing the temperature led to an increased electronic concentration (from $7 \cdot 10^{19}$ to $2.45 \cdot 10^{20}$ cm^{-3}) and higher photocurrents (up to 0.7 mA cm^{-2} at 1.23 V vs. RHE in 1.0 M NaOH and AM 1.5G).[40] The same effect has been observed upon doping hematite with Cd^{2+} ions: incorporation percentages of 0.4–1.45 % enhanced the photocurrent by a factor of 4 at 1.23 V vs. RHE.[41] It also seems that the Cd(II) ions shift the absorption band to mostly visible light region extending the wavelength windows absorbed to 665 nm. Although lattice distortions resulting from the introduction of ionic dopants either larger or smaller than Fe(III) ions might be expected to allow stronger low-energy transitions due to a lowering of the ground-state symmetry, and to boost light absorption, different reports showed that, if this effect is present at all, it's very small.[42,43]

In principle, there are several ways by which dopants can improve the performance of hematite films rather than enhancing the electronic conductivity, and the specific cause of any improvement has not been unambiguously determined. For example, the better performance of Ti doped hematite film has been explained with improved crystallinity,[44] with a catalytic effect on the water oxidation kinetics at the semiconductor surface[45] and with a passivation effect on surface state recombination centres.[46] It seems thus more likely that the overall effect should be ascribed to a combination of different effects, both on morphology and bulk properties, as suggested by Zandi *et al.*[47]

3.4.3. Synthesis of nanostructured hematite films

In 1984 Bockris and Itoh introduced the spray pyrolysis technique for the synthesis of nanostructured α-Fe_2O_3 electrodes.[48] They used an ethanolic solution of $FeCl_3$ sprayed onto conductive glass substrates heated at 350 °C in air, using nitrogen as gas carrier, obtaining compact and uniform film with a mirror-like aspect, characterized by high sheet resistance and photocurrent around 1 mA cm^{-2} in NaOH+Na_2SO_4 electrolyte solution. The technique was further developed by Augustinsky[49] and finally gained popularity in 2005 when the Grätzel group modified the procedure introducing an ultrasonic spray nozzle to create very fine droplets of the precursor solution (ultrasonic spray pyrolysis, USP) reaching a remarkable photocurrent of 1.3 mA cm^{-2} at 1.23 V vs. RHE in NaOH 1 M under AM 1.5G illumination (100 mW cm^{-2}).[50] In 2006, Kay *et al.* used the chemical vapour deposition technique at ambient pressure (APCVD) obtaining mesoporous films of hematite doped with silicon from the thermal decomposition of $Fe(CO)_5$ mixed with a TEOS solution, a silicon precursor.[9] They obtained cauliflower-type morphology (Figure 3.5) with a maximum feature size of 5-10 nm perpendicularly oriented on the FTO, showing current densities of 1.8 mA cm^{-2} at 1.23 V vs. RHE under AM 1.5G illumination in NaOH 1 M, further improved to 3.0 mA cm^{-2} after the optimization of a 800 nm thick film.[51] The combination of the small particles size, aligned to the basal crystal plane normal to the FTO, and the incorporation of Si^{4+} ions in the hematite lattice, led to very high efficiencies both in charge generation and separation processes.

Solution-based colloidal methods for preparing oxide semiconductor electrodes allow for the use of inexpensive processing techniques (e.g. spin coating, doctor blading) to coat a precursor solution or a dispersion of nanoparticles plus a porogenic agent onto a conductive substrate. Drying and then heating these films led to a porous structure of interconnected oxide particles. This method was first reported in 1994 with a sol created from the hydrolysis of $FeCl_3$ combined with a polyethylene glycol, and then doctor bladed on FTO.[52] Other examples include polymeric precursors prepared by the condensation of citrate salts,[53] Fe_2O_3 nanopowder combined with hydroxylpropyl cellulose[39] and of an iron nitrate and oleic acid solution dip casted on FTO have been reported.[54] However,

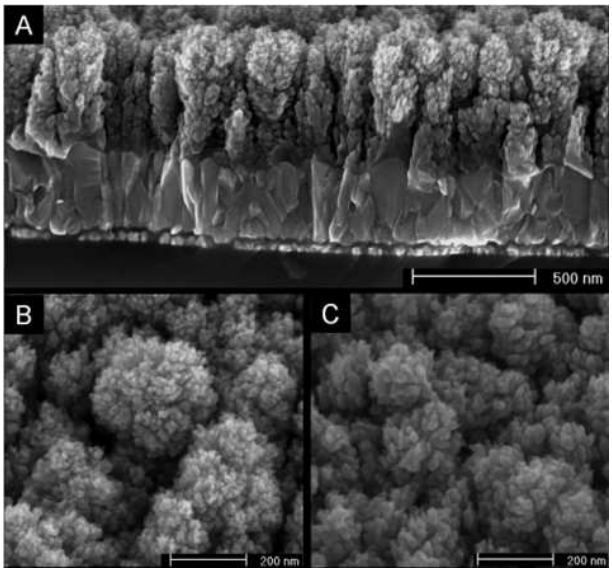

Figure 3.5. HR-SEM images of (A-B) silicon doped α-Fe_2O_3 and (C) pure α-Fe_2O_3 grown by APCVD (from reference [9]).

usually these systems give lower photocurrents due to a high degree of charge carrier recombination for the presence of grain boundaries between the particles.

In the early 2000s, Vayssieres *et al.* proposed a novel methodology to obtain large arrays of metal oxide in monodispersed perpendicularly oriented single-crystalline nanorods, grown directly onto a solid substrate with a very simple solution-based procedure, finding a cheap and realistic way to obtain aligned and ordered nanomaterials with a controlled and well defined structure.[10,55] The basic theoretical concept, called 'purpose-built materials', concerns in the monitoring of the thermodynamics and kinetic of nucleation and growth of the system by controlling experimentally the interfacial tension (surface free energy), thus allowing to separate the nucleation and the growth stage of the material directly on a solid substrate. To obtain the most suitable morphology for PEC application, the reduction of this interfacial energy, achieved by the control of the pH and of the ionic strength of the precursor solution, led to a lowering of the nucleation energy barrier with a consequently large stage of nucleation of very small particles at a very short stage of growth. They were able to obtain, in this way, well-aligned crystalline nanorods grown in a fairly perpendicular fashion onto the substrate and arranged in very large uniform arrays (Figure 3.6), after the thermal annealing (at T > 400 °C) of the metastable

iron oxide phase (β-FeOOH, pure akaganeite), that is firstly formed in a $FeCl_3$ solution at pH 1.5 heated at 100 °C. They did not limit the application of this technique only to hematite, demonstrating its efficacy also with other metal oxides semiconductors (e.g. TiO_2, ZnO).

After their first report of a hematite photoanode with reasonably PEC performances obtained with this new and convenient approach in 2000,[56] this solution based methodology has been widely employed to investigate various aspects affecting the activity of hematite photoelectrodes, such as the doping effect of different cations (e.g. Sn^{4+}, Ti^{4+})[12,57], the surface treatment with oxygen evolving catalysts,[58] the effect of annealing temperature on the film morphology[59] and on the oxygen content in the crystal lattice[60] and the particle encapsulation in oxides scaffold-matrix.[61] Indeed, the hematite top performer has been obtained in 2013 by Domen *et al.* using a hydrothermal grown hematite film doped with Pt and successively modified with a cobalt based catalyst, reaching photocurrents of 4.32 mA cm^{-2} at 1.23 V vs. RHE in 1 M NaOH under AM 1.5G illumination (Figure 3.7).[11]

Although it is not easy to make a comparison between different synthetic methodologies related to the PEC performances of hematite photoelectrodes, one clear difference is that vapour assisted techniques, such as spray pyrolysis and APCV,D work at relatively low temperatures (400-500 °C), while colloidal or solution-based procedures need much higher temperature (700-800 °C) to produce photoactive materials. This is due to different factors, such as the presence of doping impurities and quality of the crystal lattice.

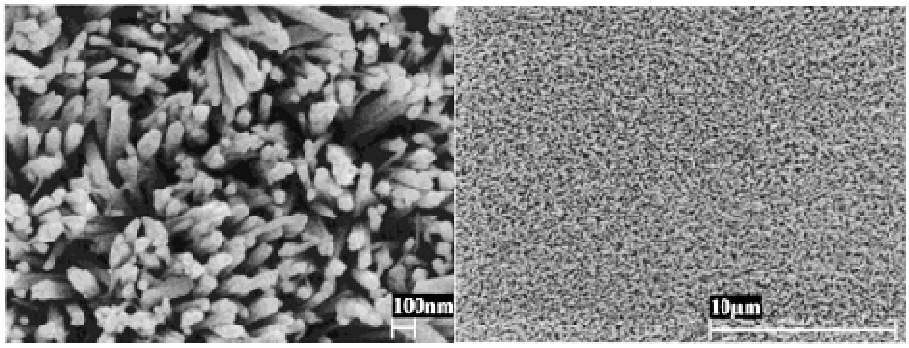

Figure 3.6. FEG-SEM images of oriented hematite nanorods grown on tin oxide glass substrate (from reference [10]).

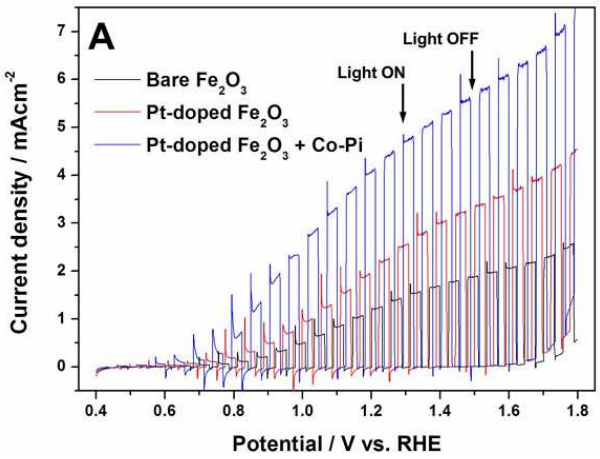

Figure 3.7. Photocurrent potential curve of different hematite photoanodes obtained by solution based methodology on FTO substrate recorded in NaOH 1 M under AM 1.5G illumination (100 mW cm^{-2}) (from reference [11]).

Hematite electrodes prepared by this latter route usually suffer from recombination in both the bulk and at the surface defects. Furthermore, the high temperature treatment required is deleterious in terms of increased resistance of the glass substrate and of increased feature size of the original nanoparticles, reducing the surface area of the film, and consequently the efficiency in charge collection of the minority carriers. Given that, vapour assisted techniques usually yield better pristine hematite photoanodes in comparison with solution processed ones.

Another facile method to obtain nanostructured hematite consists in the thermal oxidation of iron foils. Thermal oxidation in an oxygen rich atmosphere gave rise to nanorods which showed a photocurrent of 1.6 mA cm^{-2} at 1.6 V vs. RHE: in an oxygen-clean environment, hematite nanocorals were obtained with a best photocurrent density of 2.6 mA cm^{-2}.[62]. Nanowires with a diameter of 20-40 nm and length up to 5 µm have been reported.[63] Although the accessible morphologies are suitable for efficient holes transfer to the solution, photoresponse is usually very poor at low applied bias due to high recombination kinetics at the substrate interfaces, where sub-oxides act as recombination centres. Charge recombination also limits the performance of hematite nanotubes obtainable by potentiostatic anodization of iron foils in NH_4F solution and ethylene glycol (Figure 3.8).[64] Thermal post-formation annealing, needed to obtain a crystalline material, usually alter the ordered array of nanostructures.[13]

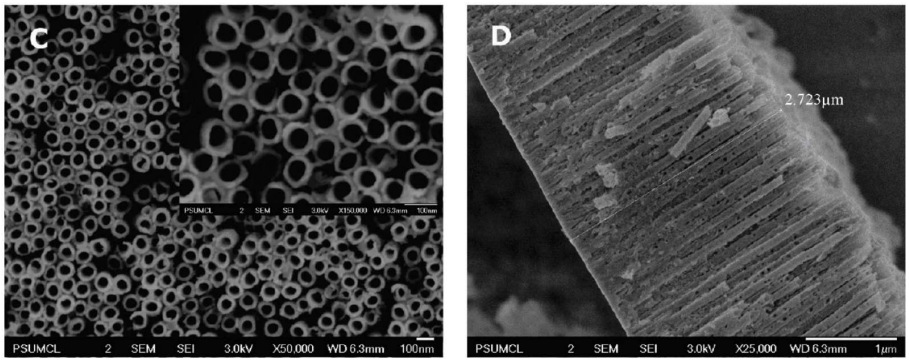

Figure 3.8. FESEM top view and cross-sectional images of iron oxide nanotube arrays prepared by anodization of an iron foil at a potential of 50 V in ethylene glycol + 0.5 wt % NH_4F + 3.0% DI water, for a duration of 180 s at 45 °C (from reference [64]).

3.4.4. Water oxidation efficiency

Although nanostructuring and doping can overcome the short holes diffusion length and the poor electronic conductivity in hematite, holes that reach the surface still must be collected and transferred to the solution efficiently to perform the water oxidation reaction. It is well established that slow water oxidation kinetics limit the performance of α-Fe_2O_3, especially at low applied potential, where the rate of oxygen evolution is governed by the rate of holes transfer to H_2O molecules or OH^- anions. At sufficiently high driving forces, the rate of oxygen evolution, as indicated by the plateau value of photocurrent, is instead largely governed by the rate of delivery of holes to the SLCJ.

Ideally, with a n-type semiconductor it would be possible to observed photocurrent at any potential more positive (i.e. more anodic) than the V_{fb}, because the space charge region developed at these potentials (at which the bands start to bend) help the charge separation and the transfer of holes to the solution. Common values of V_{fb} for hematite are reported to be 0.3-0.4 V vs. RHE but, also with the top performer electrodes, no photocurrent is detected until ca. 1 V vs. RHE: there are thus at least 500 mV of overpotential needed to trigger the water oxidation reaction at hematite surface (Figure 3.9). This overpotential has been most often ascribed to kinetic limitations of the

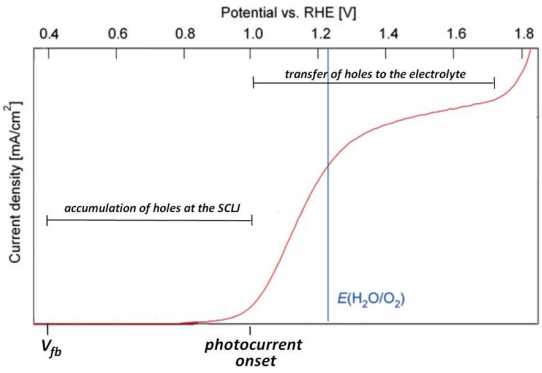

Figure 3.9. Example of a typical *JV* curve for a hematite photoelectrode under solar simulated illumination.

water oxidation reaction because it must involve four photogenerated holes to evolve one molecule of O_2.

When fast one-electron redox couples, such as $[Fe(CN)]^{3-/4-}$ is employed with thin films of hematite deposited by ALD (Atomic Layer Deposition),[65] the collection can be quantitative without the need of any overpotential with respect to the flat band potential: this means that holes are indeed available at the SCLJ to perform water oxidation already at a potential close to V_{fb}, but they accumulate because the reaction rate is extremely low. This accumulation continues until the creation of a field that opposes to the space charge field and stops the further separation of charges: this situation is observable as transient photocurrent spikes when the *J-V* curve is recorded with a pulsed illumination source between the V_{fb} and the beginning of the photocurrent. The same results have been obtained using H_2O_2 as hole scavenger (Figure 3.10).[66]

To overcome these kinetic limitations, OECs based on metal complexes with very low overpotential for water oxidation reaction have been employed.[67] Treatment of CVD-prepared nanostructured α-Fe_2O_3 photoanodes, with a monolayer of adsorbed Co^{2+} from $Co(NO_3)_2$, resulted in a cathodic shift of the photocurrent onset of about 80 mV,[9] This results are consistent with the high activity of cobalt based oxides towards water oxidation, although the parasitic light absorption by these catalysts allows only a thin layer of it to be deposited. So far, the best example of this approach has been reported so far by Tilley *et al.*

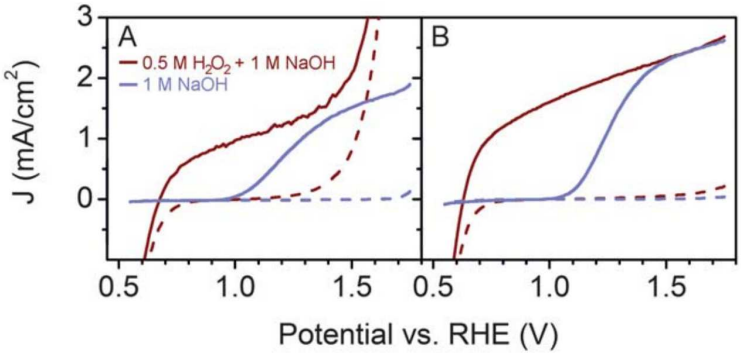

Figure 3.10. Current density vs. applied potential plots in dark (dotted curves) and under simulated solar illumination (solid curves) for USP (A) and APCVD (B) hematite electrodes (from reference [66]).

who attached iridium oxide nanoparticles (IrO_2) of about 2 nm in diameter to hematite photoanodes, recording a shift in the water oxidation photocurrent onset of 160 mV,[51] exploiting the excellent Faradaic efficiency of this type of metal catalyst.[68] Other catalysts based on nickel(II) hydroxide, $NiFeO_x$ layers and amorphous iron oxides have been reported.[69-71,58] Few examples of molecular homogeneous catalysts based on iridium,[72] cobalt oxo-cubane[73] and ruthenium[74] complexes coupled whit hematite electrodes have been reported to date, because they can rapidly be degraded by high oxidative intermediates formed in solution during the water oxidation pattern reactions (e.g. OH radical)[75] or, depending on the conditions,[76] can lead anyway to heterogeneous materials with electrocatalytic activity.

It is however surprising that, after the application of high performance electrocatalysts, the observed onset potential still exceeds by several hundreds millivolts the minimum onset potential theoretically achievable. This suggests that kinetic factors alone cannot explain the low efficiency of water oxidation activity of hematite. The presence of surface states that act as recombination centres for the photogenerated holes has been soon proposed as an additional mechanism that cause losses in water oxidation efficiency for hematite electrodes. Both the mechanistic details of the processes involving these surface traps and their chemical nature are still unclear: it is not well understood if they are intrinsic surface states, due to crystalline defects at the surface of the semiconductor material, alos induced by illumination, or if they arise from an energy mismatching between the acceptor d orbitals of hematite and donor p orbitals of the O^2-OH^- redox

couple. These states, present at the SCLJ, with energies in the band gap of the semiconductor, can trap energetic valence band holes (that either recombine with conduction band electrons or participate in water oxidation reactions), causing a loss in the amount of holes available for the reaction. They are also responsible for the so-called 'Fermi level pinning' of the bands of the semiconductor: the external applied bias does not induce the bending of the bands of the semiconductor, but rather causes the filling and the emptying of these surface states, preventing the formation of a space charge layer inside the semiconductor, able to assist the electron/hole separation also at low applied bias. This would explain the large anodic potential required to appreciate photocurrent in hematite electrodes.

Recently, evidence of the existence of surface states in the semiconductor/liquid interface where holes accumulate and contribute both to Fermi level pinning and to the late onset of water oxidation has been revealed by Hamann and Bisquert using electrochemical impedance spectroscopy (EIS).[77] They found a strong correlation between an additional capacitive component under illumination referred to the development of a surface state capacitance (C_{ss}), and a valley in the charge transfer resistance from these states ($R_{ct,ss}$) with the onset of photocurrent (Figure 3.11). These results indicate that hole transfer takes place predominantly from surface states rather than directly from the valence band. A strategy recently reported to alleviate the recombination at these surface states consists in the use of very thin metal oxide overlayers (few nanometers) that are able to uniformly cover the hematite surface maintaining its rough morphology: reduction of the onset potential ascribable to limitation in electron/hole recombination in these trap states have been observed with Al_2O_3, Ga_2O_3 and In_2O_5.[78,79] Interestingly, Barroso *et al.*[80] and Klahr *et al.*[81] reported a similar effect of passivation of surface states at the SCLJ after the photodeposition of a cobalt oxyhydroxide from a phosphate buffer (Co-Pi), thus revealing that although cobalt oxides commonly act as a an electrocatalyst in the dark (by increasing the rate of holes transfer to the solution), when it is coupled with a semiconductor under illumination it can carry out also a passivation effect. Sivula analyzed this dual-behaviour and pointed

out which are the requirements to be a 'real catalyst' for the water oxidation reaction at a photoanode surface.[82]

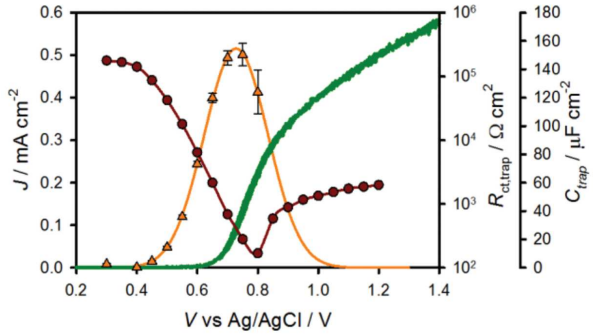

Figure 3.11. Plot of C_{ss} (orange triangles) and $R_{ct,ss}$ (red circles) with the *JV* curve of 60 nm ALD deposited hematite electrode at pH 6.9 under 1 sun of illumination (from reference [77]).

Although the exact mechanism and the nature of the intermediates involved in the oxygen evolution reaction (OER) on hematite surface are not still fully clarified, there are in literature several experimental indications, supported by theoretical calculations on the crystal surface, about the possible pathways for oxygen formation.[83,84]

First of all, the water oxidation reaction consists of four oxidation steps, each of which results in the release of a proton into the electrolyte, that will eventually meet an electron been transferred at the cathode. The first oxidation step involves the absorption of H_2O molecules onto the surface, more likely as OH^- anions given the basic working environment. Both the formation of metal superoxide (M−O−O−M) and metal-oxy-hydroxide (M-OOH) species has been observed on metal oxide nanoparticles,[85] and the existence of highly valent iron species, such as Fe(IV), Fe(V) and Fe(VI), has been predicted using modulated transmittance and impedance spectroscopy.[86,87] These observations, suggested a concerted mechanism on the substrate surface involving two vicinal Fe atoms (rather then a single Fe site) at which the rate determining step involves the oxygen−oxygen bond formation. In 2015, Le Formal *et al.* reported the first rate law analysis of photoinduced water oxidation on nanostructured hematite using photoinduced absorption spectroscopy (PIA) under external applied bias and different light intensities, simulating photoelectrochemical operating conditions.[88] Under

conditions where water splitting occurs, the photoholes were found to have a lifetime of ca. 3 s, indicating that the oxidation of water on α-Fe_2O_3 requires extremely long-lived holes, as demonstrated by the Durrant group using transient absorption spectroscopy (TAS).[89] To be competitive with charge recombination occurring on similar time scales,[90] high density of holes are needed at the SCLJ to drive the hole transfer to the solution. They interestingly found a third-order kinetic law under high hole accumulation conditions (where hole mobility is unlike to be a critical consideration), which results in a reaction mechanism where the rate-determining step requires the three-holes oxidation of a reaction intermediate. On the basis of their results, they proposed two plausible mechanisms involving two adjacent iron atoms on the hematite surface (Figure 3.12): the initial oxidation of the two neighbouring irons is relatively facile, while the third oxidation (i.e. the rate determining step) may lead to the formation of an Fe(V)-oxo specie or oxidation of the bridging oxygen.

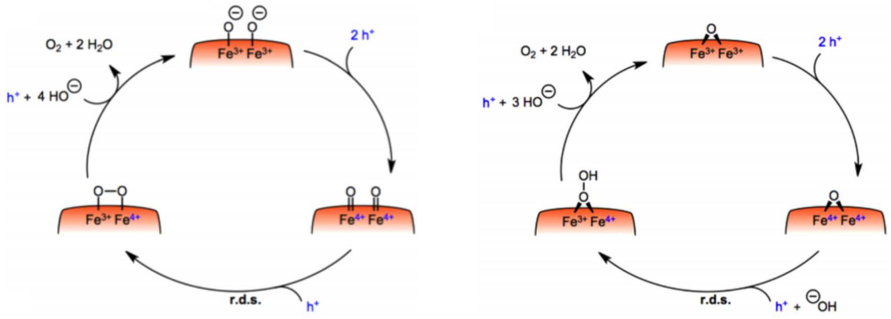

Figure 3.12. Mechanism of oxygen formation on nanostructured hematite surface proposed on the basis of photoinduced absorption spectroscopy (PIA) investigation (from reference [88]).

3.5 References

1 A. Fujishima and K. Honda, *Nature*, **1972**, *238*, 37.

2 M. Yellishetty, P. G. Ranjith and A. Tharumarajah, *Resour. Conserv. Recy.*, **2010**, *54*, 1084.

3 A. B. Murphy, P. R. F. Barnes, L. K. Randeniya, I. C. Plumb, I. E. Grey, M. D. Horne and J. A. Glasscock, *Int. J. Hydrogen Energ.*, **2006**, *31*, 1999.

4 J. Brillet, J.-H. Yum, M. Cornuz, T. Hisatomi, R. Solarska, J. Augustynski, M. Grätzel and K. Sivula, *Nat. Photon.*, **2012**, *6*, 824.

5 Gurudayal, D. Sabba, M. H. Kumar, L. H. Wong, J. Barber, M. Grätzel and N. Mathews, *Nano Lett.*, **2015**, *15*, 3833.

6 M. S. Prévot and K. Sivula, *J. Phys. Chem. C*, **2013**, *117*, 17879.

7 H. Wang, T. Deutsch and J. A. Turner, *J. Electrochem. Soc.*, **2008**, *155*, F91.

8 J. H. Kennedy and K. W. Frese, *J. Electrochem. Soc.*, **1978**, *125*, 709.

9 A. Kay, I. Cesar and M. Grätzel, *J. Am. Chem. Soc.*, **2006**, *128*, 15714.

10 L. Vayssieres, A. Hagfeldt and S. E. Lindquist, *Chem. Mater.*, **2001**, *13*, 233.

11 J. Y. Kim, G. Magesh, D. H. Youn, J.-W. Jang, J. Kubota, K. Domen and J. S. Lee, *Sci. Rep.*, **2013**, *3*, 2681.

12 Y. Ling, G. Wang, D. A. Wheeler, J. Z. Zhang and Y. Li, *Nano Lett.*, **2011**, *11*, 2119.

13 S. K. Mohapatra, S. E. John, S. Banerjee and M. Misra, *Chem. Mater.*, **2009**, *21*, 3048.

14 Y. Lin, S. Zhou, S. W. Sheehan and D. Wang, *J. Am. Chem. Soc.*, **2011**, *133*, 2398.

15 S. Gialanella, F. Girardi, G. Ischia, I. Lonardelli, M. Mattarelli and M. Montagna, *J. Therm. Anal. Calorim.,* **2010**, *102*, 867.

16 K. Stahl, K. Nielsen, J. Jiang, B. Lebech, J. C. Hanson, P. Norby and J. van Lanschot, *Corros. Sci.,* **2003**, *45*, 2563.

17 Z. Jianmin, F. E. Huggins, F. Zhen and G. P. Huffman, *Clay. Clay Minerals*, **1994**, *42*, 737.

18 G. Schimanke and M. Martin, *Solid State Ionics*, **2000**, *136–137*, 1235.

19 U. Schwertmann and R. M. Cornell, *Iron Oxides in the Laboratory: Preparation and Characterization*, **1991**, VCH, Weiheim.

20 K. Sivula, F. Le Formal and M. Grätzel, *ChemSusChem*., **2011**, *4*, 432.

21 U. Schwertmann and R. M. Cornell, *The Iron oxides. Structure, Properties, Reactions and Uses*, VCH, **1996**, Weiheim.

22 L. A. Marusak, R. Messier and W. B. White, *J. Phys. Chem. Solids*, **1980**, *41*, 981.

23 G. K. Rozenberg, L. S. Dubrovinsky, M. P. Pasternak, O. Naaman, T. Le Bihan and R. Ahuja, *Phys. Rev. B: Condens. Matter Mater. Phys.*, **2002**, *65*, 641121.

24 N. C. Debnath and A. B. Anderson, *J. Electrochem. Soc.*, **1982**, *129*, 2169.

25 M. Barroso, S. R. Pendlebury, A. J. Cowan and J. R. Durrant, *Chem. Sci.*, **2013**, *4*, 2724.

26 M. Catti, G. Valerio and R. Dovesi, *Phys. Rev. B*, **1995**, *51*, 7441.

27 Z. Y. Wu, S. Gota, F. Jollet, M. Pollak, M. Gautier-Soyer and C. R. Natoli, *Phys. Rev. B*, **1997**, *55*, 2570.

28 Y. Ma, P. D. Johnson, N. Wassdahl, J. Guo, P. Skytt, J. Nordgren, S. D. Kevan, J. E. Rubensson, T. Böske and W. Eberhardt, *Phys. Rev. B*, **1993**, *48*, 2109.

29 K. L. Hardee and A. J. Bard, *J. Electrochem. Soc.*, **1976**, *123*, 1024.

30 R. K. Quinn, R. D. Nasby and R. J. Baughman, *Mater. Res. Bull.*, **1976**, *11*, 1011.

31 J. H. Kennedy, R. Shinar and J. P. Ziegler, *J. Electrochem. Soc.*, **1979**, *127*, 2307.

32 M. V. C. Sadn and G. Nagasubramanian, Adv. Hydrogen Energy, **1981**, *2*, 597.

33 M. P. Dare-Edwards, J. B. Goodenough, A. Hamnett and P. R. Trevellick, *J. Chem. Soc., Faraday Trans. 1*, **1983**, *79*, 2027.

34 N. J. Cherepy, D. B. Liston, J. A. Lovejoy, H. Deng and J. Z. Zhang, *J. Phys. Chem. B*, **1998**, *102*, 770.

35 A. G. Joly, J. R. Williams, S. A. Chambers, G. Xiong, W. P. Hess and D. M. Laman, *J. Appl. Phys.*, **2006**, *99*, 053521.

36 S. R. Pendlebury, M. Barroso, A. J. Cowan, K. Sivula, J. Tang, M. Grätzel, D. Klug and J. R. Durrant, *Chem. Comm.*, **2011**, *47*, 716.

37 R. Shinar and J. H. Kennedy, *Sol. Energ. Mater.*, **1982**, *6*, 323.

38 F. J. Morin, *Phys. Rev.*, **1951**, *83*, 1005.

39 K. Sivula, R. Zboril, F. Le Formal, R. Robert, A. Weidenkaff, J. Tucek, J. Frydrych and M. Grätzel, *J. Am. Chem. Soc.*, **2010**, *132*, 7436.

40 D.-D. Qin, C.-L. Tao, S.-i. In, Z.-Y. Yang, T. E. Mallouk, N. Bao and C. A. Grimes, *Energ. Fuel.*, **2011**, *25*, 5257.

41 A. Bak, W. Choi and H. Park, *Appl. Catal. B-Environ.*, **2011**, *110*, 207.

42 F. L. Souza, K. P. Lopes, P. A. P. Nascente and E. R. Leite, *Sol. Energy. Mater. Sol. Cells*, **2009**, *93*, 362.

43 P. Kumar, P. Sharma, R. Shrivastav, S. Dass and V. R. Satsangi, *Int. J. Hydrogen Energ.*, **2011**, *36*, 2777.

44 H. Tang, M. A. Matin, H. Wang, T. Deutsch, M. Al-Jassim, J. Turner and Y. Yan, *J. Appl. Phys.*, **2011**, *110*, 123511.

45 J. A. Glasscock, P. R. F. Barnes, I. C. Plumb and N. Savvides, *J. Phys. Chem. C*, **2007**, *111*, 16477.

46 N. T. Hahn and C. B. Mullins, *Chem. Mater.*, **2010**, *22*, 6474.

47 O. Zandi, B. M. Klahr and T. W. Hamann, *Energ. Environ. Sci.*, **2013**, *6*, 634.

48 K. Itoh and J. O. Bockris, *J. Electrochem. Soc.*, **1984**, *131*, 1266.

49 C. J. Sartoretti, M. Ulmann, B. D. Alexander, J. Augustyski and A. Weidenkaff, *Chem. Phys. Lett.*, **2003**, *376*, 194.

50 A. Duret and M. Grëtzel, *J. Phys. Chem. B*, **2005**, *109*, 17184.

51 S. D. Tilley, M. Cornuz, K. Sivula and M. Grätzel, *Angew. Chem., Int. Ed.*, **2010**, *49*, 6405.

52. U. Bjoerksten, J. Moser and M. Grätzel, *Chem. Mater.*, **1994**, *6*, 858.

53 F. L. Souza, K. P. Lopes, P. A. P. Nascente and E. R. Leite, *Sol. Energy. Mater. Sol. Cells*, **2009**, *93*, 362.

54 D. K. Bora, A. Braun, S. Erat, A. K. Ariffin, R. Lonhert, K. Sivula, J. Topfer, M. Grätzel, R. Manzke, T. Graule and E. C. Constable, *J. Phys. Chem C*, **2011**, *115*, 5619.

55 L. Vayssieres, A. Hagfeldt and S. E. Lindquist, *Pure Apll. Chem.* , **2000**, *72*, 47.

56 N. Beermann, L. Vayssieres, S. E. Lindquist and A. Hagfeldt, *J. Electrochem. Soc.*, **2000**, *147*, 2456.

57 C. Toussaint, H. L. L. Tran, P. Colson, J. Dewalque, B. Vertruyen, B. Gilbert, N. D. Nguyen, R. Cloots and C. Henrist, *J. Phys. Chem. C*, **2014**, *119*, 1642.

58 N. Dalle Carbonare, V. Cristino, S. Berardi, S. Carli, R. Argazzi, S. Caramori, L. Meda, A. Tacca and C. A. Bignozzi, *ChemPhysChem.*, **2014**, *15*, 1164.

59 E. S. Cho, M. J. Kang and Y. S. Kang, *Phys. Chem. Chem. Phys.*, **2015**, *17*, 16145.

60 Y. Ling, G. Wang, J. Reddy, C. Wang, J. Z. Zhang and Y. Li, *Angew. Chem. Int. Ed.*, **2012**, *51,* 4074.

61 J. Brillet, M. Grätzel and K. Sivula, *Nano Lett.*, **2010**, *10*, 4155.

62 T. Vincent, M. Gross, H. Dotan and A. Rothschild, *Int. Journal Hydrogen Energ.*, **2012**, *37*, 8102.

63 X. Wen, S. Wang, Y. Ding, Z. L. Wang and S. Yang, *J. Phys. Chem. B*, **2005**, *109*, 215.

64 T. J. LaTempa, X. Feng, M. Paulose and C. A. Grimes, *J. Phys. Chem. C*, **2009**, *113*, 16293.

65 B. Klahr, S. Gimenez, F. Fabregat-Santiago, T. W. Hamann and J. Bisquert, *Energy Environ. Sci.*, **2012**, *5*, 7626.

66 H. Dotan, K. Sivula, M. Grätzel, A. Rothschild and S. C. Warren, *Energy Environ. Sci.*, **2011**, *4*, 958.

67 H. Yamazaki, A. Shouji, M. Kajita and M. Yagi, *Coordin. Chem. Rev.*, **2010**, *254*, 2483.

68 T. Nakagawa, C. A. Beasley and R. W. Murray, *J. Phys. Chem. C*, **2009**, *113*, 12958.

69 K. M. H. Young and T. W. Hamann, *Chem. Comm.*, **2014**, *50*, 8727.

70 F. Malara, A. Minguzzi, M. Marelli, S. Morandi, R. Psaro, V. Dal Santo and A. Naldoni, *ACS Catal.*, **2015**, *5*, 5292.

71 M. Gong and H. Dai, *Nano Res.*, **2014**, *8*, 23.

72 W. Li, S. W. Sheehan, D. He, Y. He, X. Yao, R. L. Grimm, G. W. Brudvig and D. Wang, *Angew. Chem. Int. Ed.*, **2015**, *54*, 11428.

73 B. Zhang, F. Li, F. Yu, X. Wang, X. Zhou, H. Li, Y. Jiang and L. Sun, *ACS Catal.*, **2014**, *4*, 804.

74 X. Chen, X. Ren, Z. Liu, L. Zhuang and J. Lu, *Electrochem. Comm.*, **2013**, *27*, 148.

75 V. Cristino, S. Marinello, A. Molinari, S. Caramori, S. Carli, R. Boaretto, R. Argazzi, L. Meda and C. A. Bignozzi, *J. Mater. Chem. A*, **2016**, DOI: 10.1039/C5TA06887H.

76 A. Prevedello, I. Bazzan, N. Dalle Carbonare, A. Giuliani, S. Bhardwaj, C. Africh, C. Cepek, R. Argazzi, M. Bonchio, S. Caramori, M. Robert and A. Sartorel, *Chem.-Asian J.*, **2016**, DOI: 10.1002/asia.201501446R1.

77 B. Klahr, S. Gimenez, F. Fabregat-Santiago, T. Hamann and J. Bisquert, *J. Am. Chem. Soc.*, **2012**, *134*, 4294.

78 F. Le Formal, N. Tétreault, M. Cornuz, T. Moehl, M. Grätzel and K. Sivula, *Chem. Sci.*, **2011**, *2*, 737.

79 T. Hisatomi, F. Le Formal, M. Cornuz, J. Brillet, N. Tétreault, K. Sivula and M. Grätzel, *Energy Environ. Sci.*, **2011**, *4*, 2512.

80 M. Barroso, C. A. Mesa, S. R. Pendlebury, A. J. Cowan, T. Hisatomi, K. Sivula, M. Grätzel, D. R. Klug and J. R. Durrant, *PNAS*, **2012**, *109*, 15640.

81 B. Klahr, S. Gimenez, F. Fabregat-Santiago, J. Bisquert and T. W. Hamann, *J. Am. Chem. Soc.*, **2012**, *134*, 16693.

82 K. Sivula, *J. Phys. Chem. Lett.*, **2013**, *4*, 1624.

83. P. Liao, J. A. Keith and E. A. Carter*, J. Am. Chem. Soc.*, **2012**, *134*, 13296.

84 A. Hellman and R. G. S. Pala, *J. Phys. Chem. C*, **2011**, *115*, 12901.

85 R. Nakamura and Y. Nakato, *J. Am. Chem. Soc.*, **2004**, *126*, 1290.

86 K. G. Upul Wijayantha, S. Saremi-Yarahmadi and L. M. Peter, *Phys. Chem. Chem. Phys.*, **2011**, *13*, 5264.

87 C. Y. Cummings, F. Marken, L. M. Peter, K. G. Upul Wijayantha and A. A. Tahir, *J. Am. Chem. Soc.*, **2012**, *134*, 1228.

88 F. Le Formal, E. Pastor, S. D. Tilley, C. A. Mesa, S. R. Pendlebury, M. Grätzel and J. R. Durrant, *J. Am. Chem. Soc.*, **2015**, *137*, 6629.

89 S. R. Pendlebury, A. J. Cowan, M. Barroso, K. Sivula, J. Ye, M. Grätzel, D. R. Klug, J. Tang and J. R. Durrant, *Energy Environ. Sci.*, **2012**, *5*, 6304.

90 L. M. Peter, K. G. U. Wijayantha and A. A. Tahir, *Faraday Discuss.*, **2012**, *155*, 309.

CHAPTER 4

SCOPE AND SUMMARY OF THE THESIS

My PhD research work has been mainly focused on the investigation of charge transfer dynamics in nanostructured hematite thin film modified with amorphous and crystalline structures of iron(III) oxides for the photo-induced oxidation of water.

Hematite is a well known semiconductor that has gained a lot of popularity in the last decades as a promising material for the photo-oxidation of water. The solar water splitting process represents an interesting and elegant way to exploit the enormous power of the sun to obtain molecular hydrogen from the decomposition of water molecules in their elementary components, without the production of polluting by-products and, in principle, without the need of external additional energy. Different strategies have been proposed to solve several issues ascribed to intrinsic properties of hematite that limit its application in photoelectrochemical devices. Among the others, the most incisive were proven to be: (i) the development of synthetic procedures able to obtain a rough morphology, thus allowing to work with films thick enough to absorb a sufficient amount of light, (ii) the application on the semiconductor surface of species able to catalyse the water oxidation reaction, known to be very slow at the hematite

surface and (iii) the introduction of external doping elements to improve the electronic conductivity of the material, reducing the probability of electron/hole losses due to recombination. Following these guidelines, we have analyzed different aspects usually limiting the efficiency of photoanodes based on iron oxides, proposing cheap and simple solutions to alleviate the limitations listed above.

We decided to set up our research on few key points. Our main objective was the use of solution-based procedures for both the preparation of hematite films and their further modification. This decision was guided by the possibility to drastically reduce, first of all, the cost of the synthetic process, with respect to vapour-based techniques. These latter techniques have demonstrated to produce hematite electrodes with the best performances reported so far, but the necessity of dedicated instrumentation, the severe control of the conditions (i.e. temperature, pressure) and the use of not-benign precursors and solvents (DMF) represents, in our opinion, a weak point for a future large scale production and application. On the other hand, we have utilized simple instrumentations, common laboratory glassware and fast procedures that are suitable for scaling-up both the synthesis and the successive modification processes. Moreover, we have employed in all the different preparative steps only aqueous solutions of iron(III) precursors that are abundant, cheap and environmental friendly. A clean and sustainable way to produce hydrogen cannot be based on devices built with precious or harmful components, but instead it has to take advantage of earth-abundant elements, such as iron.

At a first stage, we tried different methods to prepare films with appropriate thickness and morphology, such as the dip coating of an alcoholic solution of iron(III) chloride onto a heated FTO: the lack of homogeneity of the resulting films encouraged us to explore different synthetic ways. Using a wet procedure based on the growth of iron oxide directly on the FTO substrate, we finally obtained finally good catalytic crystalline films, characterized by a rough morphology made of iron oxide nanorods with an overall thickness of ca. 300 nm. The excellent reproducibility and the good performances,

combined with the facility of the synthetic procedure, fulfilled our requirements. These samples were tested as batch for the implementation of an oxygen evolving catalyst based on hydrated iron(III) oxides. Different catalysts based on various metals (such as ruthenium, iridium, nickel and cobalt) have been coupled so far with hematite and other n-type semiconductors, showing good improvement in the water oxidation activity due to their very low overpotential required to trigger this reaction. Our proposed catalyst presents additional characteristics that make it even more attractive: its amorphous nature reduces it light absorption capability, important to avoid interference with the semiconductor in the photogeneration process and, as previous said, it can be deposited with an impregnation methodology, using just aqueous solutions. Moreover, iron is the fourth most abundant metal on our planet, and the possibility to develop a device completely based on it was an additional pros. In Chapter 5 are reported the results obtained with this system and its characterization. The better performances achieved after the functionalization of the electrode with the hydrated iron(III) oxides (0.8 mA cm^{-2} at 0.8 V vs. SCE in 0.5 M borate buffer, pH 11.5) can be ascribed to the capability of the latter to store photogenerated holes in a more suitable environment for the oxidation of water with respect to the iron of the hematite lattice, probably due to its amorphous nature of the catalyst. Complementary flash photolysis experiments support our interpretation, showing how it is possible to obtain efficient catalytic systems based on earth-abundant elements using simple and cost-effective procedures.

We then decided to concentrate our interest on the hematite/FTO interface rather then on the SCLJ. Indeed, defects due to a mismatch between the lattices of the two oxides on the former interface may act as recombination centres, thus limiting the electron collection capability of the photoanode. We tested the role of a thin layer of crystalline iron oxide (ca. 30 nm), deposited by spin coating technique from an aqueous solution of iron(III) chloride modified with PEG. The successive deposition of the mesoporous film of hematite was performed with an electrophoretic methodology, using a colloid solution of iron oxide nanoparticles that, after the application of a suitable potential, stack on the negatively polarized FTO. Also in this case, the morphology

obtained addresses our requirements and, although the performances of the resulting bare hematite were lower if compared to the hydrothermally grown samples (coherent with previous reports), the great improvement in the photocurrent was very surprising, reaching photocurrent density of ca. 1 mA cm^{-2} at 0.65 V vs. SCE. The effects of metal oxide underlayers coupled with very thin hematite films have been reported in the literature and have been ascribed to the diffusion of doping elements from the underlayer to the hematite film or to an improvement in the hematite crystallinity due to a template effect of the underlayer during the deposition/growth process. Differently from these previous studies, we decided to keep the thickness of the hematite film around 300 nm, to ensure good light harvesting efficiency, and to test an underlayer based on iron (instead of Nb, Ga or Si as reported so far). Although the conditions of the different preparative steps cannot be rigorously controlled, the reproducibility was anyway excellent. We did not actually observe improvements neither in the crystallinity of the film or in its doping density but, instead, electrochemical characterization showed that the underlayer assists the charge separation process developing an active space charge region that generates an additive driving force to extract electrons from the photoanode, thus reducing the electron/hole recombination. This proposed interpretation gives new insights about the mechanistic role of the underlayer on the overall charge dynamic properties of the photoanode. The subsequent addition of the catalyst onto the hematite surface allows us to obtain photocurrent values among the highest reported using only solution based procedures, around 1.5 mA cm^{-2} in NaOH 0.1 M (pH 13.3). The combination of different structures based only on iron represents a smart way to explore and maximize the performance of this type of electrodes. Morphological investigation of the samples employing SEM, Micro-Raman and XRD spectroscopy, combined with photoluminescence spectroscopy resulted in a coherent and exhaustive description of the phenomena observed and described in detail in Chapter 6.

The third aspect studied in Chapter 7 concerns the determination of the effect of the introduction of a Ti(IV) precursor during the electrophoretic deposition of iron oxide

on FTO. Doping n-type semiconductor with different elements is a common strategy to improve the electrocatalytic activity, although the exact effect of these external agents is still not well understood. In principle, Ti(IV) (as many other cations) can enter in the hematite crystal enhancing the electronic conductivity of the material with benefits for the efficiency in charge separation processes. However, it is also possible the formation of a pure or mixed phase of TiO_2 on the hematite surface, in particular with post-synthetic treatments followed by high temperature annealing. The deposition of thin metal oxides onto the semiconductor surface can be beneficial too due to the passivation of recombination centres present in defective surface states. Under this point of view, it is not always correct to talk about doping, because it's necessary to clearly discern between the two different effects explained above. We thus prepared electrophoretic hematite films by introducing in the deposition solution a Ti(IV) butoxide: the photoelectrochemical performances of the modified electrodes were superior to un-modified hematite film, for all the different concentration of Ti(IV) tested. AFM and XPS morphological investigation reveal the formation of a Ti(IV) containing phase on the hematite surface, that reduces the surface state recombination and enhances the charge transfer rate resulting in improved photocurrent, as confirmed by EIS analysis. M-S plot testified a 3-fold increase in the donor density in the modified sample, indicating a better conductivity, which may also contribute to explain the enhanced response. Thus, the introduction of Ti(IV) probably affects the photoelectrochemical properties of the film by playing multiple roles: it acts both as an interfacial modifier, resulting in improved kinetics and, probably, as a lattice dopant, although this latter role may be secondary with respect to the former. The combination of these two effects together with functionalization with Fe-OEC produce modified electrode able to reach ca. 1.5 mA cm^{-2} at 0.65 V vs. SCE in NaOH 0.1 M (pH 13.3), one of the highest photocurrent achieved with only solution based procedure and without the addition of precious elements.

Finally, in collaboration with Dr. Michele Orlandi from Id.E.A. laboratories of the University of Trento, we studied the behaviour of nanostructured amorphous iron oxide catalyst deposited by PLD (Pulsed Laser Deposition) on hematite electrodes. PLD is a

vapor deposition technique that employs a pulsed laser beam inside a vacuum chamber to strike a target of the material that has to be deposited. Although this technique needs specialized equipment, it offers some advantages with respect to SILAR or other solution-based deposition techniques (i.e. electrodeposition, PMOD) for the deposition of catalysts on solid substrates, such as hematite electrodes. These advantages reside mainly in the possibility to obtain complete and homogeneous surface coverage, to precisely control the quantity of the deposited material and most importantly, to nanostructure the surface by the deposition of nanoparticles. Finally, different species are accessible by varying the experimental conditions (such as the background gas9 with precise and controlled stoichiometry. The purpose of our study was the implementation of a transparent and amorphous iron oxide catalyst onto hematite photoanodes, to obtain a homogeneous coverage of the semiconductor surface for a better catalytic activity. Beyond the catalytic properties, an important characteristic for catalysts, when coupled to photoactive materials, is the absence of optical absorption features, to avoid parasitic phenomena of light absorption, limiting the efficiency of the PEC device. The different morphologies obtained by PLD varying the temperature conditions during and after the deposition process enormously affect both the optical properties of the species and their electrochemical behavior. Chapter 8 reports the morphological and electrochemical characterization of these iron oxides and the first results obtained in combination with mesoporous hematite photoanodes. Reducing the dimensions of the iron oxide catalyst has proven to be a feasible strategy to obtain transparent coatings, although successive thermal treatment is needed to enhance the stability. Their application on hematite photoanodes shows interesting enhancement of the photoactivity with respect to denser catalytic samples, probably due to a blocking effect in the absorption process. Further investigations is currently underway to assess if the different morphology of the catalyst also influence the charge transfer dynamics at the hematite/catalyst/solution interface.

Experimental details and theoretical aspects of some of the employed characterization techniques, with particular focus on the electrochemical methods, are reported in Chapter 9, with a list of chemicals and materials used in the different

preparative steps. Details of the preparation and modification procedures are instead discussed in the respective chapters (5-8).

CHAPTER 5

HEMATITE PHOTOANODES MODIFIED WITH AN IRON(III) WATER OXIDATION CATALYST

this chapter is based on: N. Dalle Carbonare, V. Cristino, S. Berardi, S. Carli, R. Argazzi, S. Caramori, L. Meda, A. Tacca and C. A. Bignozzi *ChemPhysChem.*, **2013**, *15*, 1164.

5.1 Introduction

Currently, the optimal OECs are based on RuO_2 and IrO_2, since these materials exhibit the lowest overpotentials for the OER at practical current densities. However, the high cost and low natural abundance of these materials renders their widespread commercial utilisation both uneconomical and impractical. In light of these limitations, the oxides of the first row transition metals offer a compromise solution: although they possess inferior electrocatalytic activity for the OER, their relatively low-cost and long-term corrosion resistance in alkaline solution makes them attractive catalysts. Moreover, in the past few years, special interest has grown on the synthesis and application of amorphous materials for electrocatalysis, due to their better performance in terms of overpotential and Tafel slope values.[1]

Besides their well-known catalytic properties in oxidation reactions, [2-4] Fe(III) oxides are very attractive materials also due to their non-toxicity and environmentally benign nature. The electrocatalytic properties of these amorphous Fe(III) oxides reside mainly in

the achievement of a good permeation by the solvent and in the capability to store multiple oxidizing equivalents, by reaching highly valent oxidation states able to initiate oxidation reactions. Cristino *et al.* in 2013 successfully employed amorphous iron(III) oxides in the functionalization of ITO (Indium Tin Oxide) surfaces and of triple junction cells showing the great potentiality in the application of this type of catalysts on photoactive material for solar water splitting. [5]

Since, to the best of our knowledge, there were no reports in the literature about the application of these species on hematite substrates so far, we decided to investigate the effect of the functionalization of nanocrystalline hematite electrodes obtained by hydrothermal route with a Fe(III) oxygen evolving catalyst, essentially consisting of hydrated amorphous Fe(III) oxides, deposited by SILAR (Successive Ionic Layer Adsorption and Reaction) procedure. This technique exhibits several advantages over more common (photo)- electrochemical deposition techniques[6] since (i) it is fast, (ii) it does not require electrochemical equipment or the use of toxic chemicals and (iii) it can be easily scaled up to large surfaces. The modification of our hematite electrodes results in a considerable enhancement of the photoelectrochemical activity of the pristine photoanodes. Insights about charge transfer dynamics at the modified interface have been obtained by combining conventional DC photoelectrochemical measurements, Electrochemical Impedance Spectroscopy (EIS) and nanosecond Laser Flash Photolysis (LFP).

5.2 Synthesis and functionalization procedures of hematite films

Nanocrystalline wormlike hematite thin films were deposited on FTO substrates according to a simple solution-based procedure devised by Vayssieres *et al.*[7] (see chapter 3.4.3) as follows: FTO glass slides (*ca*. 2.5 x 4 cm) were carefully cleaned by subsequent ultrasonic treatments with acetone, ethanol and aqueous Alconox® and blown dry with a hot dry air stream. A portion of the slide (4 x 1 cm) was masked with KAPTON tape (Tesa) to preserve an uncovered zone of the FTO for the electric contact. The resulting FTO slides were placed in a round bottom flask and covered with 30 mL of

an aqueous solution containing 0.15 M $FeCl_3 \cdot 6H_2O$ and 1 M of sodium nitrate at pH ca. 1.3 and heated at constant 95 °C without stirring for 4 hours. At the end of the reaction the resulting FTO slides were rinsed several times with distilled water, dried, annealed at 500 °C for 2 hours in air and then annealed again at 800 °C for 1 hour.

Nanocrystalline hematite electrodes were functionalized with iron(III) hydrous oxide (generally indicated as $(Fe_2O_{3-x}(OH)_x^* x(H_2O)$, Fe-OEC) by using 10 cycles of SILAR deposition.[8] Each SILAR cycle consisted in the immersion of the electrode (1 x 1.5 cm) for 10 seconds in a 50 mM $FeCl_3$ aqueous solution, followed by dipping (10 seconds) in 0.1 M NaOH (pH 13). After each cycle the electrode was rinsed with abundant distilled water to remove weakly interacting macroscopic deposits from its surface. After completion of the SILAR cycles, the modified electrodes were annealed in air at 200 °C for 20 minutes in order to improve the adhesion and the consolidation of the Fe(III) catalyst on the hematite surface.

5.3 Morphology of hydrothermally-prepared hematite film

Briefly, the hydrothermal preparation of hematite resides in the hydrolysis of an ionic Fe(III) precursor, in the presence of an electrolyte buffer, resulting in the nucleation and growth of iron(III) oxy-hydroxide (β-FeOOH, akaganeite) nanoparticles on the FTO surface exposed to the solution. This metastable iron oxide phase appears on the glass transparent substrate as a pale yellow film. A subsequent annealing at 500 °C induces its decomposition and the formation of nanocrystalline hematite (α-Fe_2O_3), characterized by an orange color that keeps a discrete transparency (Figure 5.1).

In the present study we selected the hydrothermal route to the synthesis of hematite thin films since: 1) it represents a facile and convenient way to the quick preparation of photoanodes having a reasonable photoelectrochemical response; 2) it virtually requires no specific equipment with easily controlled process variables, essentially temperature and composition of the aqueous Fe(III) precursor solution; 3) it can be scaled to large

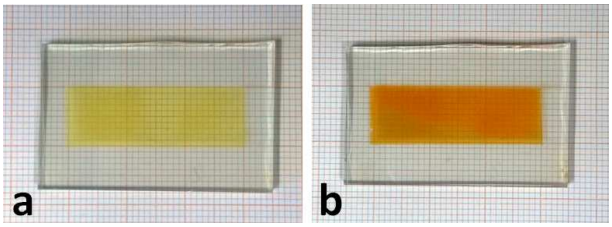

Figure 5.1. Aspect of iron(III) oxy-hydroxide film (a) before and (b) after annealing at 500 °C.

surfaces employing cheap reactants and harmless solvents (water). It represents thus a convenient procedure for producing basic photoanodes that serve as test beds for subsequent surface functionalization with electroactive species, for the purpose of investigating the charge transfer dynamics at the modified interfaces.

The SEM images of hematite thin films deposited on FTO after 500 °C annealing, taken at x50 k, are shown in Figure 5.2 (a-b). It is evident a nanostructured morphology constituted by elongated irregular features (ca. 100 X 20 nm) which are partially aggregated resulting in larger conglomerates irregularly distributed on the surface.

XRD analysis (Figure 5.3) indicates coherent scattering domains of 18-20 nm, meaning that each conglomerate is actually constituted by small nanocrystals, whose size, evident under high magnification and high resolution imaging at x200 k (Figure 5.4), is roughly consistent with XRD results. The thickness of the active film, estimated by cross sectional imaging, is about 250-270 nm, whereas the FTO, which can be clearly distinguished from hematite due to the large size of its crystallites, is 600-650 nm thick (Figure 5.2-b).

Although the 500 °C electrode exhibited a good crystallinity and an average feature size that can potentially generate a remarkable photocurrent, considering a hole diffusion length L_h of 2-4 nm,[9] the photoelectrochemical properties were very poor, resulting in photoanodic currents of few μA under AM 1.5G illumination (100 mW cm^{-2}). However, it was first reported by Grätzel[10] that a large improvement in the photoanodic response could be induced on either colloidal or hydrothermal hematite following heat treatment at 800 °C. The reason of the improved response is complex and probably originated by a combination of factors. Nevertheless, Sn(IV) diffusion and doping from the underlying FTO/glass substrate, brought close to melting conditions, is believed to play the major role in increasing the photoanodic response. Another factor, which secondarily

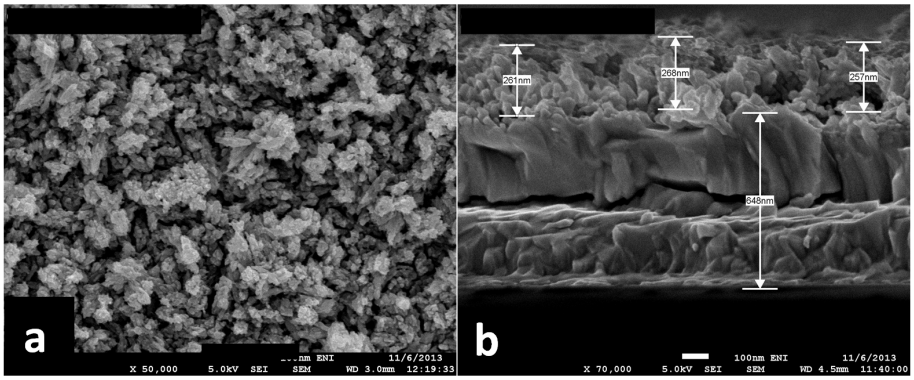

Figure 5.2. (a) SEM micrographs of hematite surface annealed at 500 °C (x 50 k) and (b) cross sectional view.

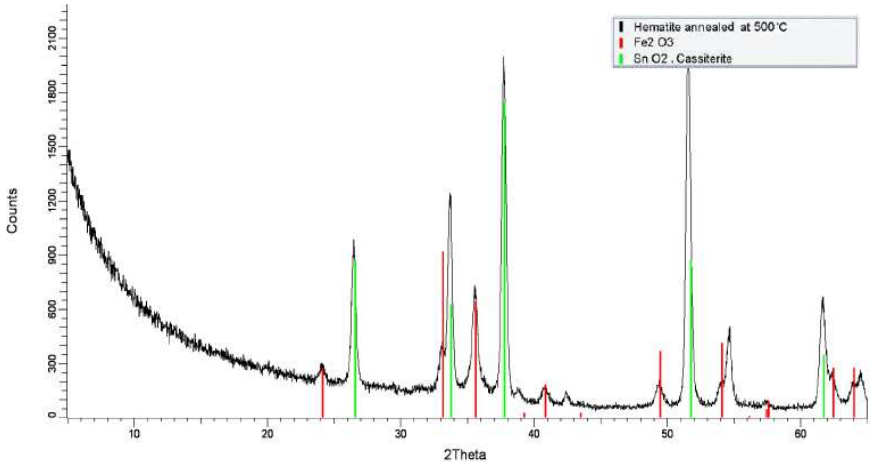

Figure 5.3. XRD of hydrothermal hematite thin film on FTO annealed at 500 °C for 2 hours.

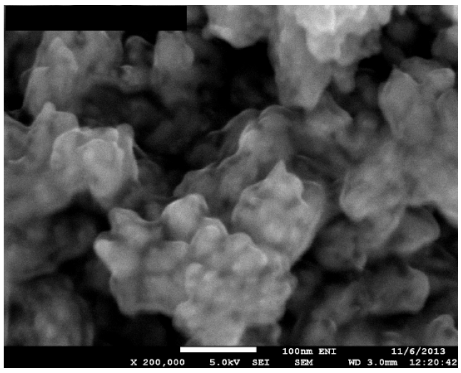

Figure 5.4. SEM micrograph of hydrothermal hematite after 500 °C annealing (x 200 k).

contributed to the enhanced performances, was the introduction of a permanent trigonal distortion along face sharing octahedra (Fe_2O_9), which resulted in improved optical properties of thin films (increased intensity and red shift of optical transitions).

The SEM image of hematite thin film annealed at 800 °C is shown in Figure 5.5-a. It is clear that the heat treatment not only increased the size of the agglomerates but also modified the morphology with respect to the parent surface treated at 500 °C (Figure 5.1). Two different nanoparticle morphologies and size distributions, with random orientations, are evident, with larger needle-like conglomerates (ca. 300 x 50 nm) associated to smaller, roughly spherical particles with a diameter of ca. 50 nm. The surface of these nanostructures is also smoother and less porous, as confirmed by high resolution imaging reported in Figure 5.5-b and XRD analysis (Figure 5.6), consistent with the presence of larger coherent scattering domains sizing up to 35 nm. The cassiterite signals were also stronger due to the partial melting and surfacing of the FTO at 800 °C. For this reason, we were unable to clearly observe the discontinuity between the hematite thin film and the underlying FTO. Nevertheless, it can be reasonably assumed that the thickness of the photoactive material is not substantially changed by the 800 °C thermal treatment. Finally, the colour of the hematite thin film changed from orange to deep red.

The SEM image of the hematite electrode functionalized with iron(III) hydrous oxide (Fe-OEC) by using 10 cycles of SILAR deposition and annealed at 200 °C is reported in Figure 5.7, where it is possible to observe the presence of irregular features, attributed to the presence of an amorphous Fe(III) oxide phase (outlined by white circles), which cover the nanocrystalline network of hematite. High resolution imaging at x200 k (Figure 5.7-b) confirms this observation showing an irregular and porous encrustation of nanometric thickness (indicated by the arrow), covering the underlying crystalline structures. The amorphous nature of the Fe-OEC deposited by SILAR procedure using NaOH is maintained after the annealing at 200°C as probed elsewhere using both IR and Raman spectroscopy and XPS and XRD spectroscopy.[5]

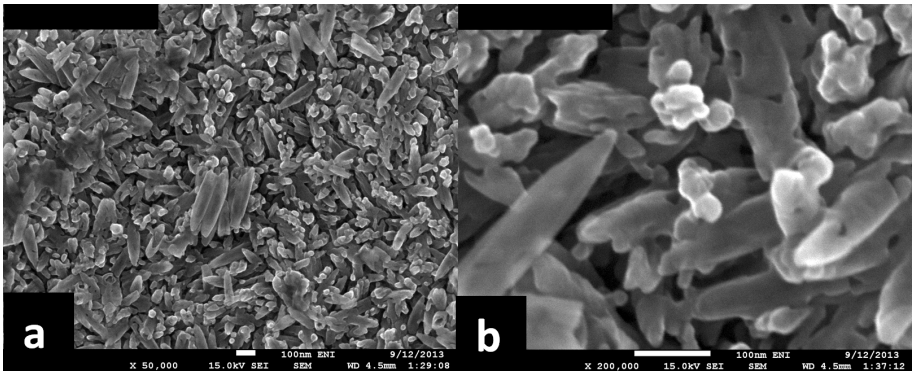

Figure 5.5. SEM micrographs of hematite surface annealed at 800 °C.

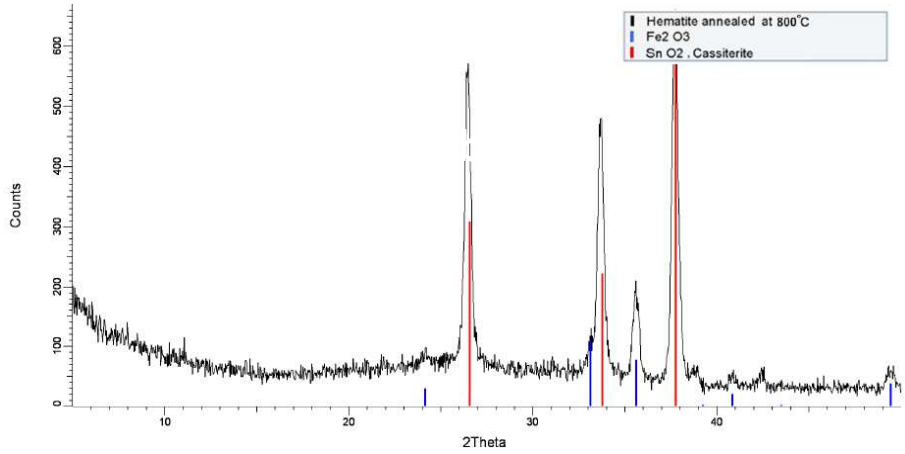

Figure 5.6. XRD of hydrothermal hematite thin film on FTO annealed at 800 °C for 1 hour. Expansion of the 2θ scale between 0 and 50°.

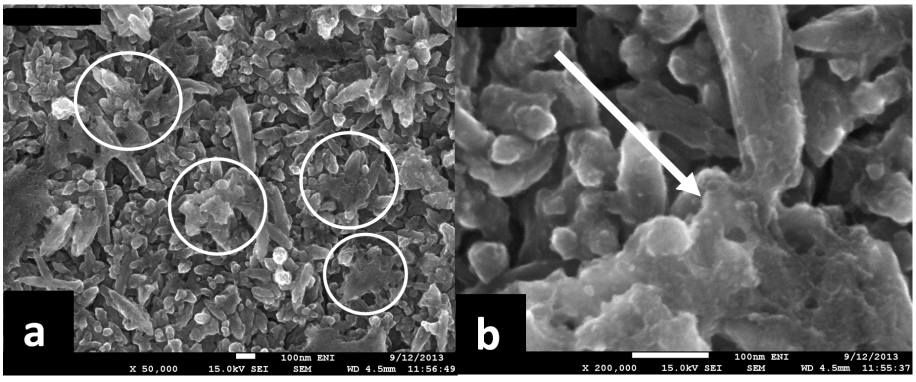

Figure 5.7. SEM micrographs of hematite annealed at 800 °C followed by functionalization with Fe-OEC and annealing at 200 °C for 20 minutes.

5.4 Photoelectrochemistry of pristine and modified hematite electrodes

The *J-V* curves of the same hematite photoanode prior and after surface modification with Fe-OEC, recorded in 0.5 M sodium borate buffer (pH 11.5) under AM 1.5G illumination, are shown in Figure 5.8-a. The surface modification with the water oxidation catalyst nearly doubles the photoanodic response of the original photoelectrode within the whole explored potential interval. The maximum photocurrent produced in borate buffer at 0.8 V vs. SCE reaches ca. 0.8 mA cm^{-2}, whereas the unmodified hematite is limited to ca. 0.35 mA cm^{-2}. The rectangular shaped photocurrent transients recorded under shuttered illumination show a good matching with the steady state *J-V* curves. The threshold of the appearance of photoanodic transients, which represents a lower estimation of the V_{fb} of the semiconductor, is located at about 0 V vs. SCE and, in both cases, is nearly coincident. This rules out a substantial modification of the Fermi level of hematite due to surface modification with the catalyst. The steady state photocurrent recorded at 0.7 V vs. SCE was substantially stable under prolonged illumination conditions (8 hours) (Figure 5.8-b) ruling out photocorrosion involving the catalyst. As expected, in both cases the magnitude of the photocathodic spikes, observed when the illumination is turned off, which is ascribed to electron-hole recombination, decreases with increasing potential bias. In addition, their amplitude, relative to the amplitude of the photoanodic transients, is reduced by a ca. x 2 factor in the presence of the catalyst, suggesting an improved interfacial hole scavenging.

Entirely analogous observations can be extended to the other electrolytes, explored in this study (0.5 M Na_2CO_3 and 0.1 M NaOH), allowing to exclude, as a first approximation, specific electrolyte effects on the catalyst mediated charge transfer kinetics due to buffering, specific ionic adsorption or modifications of the structure of the Helmholtz layer (Figure 5.9). Indeed, in all cases, the relative improvement of the photoanodic current due to the presence of Fe-OEC is nearly the same (a photocurrent doubling) although the highest photocurrent density was recorded in NaOH, where plateau values close to 1 mA cm^{-2} were obtained. It should be noted that data are referred to the same photoelectrode before and after surface modification. This choice was motivated by the

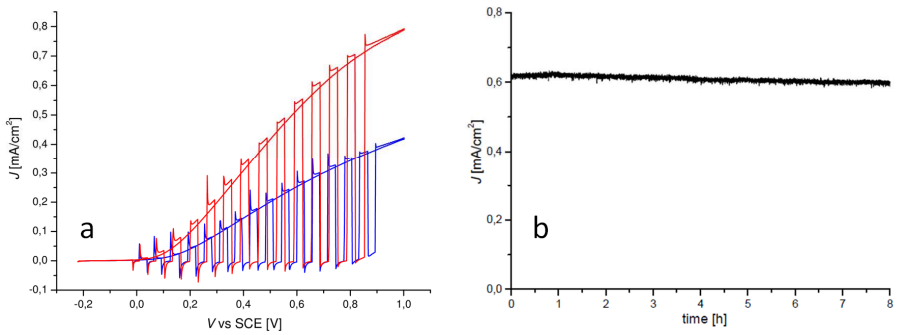

Figure 5.8. (a) *J-V* curves under continuous and shuttered illumination of Fe-OEC modified hematite (red line) compared to the unmodified hematite (blue line) and (b) chronoamperometry at 0.7 V vs. SCE of hematite photoanode modified with Fe-OEC recorded in 0.5 M sodium borate buffer (pH 11.5).

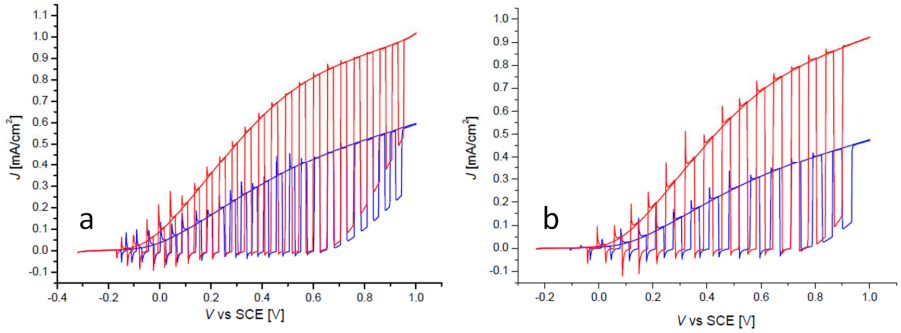

Figure 5.9. *J-V* curves under continued and shuttered illumination of the same hematite photoanode before (blue line) and after (red line) surface modification with Fe-OEC recorded in (a) 0.1 M NaOH (pH 13.1) and (b) 0.5 M Na_2CO_3 (pH 11.5).

need of individuating the net repercussions of the surface modification with the water oxidation catalyst, by minimizing possible variability in performance arising from the use of different batches of baseline electrodes (unmodified hematite), prepared in different days. It should also be noted that the experiments were repeated on several different photoelectrodes and that the relative improvement in electrode performance induced by the presence of the catalyst was reproducible.

The IPCE spectra, recorded in the presence of a constant bias at 0.7 V vs. SCE (Figure 5.10-a), are consistent with the photocurrent doubling observed in *J-V* curves. The IPCE generated by the Fe-OEC modified hematite reaches maximum values equal to 23 % at 350 nm and more than doubles in the visible region, passing from 7-8 % to 16-12 %. The action spectra are in reasonable agreement with the absorption spectrum (Figure 5.10-b),

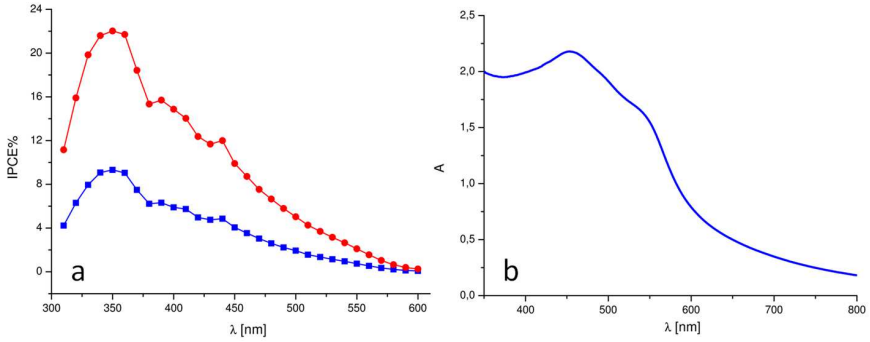

Figure 5.10. (a) IPCE spectra of Fe-OEC modified hematite (red circles) compared to the same electrode before functionalization with the Fe(III) catalyst (blue squares) recorded in sodium borate buffer under 0.7 V vs. SCE potential bias. (b) UV-Visible absorption spectrum of hematite thin film on FTO after 800 °C annealing.

showing a secondary absorption maximum at about 450 nm, with an absorption tail reaching 600 nm. Compared to the parent electrode, the presence of the catalyst does not alter the shape of the spectral response of the modified photoelectrode, indicating that the light absorption is not substantially influenced by the presence of Fe-OEC. This is an important feature to evaluate for the application of a catalyst onto a photo-electrode, because the eventually possible parasitic light absorption of the catalyst specie can compromise the light harvesting efficiency of the substrate, limiting the charge generation (e.g. Co-Pi). In our case Finally, given that the light harvesting efficiency is nearly unitary up to 550 nm (Figure 5.10-b), it can be appreciated that most of the charge carriers (ca. 75-80%) generated upon photoexcitation recombine, despite the presence of the hole transfer catalyst, indicating that the potentialities of hematite as a photoanodic material are still far from being fully exploited.

The study of photovoltage transients (normalized data in Figure 5.11) under open circuit conditions was used to gain initial insights on the charge transfer dynamics at the modified semiconductor interface. The measurements were performed as follows:

1) the potential of the electrode was equilibrated in the dark, after initial positive polarization (pre-conditioning) at potentials at which no dark faradic processes occur;

2) after equilibration was attained, light was shined on the electrode and a constant photovoltage was reached and maintained for several seconds. The amplitude of the negative voltage drop upon illumination (ΔV_{photo}) was ca. 200 mV;

3) illumination was turned off and the photovoltage decayed due to electron/hole recombination.

In the unmodified hematite in borate buffer (Figure 5.11-a, blue line) it can be observed that, upon illumination, the photovoltage slowly ($\tau \approx 26$ s) drifts to the steady value, which is reached ca. 100 s after illumination is turned on. After dark conditions are restored, the photovoltage recovery shows two distinct kinetic regimes: there is a fast, almost instantaneous (for the time scale of the experiment) partial recovery, having a small amplitude (ca. 1/10 of ΔV_{photo}), followed by a very slow decay with a lifetime of hundreds of seconds. The initial dark equilibrium voltage is not restored even after several hundreds seconds. In the presence of Fe-OEC (Figure 5.11-a, red line) the steady state photovoltage is reached with an almost instantaneous drop and, upon restoration of the dark conditions, the fast component of the decay has a significantly larger amplitude (ca. 1/3 ΔV_{photo}). As a comparison, Figure 5.11-b (black line) shows the photovoltage decay of unmodified hematite in the presence of 0.1 M $[Fe(CN)_6]^{4-}$ acting as a reversible hole scavenger, where both the drop to the steady state photovoltage and the recovery to the initial dark equilibrium value are almost instantaneous.

The photovoltage decay experiments can be interpreted as follows: the unmodified hematite is dominated by the filling (slow drift to the steady photovoltage value) of long lived trap states, as indicated by the dominating, extremely slow component of the photovoltage recovery. In the presence of Fe-OEC, holes are partly transferred to the water oxidation catalyst, where, in the absence of applied bias, recombination with electrons occurs on a fast time scale. This explanation is corroborated by the transient behaviour of unmodified hematite in the presence of a Fe(II)/(III) couple acting as a fast hole scavenger. In this latter case the fast and almost complete photovoltage recovery is ostensibly determined by shuttle-mediated electron-hole recombination as summarized in Scheme 5.1.

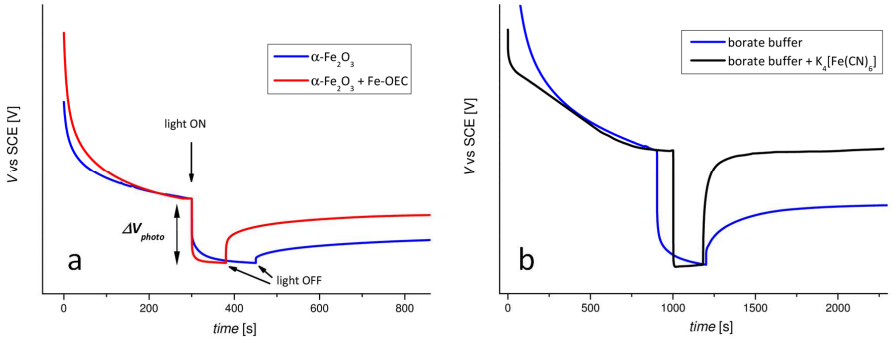

Figure 5.11. Open circuit photovoltage decays of: (a) unmodified hematite (blue line) and Fe-OEC modified hematite (same electrode after functionalization, red line in 0.5 M sodium borate buffer; (b) unmodified hematite in the absence and in the presence of 0.1 M $K_4[Fe(CN)_6]$ in sodium borate buffer. For sake of clarity, in all cases ΔV_{photo} was normalized to the same value.

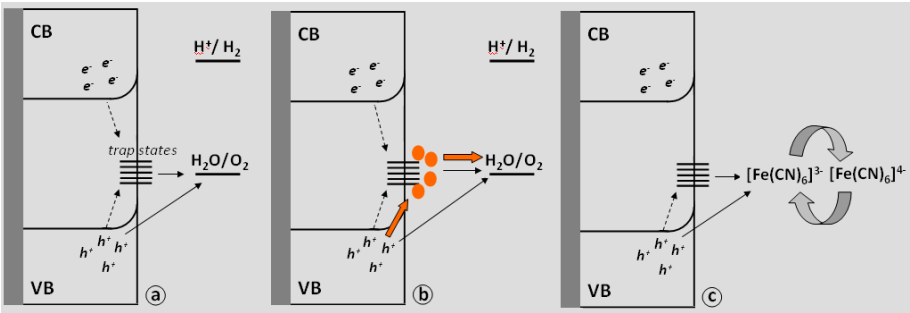

Scheme 5.1. Charge transfer and recombination pathways hypothesized on the basis of photovoltage decay experiments. In unmodified hematite (a) holes are prevailingly trapped in intraband gap states, where they slowly recombine with electrons (dark solid lines). In the Fe-OEC modified hematite (b), holes are partly scavenged by the surface bound catalyst either via trap states (dark solid lines) or by direct transfer from the valence band (grey lines) (VB). Recombination involves both holes trapped in the catalyst and in trap states. In the presence of a reversible redox shuttle (Fe(II)/(III)) (c) holes trapped in intraband states or in the VB react with Fe(II) forming Fe(III). Electrons recombine with Fe(III) resulting in a fast photovoltage decay.

5.5 Electrochemical Impedance Spectroscopy (EIS)

EIS was performed both in the dark and under illumination in order to identify and understand the active elements and interfaces in the photocurrent generation. Let alone surface modification with Fe-OEC, we note that, to the best of our knowledge, a detailed EIS study of simpler Sn(IV) doped hydrothermal hematite photoelectrodes has not been so far reported. For sake of clarity, Figure 5.12 reports the complex plane (Nyquist) plot recorded for both Fe-OEC modified and unmodified hematite photoelectrode under AM

1.5G illumination and biased at 0.3 V vs. SCE. Fitted Nyquist and Bode phase plots recorded at 50 mV intervals in the range 0 - 0.6 V vs. SCE are reported in Figures A1 and A2 (see Appendix A). Both hematite and Fe-OEC modified hematite electrodes share the same impedance features, which are described by two complex plane arcs, outlined by the arrows in Figure 5.12, at intermediate (100-10 Hz) and low frequencies (10-1 Hz) respectively. Correspondingly, two clear phase peaks are observed (Figures A1-b and A2-b). The low frequency phase peak has an angle close to 70° at low potentials, at the onset of photocurrent generation, indicating that at these potentials interfacial charging dominates over charge transfer. As the electron transfer is activated, at increasingly positive bias, the phase angle decreases with increasing potential and, concomitantly, the phase peak shifts to higher frequency. On the other hand, the intermediate frequency peak has a phase angle which increases with increasing potentials, reaching 40° - 50° while shifting to lower frequencies.

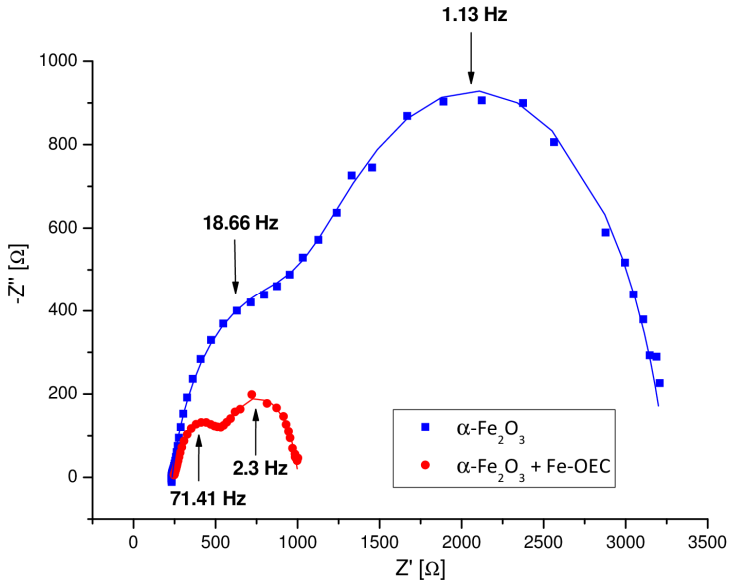

Figure 5.12. Complex plane plot (0.3 V vs. SCE) of the same hematite electrode before (blue squares) and after (red circles) functionalization with Fe-OEC under AM 1.5G illumination in 0.5 M sodium borate buffer (pH 11.5). Data are fitted (solid lines) with the circuital model reported in Scheme 5.2.

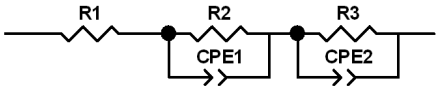

Scheme 5.2. Equivalent circuit used for fitting of EIS data.

5.5.1 Assignment of the charge transfer interfaces

The inverse of the charge transfer resistances and the total resistance ($R_{tot}^{-1} = (R_1 + R_2 + R_3)^{-1}$) extracted from the fitting of EIS data with the electric equivalent reported in Scheme 5.2 in the low frequency limit ($\omega \rightarrow 0$) are reported in Figures 5.13 and compared with the inverse of the differential resistance $\left(\frac{\partial J}{\partial V}\right)$ obtained from the *J-V* curve. It can be observed that the major resistive contribution, within the explored potential interval, arises from R_3, which contributes to the low frequency loop originated by the parallel mesh in Scheme 2 (R3-CPE2). R_3^{-1} (black triangles) exhibit the same potential dependence of the inverse of the differential resistance, indicating that the parallel mesh (R3-CPE2) models the interface which is mainly responsible of the photocurrent generation. Therefore, R_3 can be assigned to the charge transfer resistance (R_{CT}) at the hematite/electrolyte interface, whereas the resistance R_2 in the (R2-CPE1) mesh, showing a weak potential dependence (Figure 5.14) and a weak correlation with the *J-V* curve (squares in Figure 5.13), is assigned to the charge transfer resistance at the hematite/FTO interface ($R_{CT\text{-}FTO}$).

5.5.2 Mott-Schottky (MS) analysis of the active interfaces

The study of the capacitances associated with the two different charge transfer resistances allowed to corroborate the previous assignment. The capacitance related to R2 (CPE1) of either unmodified or modified hematite photoelectrodes calculated at intermediate frequencies both in the dark (1 Hz) and under illumination (in the maximum of the high frequency arc) resulted in reasonably linear MS plots

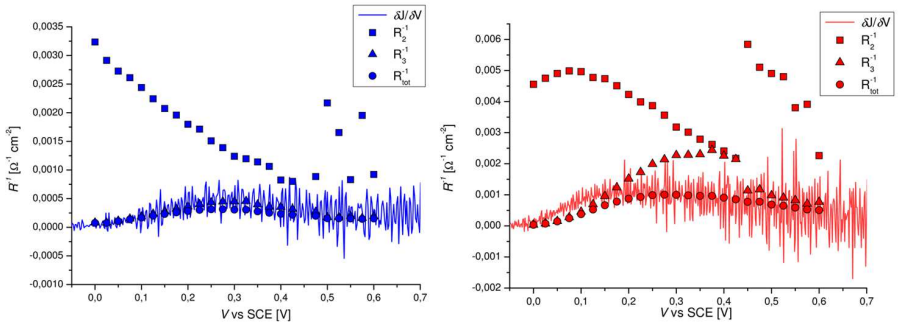

Figure 5.13. R_2^{-1} (squares), R_3^{-1} (triangles) and R_{tot}^{-1} (circles) compared to the derivative of the *J-V* curve (solid line) with the model reported in Scheme 2 for hematite before (blue) and after (red) functionalization with Fe-OEC.

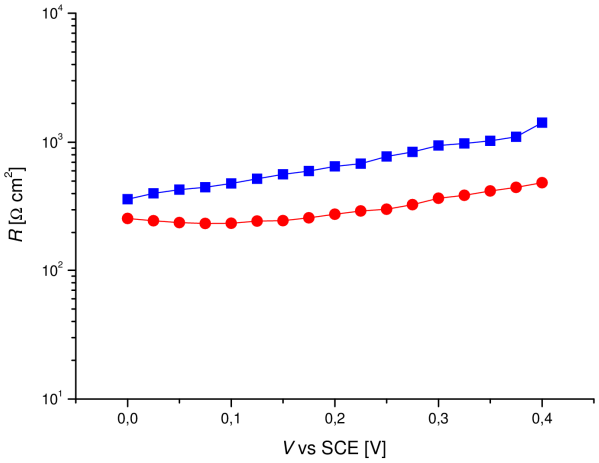

Figure 5.14. Potential dependence of R2 in hematite photoelectrodes before (blue squares) and after surface functionalization with Fe-OEC (red circles) under AM 1.5G illumination in 0.5 M sodium borate buffer (pH 11.5).

(Figure 5.15), yielding a donor density N_d, calculated according to Equation 5.1, in good agreement with the donor density (≈ 10^{20}) reported for the FTO:[11]

$$N_d[cm^{-3}] = \frac{2}{\varepsilon_0 \cdot \varepsilon_{FTO} \cdot q \cdot b} \qquad (5.1)$$

with $\varepsilon_0 = 8.854 \cdot 10^{-12}$ F/m, $\varepsilon_{FTO} = 10$,[12] $q = 1.610 \cdot 10^{-19}$ C, b= slope of the linear trait of MS plots. The active area of the electrode (1.17 cm^2) has been determined by cyclic

voltammetry (CV) analysis (Figure A3). The intercept on the potential axis at ca. -100 mV vs. SCE is also consistent with the flat band potential estimated from the threshold of the photoanodic transients in Figure 5.8-a. This is a clear indication that indeed the capacitance of the photoelectrode in the dark and under illumination in the intermediate frequency range is dominated by the space charge region developed into the FTO. This finding is corroborated also by comparative cyclic voltammetry experiments in the dark (Figure A3).

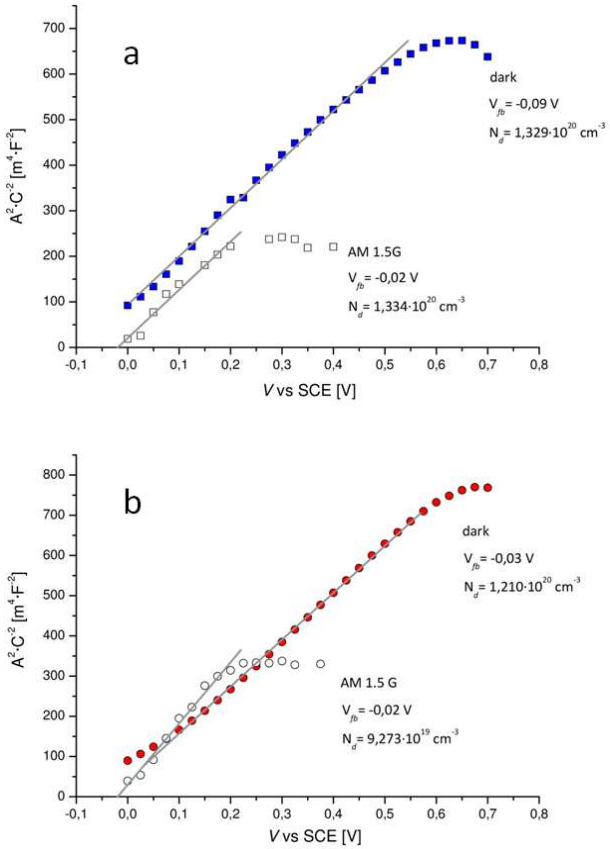

Figure 5.15. MS plots in the dark (coloured symbols) and under AM 1.5G illumination (empty symbols) of (a) unmodified hematite and (b) Fe-OEC modified hematite.

The maximum capacitance of the hematite/electrolyte interface (R3-CPE2 mesh), calculated under illumination in correspondence of the maximum of the low frequency arc resulted in a super linear MS (A^2/C^2 vs. V) behaviour. Although deviations from the

linearity were observed in fractal hematite electrodes and in ZnO nanotubes by Grätzel,[11] Windisch[13] and Bisquert[14] respectively, in our case the linear regressions of the two different linear traits (Figure 5.16) resulted in either too negative (-1.1 V vs. SCE) or too positive (0.15 V vs. SCE) potentials, in disagreement with the flat band potential estimated from Figure 5.15 and Figure 5.8. Further, it was observed that, under illumination, the capacitance of the semiconductor/electrolyte interface increased by a 10 x factor (unmodified hematite) and by a ca. 23 x factor (Fe-OEC modified hematite) (Figure 5.17). Interestingly, in the dark, both the unmodified hematite and the Fe-OEC modified hematite exhibited the same capacitance, of the order of 10^{-5} F cm^{-2}, displaying a weak dependence on the applied potential (Figure 5.16). If the capacitance at the semiconductor/electrolyte interface were dominated by the depletion region of hematite, the increase in capacitance observed under illumination would be difficult to explain since the depletion width is expected to decrease under illumination, due to the presence of photogenerated charge carriers which neutralize the charge of the ionized dopants. We also note that the clear observation of potential drop within the space charge layer was difficult to observe even in much thicker (6-7 µm) hematite electrodes, composed by large crystallites (2 µm) prepared by Peter *et al.*[15] by AACVD (Aerosol Assisted Chemical Vapour Deposition). Due to Fermi level pinning, caused by surface states, Peter concluded that most of the voltage drop relevant to the activation of the oxygen evolution reaction occurred across the Helmholtz layer.

5.5.3 Description of the capacitance of the semiconductor/electrolyte interface

In our case, the capacitance of the semiconductor/electrolyte interface under illumination, follows a broad, approximately Gaussian distribution with the potential, reaching a maximum value, in presence of FeOEC, at ca. 0.15 V vs. SCE.

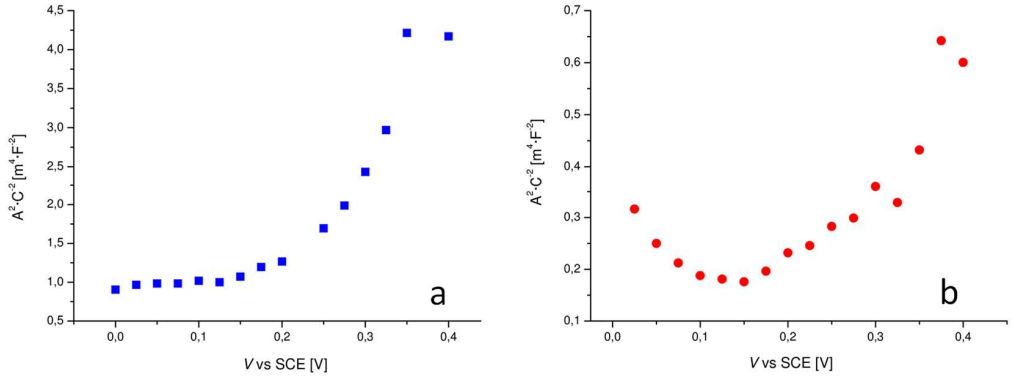

Figure 5.16. MS plots of the semiconductor/electrolyte interface under illumination of the same hematite electrode before (a) and after (b) surface functionalization with Fe-OEC measured in 0.5 M sodium borate buffer (pH 11.5).

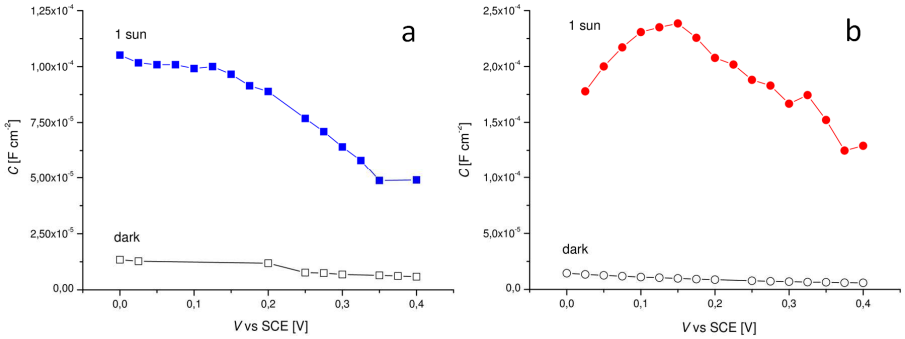

Figure 5.17. Capacitance of the semiconductor/electrolyte interface in the dark (empty symbols) and under AM 1.5 G illumination (coloured symbols) of an hematite electrode (a) before and (b) after surface modification with Fe-OEC measured in 0.5 M sodium borate buffer (pH 11.5).

The same trend is observed with unmodified hematite, although the maximum, at about the same voltage, is less evident (Figure 5.18). Hamann and Bisquert[16,17] have described a similar capacitance behaviour in hematite thin films prepared by ALD and explained it with the trapping of photoinduced holes in highly valent surface states.

The capacitance of the surface states (C_{SS}) can then be expressed as a chemical capacitance[18] according to

$$C_{ss} = e^2 \frac{\partial n_{ss}}{\partial \mu} \qquad (5.2)$$

where μ is the chemical potential of the electron, e is the electronic charge and n_{SS} is the occupied surface state density. n_{SS} is related to N_{ss}, the surface state density and to the chemical potential by the Fermi-Dirac distribution according to

$$n_{ss} = N_{ss} \frac{1}{exp\left(\frac{E_{ss} - \mu}{kT}\right) + 1} \tag{5.3}$$

And by substituting Equation (5.3) in (5.2) and differentiating one obtains

$$n_{ss} = \frac{e^2 N_{ss}}{kT} \frac{exp\left(\frac{E_{ss} - \mu}{kT}\right)}{\left[exp\left(\frac{E_{ss} - \mu}{kT}\right) + 1\right]^2} \tag{5.4}$$

which is a function which peaks when $E_{SS}=\mu$.

The considerable increase in the capacitance of the surface trap states (a factor of ca. 2.5), observed in the presence of the Fe-OEC, indicates a favourable transfer of holes to the catalyst. We note that the detailed chemical nature of the surface trapped holes has not yet been clarified, however it has been proposed[17] that trapping of holes may lead to reactive high valent intermediates according to the primary event

$$Fe(III)\text{-}OH + h^+ \rightarrow Fe(IV) = O + H^+ \tag{5.5}$$

The Fe(IV)=O centres may undergo subsequent nucleophilic attack by the water molecule, leading to peroxide intermediates which then decompose to oxygen, through a sequence of steps of variable complexity, which, for example, have been characterized in the case of other metal based catalysts like Ru(II) aquo-complexes[19,20] and Co(III) amorphous oxides.[21] The Fe(III)-OEC, being an amorphous hydrated oxide, easily undergoes the proton coupled electron transfer (PCET) leading to the reactive intermediate of Reaction 5.5. It may not be just a coincidence that to a doubling of photocurrent it corresponds a doubled interfacial capacitance, since the transfer of holes to reactive states exposed to

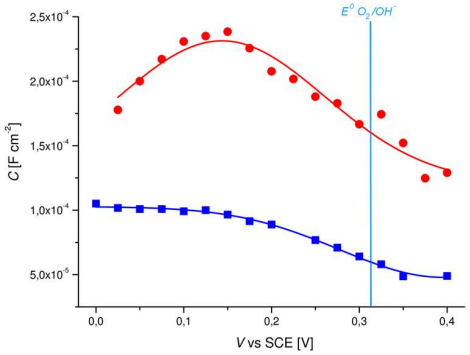

Figure 5.18. Capacitance of the semiconductor/electrolyte interface under AM 1.5 G illumination of the same hematite electrode before (blue squares) and after (red circles) surface modification with Fe-OEC measured in 0.5 M sodium borate buffer (pH 11.5). The blue bar indicates the thermodynamic potential of water oxidation at pH 11.5.

the electrolyte, where scavenging occurs, is instrumental in overcoming the kinetic competition with the recombination reaction.

The EIS measurements thus corroborate the first evidences gained with the photovoltage transients, which suggested an efficient transfer of holes to electronic states of the catalyst at the surface of the semiconductor. This mechanism seems to be different than that observed by some authors with Co-Pi functionalized hematite.[22] In this latter case, time resolved studies suggested that the presence of a thin layer of Co-Pi catalyst prevailingly resulted in the formation of a heterointerface, where the development of a wider and deeper space charge layer assisted the interfacial charge separation.

5.6 Transient Spectroscopy

Nanosecond laser spectroscopy measurements were performed in order to gain a direct spectroscopic evidence of the trapping of photogenerated holes in the surface bound Fe(III) catalyst. A wide interval of photogenerated electron-hole lifetime has been reported for hematite, varying from ps to ms-s depending on the method of investigation and on the experimental conditions.[23]

Usually, evidence of ultrafast recombination in hematite thin films[24,25] is gained by pump-probe techniques under strong excitation power, and are attributed to fast non

geminate recombination due to the large transient concentration of photoinduced electrons and holes. Under lower pulse energy (mJ), like those conventionally used in laser flash photolysis techniques, the recombination occurs on a longer time scale, typically from hundreds nanoseconds to microseconds. Even at such longer timescale, it is unlikely to observe the hole transfer to the electrolyte, which should occur on a much longer timescale, as pointed out by Durrant[23] and Peter[15] who independently observed hole transfer rate constants of the order of 1 s^{-1}. This value also agrees with the frequency of the phase peaks assigned to the interfacial electron transfer observed in this work (1.2 s^{-1} for unmodified hematite and 2.3 s^{-1} for Fe-OEC hematite, Figures A.1-b and A.2-b).

Nevertheless, a direct information about the recombination and trapping kinetics can be useful for clarifying the operation of the Fe-OEC modified electrodes and to corroborate the results gained by the photoelectrochemical techniques. Further, it allows to characterize the recombination events which are instantaneous for time scale of the photovoltage decay experiments in Figure 5.11.

The normalized decay kinetics observed at 580 nm, under 0.7 V vs. SCE are reported in Figure 5.19 and the transient difference spectra upon 355 nm excitation (20 mJ/cm^2/pulse), represented at increasingly delays after the laser pulse, are reported in Figure 5.20.The transient spectra are dominated by a sharp band at 570-580 nm which is a typical feature of hematite, followed by a broad absorption, whose intensity slowly decreases by moving to the red region of the spectrum. These optical transitions are originated by excitations of electrons from the valence band to empty intra-band-gap states, generated by reaction with photogenerated holes, and therefore represent the characteristic spectroscopic signature of hole trapping.[25] In the blue region, between 450 and 500 nm, the transient absorption has been assigned, by some authors,[27] to photogenerated electrons trapped in proximity of the surface. In the presence of the catalyst we observe essentially the same features as in unmodified hematite, but the main band is slightly blue shifted and both the transient absorption at lower wavelengths and at longer wavelengths are increased in intensity compared to the main 570-580 nm

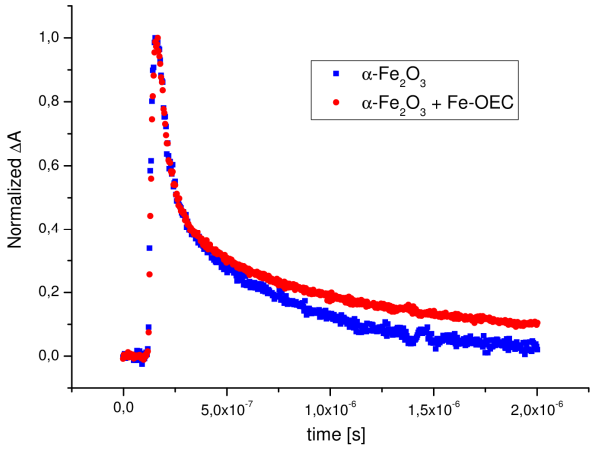

Figure 5.19. Normalized differential absorption decay in hematite photoanodes biased at 0.7 V vs. SCE: (blue) unmodified and (red) Fe-OEC modified electrode.

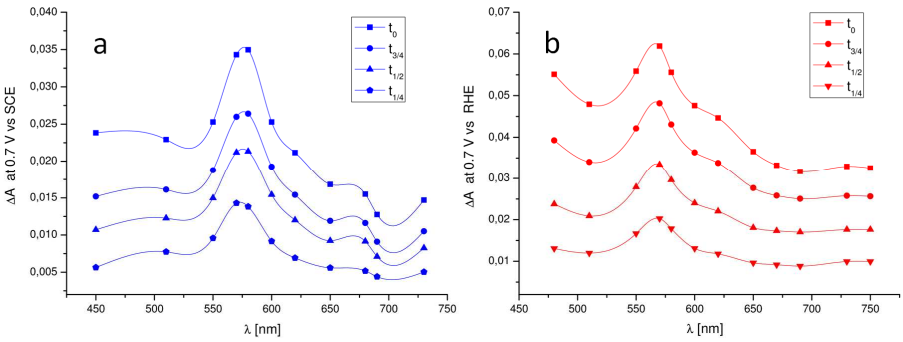

Figure 5.20. Transient difference absorption spectra of hematite photoanodes biased at 0.7 V vs. SCE: (a) unmodified and (b) Fe-OEC modified hematite electrodes. Delays were taken at t_0 (maximum ΔA amplitude) and at ¾ ($t_{3/4}$), ½ ($t_{1/2}$) and ¼ ($t_{1/4}$) of t_0.

band (Figure 5.20 and Figure A5). This blue shift is probably due to the contribution of catalyst-trapped holes, which were observed to follow an energy distribution centred at ca. 150 mV vs. SCE, slightly more negative than that of the unmodified film, where no clear capacitance peak at such potential was observed (Figure 5.18).

The transient absorption recovery due to charge recombination (Figure 5.19 and Figure 5.21) is almost complete in a time scale of 2 µs, and exhibits a multiexponential behaviour, which was satisfactorily fitted with a bi-exponential function. It is evident the presence of a fast component, which has essentially the same lifetime (60 ± 10 ns) both in the unmodified and in the Fe-OEC modified hematite, having also a weak dependence on

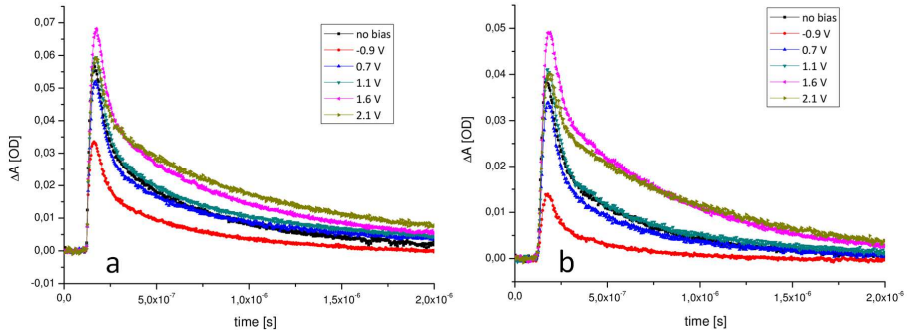

Figure 5.21. Transient difference absorption spectra of hematite photoanode modified with Fe-OEC recorded at (a) 580 nm and (b) 650 nm in the presence of an increasingly strong positive bias applied vs. SCE in a two electrode configuration in 0.5 M sodium borate buffer (pH 11.5).

the applied bias, at least in the explored potential interval (-0.9 – 2.1 V vs. SCE). By contrast, the long component of the decay, having a lifetime of about one order of magnitude longer (600-700 ns) exhibits a strong dependence on the applied bias, and has a longer lifetime (ca. 50%) in the presence of the catalyst (Figure 5.19 and Figure A6), probably due to the increased spatial charge separation between holes, trapped on the surface bound catalyst, and electrons, which are drawn to the back contact under the positive bias. Indeed, upon application of an increasingly positive bias (Figure 5.21), up to 1.6 V vs. SCE (the amplitudes at 1.6 and 2.1 V vs. SCE are almost superimposable) to the Fe-OEC modified hematite, the transient absorptions at 580 and 650 nm clearly gain intensity and the amplitude of the longer lived component of the decay increases by a factor of 2, consistently with a more favourable potential driven charge separation due to hole transfer and trapping into reactive sites of the surface bound catalyst.

5.7 Conclusions

Nanostructured hydrothermal hematite photoanodes were functionalized with an amorphous Fe(III) oxide charge transfer catalyst obtained by SILAR. The modified photoelectrodes exhibited a considerable improvement in their photoanodic response, consisting in a doubled photoanodic current, in all the electrolytes explored in this work

(0.5 M sodium borate buffer (pH 11.5), 0.5 M sodium carbonate (pH 11.5) and 0.1 M NaOH (pH 13.1)).

EIS under illumination indicated the presence of two electroactive interfaces, respectively at the FTO/hematite and at the hematite/electrolyte junction. While the FTO/hematite interface was characterized by the formation of a depletion layer developing into the FTO, unambiguous evidence of space charge formation within the nanostructured hematite, either modified or unmodified, was not found. Rather, the interfacial behavior is dominated by hole trapping in surface states, which are believed to be the intermediates responsible for the OER. The considerable increase in the capacitance of the surface trap states (a ca. 2.5 x factor), observed in the presence of the Fe-OEC, indicates a favorable transfer of holes to the catalyst, which being an amorphous hydrated oxide, easily undergoes the proton coupled electron transfer, allowing to store oxidizing equivalents in reactive states exposed to the electrolyte.

Laser flash photolysis, performed in the ns-μs time domain, where charge trapping and recombination events are dominating, is consistent with such interpretation, showing a long decay component having a longer lifetime in the presence of the catalyst. Under positive potential the amplitude of the long component is increased by a 2-3 x factor, due to the more favourable potential driven spatial charge separation between holes, trapped into reactive sites of the surface bound catalyst, and electrons, which are drawn to the back contact.

Finally, we would like to emphasize that, despite the presence of the hole transfer catalyst, the majority of charge carriers are unable to escape from recombination, indicating that the potentialities of hematite as a photoanodic material are still far from being fully exploited.

5.8 References

24 R. D. L. Smith, M. S. Prévot, R. D. Fagan, Z. Zhang, P. A. Sedach, M. K. J. Siu, S. Trudel and C. P. Berlinguette, *Science,* **2013**, *340*, 60.

25 J. A. Seabold and K.-S. Choi, *J. Am. Chem. Soc.,* **2012**, *134*, 2186.

26 A. Mariana Balu, A. Pineda, K. Yoshida, J. Manuel Campelo, P. L. Gai, R. Luque and A. Angel Romero, *Chem. Comm.,* **2010**, *46*, 7825.

27 M. Hermanek, R. Zboril, I. Medrik, J. Pechousek and C. Gregor, *J. Am. Chem. Soc.,* **2007**, *129*, 10929.

28 V. Cristino, S. Berardi, S. Caramori, R. Argazzi, S. Carli, L. Meda, A. Tacca and C. A. Bignozzi, *Phys. Chem. Chem. Phys.,* **2013**, *15*, 13083.

29 Q. Yu, X. Meng, T. Wang, P. Li and J. Ye, *Adv. Funct. Mater.,* **2015**, *25*, 2686.

30 L. Vayssieres, N. Beermann, A. Hagfeldt and S. E. Lindquist, *Chem.Mater.,* **2001**, *13*, 233.

31 H. Kim, M. Seol, J. Lee and K. Yong, *J. Phys. Chem. C,* **2011**, *115*, 25429.

32 J. H. Kennedy and K. W. Frese, *J. Electrochem. Soc.,* **1978**, *125*, 709-714.

33 K. Sivula, R. Zboril, F. Le Formal, R. Robert, A. Weidenkaff, J. Tucek, J. Frydrych and M. Grätzel, *J. Am. Chem. Soc.,* **2010**, *132*, 7436.

34 I. Cesar, K. Sivula, A. Kay, R. Zboril and M. Grätzel, *J. Phys. Chem. C.,* **2009**, *113*, 772.

35 G. Boschloo and D. Fitzmaurice, *J. Phys. Chem. B.,* **1999**, *103*, 3093.

36 C. F. Windisch and G. J. Exarhos, *J. Vac. Sci. Technol. A,* **2000**, *18*, 1677.

37 R. Tena-Zaera, J. Elias, C. Levy-Clement, C. Bekeny, T. Voss, I. Mora-Sero and J. Bisquert, *J. Phys. Chem. C.,* **2008**, *112*, 16318.

38 K. G. U. Wijayantha, S. Saremi-Yaramada and L. M. Peter, *Phys. Chem. Chem. Phys.,* **2011**, *13*, 5264.

39 B. Klahr, S. Gimenez, F. Fabregat-Santiago, T. W. Hamann and J. Bisquert, *J. Am. Chem. Soc.* **2012**, *134*, 4294.

40 B. Klahr, S. Gimenez, F. Fabregat-Santiago, J. Bisquert and T. W. Hamann, *Energy Environ. Sci.,* **2012**, *5*, 7626.

41 J. Bisquert, *Phys. Chem. Chem. Phys.,* **2003**, *5*, 5360.

42 J. H. Alstrum-Acevedo, M. K. Brennaman and T. J. Meyer, *Inorg. Chem.,* **2005**, *44*, 6802.

43 J. J. Concepcion, J. W. Jurss, M. K. Brennaman, P. G. Hoertz, A. O. T. Patrocinio, N. Y. Murakami Iha, J. L. Templeton and T. J. Meyer, *Accounts of Chemical Research,* **2009**, *42*, 1954.

44 D. G. Nocera, *Accounts of Chemical Research,* **2012**, *45*, 767.

45 M. Barroso, A. J. Cowan, S. R. Pendlebury, M. Grätzel, D. R. Klug and J. R. Durrant, *J. Am. Chem. Soc.,* **2011**, *133*, 14868.

46 M. Barroso, S. R. Pendlebury, A. J. Cowan and J. R. Durrant, *Chem. Sci.,* **2013**, *4*, 2724.

47 Y. Ling, W. Gongming, D. A. Wheeler, J. Z. Zhang and Y. Li, *Nano Lett.,* **2011**, *11*, 2119.

48 A. G. Joly, G. R. Williams, S. A. Chambers, G. Xiong, W. P. Hess and D. M. Laman, *J. Appl. Phys.,* **2006**, *99,* 053521.

49 S. R. Pendlebury, M. Barroso, A. J. Cowan, K. Sivula, J. W. Tang, M. Grätzel, D. R. Klug and J. R. Durrant, *Chem. Comm.,* **2011**, *47*, 716.

50 Z. Huang, Y. Lyn, X. Xiang, W. Rodirguez- Cordoba, K. J. McDonald, K. S. Hagen, K.-S. Choi, B. S. Brunschwig, G. D. Musaev, C. L. Hill, D. Wang and T. Lian, *Energy Environ. Sci.,* **2012**, *5*, 8923.

CHAPTER 6

EFFECT OF THIN IRON OXIDE UNDERLAYER ON POROUS HEMATITE PHOTOANODES

this chapter is based on: N. Dalle Carbonare, S. Carli, R. Argazzi, M. Orlandi, N. Bazzanella, A. Miotello, S. Caramori and C. A. Bignozzi *PCCP*, **2015**, *17*, 29661.

6.1 Introduction

In the previous chapter, we have focused our attention on the semiconductor/electrolyte interface of the hematite photoanode, enhancing its performance by the deposition of an iron-based OEC acting in the reduction of electron/hole recombination at the surface by actively operating in the hole transfer process. However, the analysis of the capacitance has also highlighted the importance of the semiconductor/FTO interface in the charge collection process. Although this interface does not actively participate in the charge generation process, recombination can take place with important limitation to the overall performance of the device.

Recently, a new strategy to promote photoconversion efficiency of hematite electrodes has been developed, involving thin films of hematite deposited over ultrathin layers of different oxides that, having a conduction band significantly higher than that of hematite, act as tunneling junction. Usually such underlayers are used in combination with very thin

hematite films (10-30 nm), that do not guarantee high Light Harvesting Efficiency (LHE), but are desirable due to the reduction of the photogenerated holes path to reach the SCLJ from the bulk. This allows holes to be transferred to the solution with minimized recombination losses, finding a compromise between deep light penetration depth and very short hole diffusion length (see Chapter 3.4.1). Improvement of the water oxidation activity has been observed adopting different ultrathin oxide underlayers. Steier *et al.*[1] observed that doping hematite with Si and Nb diffusing from underlayers of SiO_x and Nb_2O_5, improves the photoanodic performance of 10-15 nm ultrasonic spray pyrolysed hematite films. SiO_x[2] and Ga_2O_3[3] are also responsible for a beneficial increase in hematite crystallinity due to the reduction of the unfavorable mismatch between the FTO and hematite lattices. Similar results have been obtained by Zhang *et al.*[4] with TiO_2 and by Zandi *et al.*[5] with Ga_2O_3 and Nb_2O_5 underlayers, who demonstrated how the ca. 3 times higher crystallinity of 18 nm atomic layer deposited hematite film results in stronger light absorption closely related to photocatalytic water oxidation performance. In spite of the still debated exact physical effect of the oxide underlayer, it is reasonable to assume that the electronic effect should also be related to a reduction in electron/hole recombination at the FTO/hematite interface due to the insulating nature of the underlayer. In 2008, Liang *et al.*[6] have reported a beneficial effect for both the reproducibility and the photocurrent efficiency of 200 nm spray pyrolysed and silicon-doped hematite using a 5 nm spray pyrolysed SnO_2 underlayer.

Following this latter approach, we have explored the coupling of a non-insulating thin underlayer of spin-coated α-Fe_2O_3 (HTL) with an electrophoretically deposited mesoporous α-Fe_2O_3 film (MPH), realizing distinct layers cooperating to improve the charge separation in photoelectrodes entirely realized with iron based materials. The presence of a 30 nm thin underlayer results in a fourfold enhancement of the photocurrent generated by the hematite electrode under a positive potential bias, and further improves with an iron(III)-OEC. DC electrochemical techniques and EIS analysis have been employed to gain a mechanistic understanding of the improved charge separation in the combined HTL-MPH electrodes, showing that the development of a depletion region across the photoactive films, made possible by the HTL, is responsible

for the increased electron collection efficiency. Furthermore, at the SCLJ the iron(III) catalyst is able to trap holes in reactive sites exposed to the electrolyte favouring their transfer to the solution. It is thus demonstrated that the cooperation of different layers of the same type of oxide (thin crystalline, porous crystalline and amorphous iron oxide) allows to tune the performance of the electrode, allowing to extract a significant amount of charge from a 300 nm thick solution processed mesoporous film with excellent light harvesting capabilities, thus realizing an efficient all-iron based photoelectrode obtained with scalable wet solution procedures and without addition of external dopants.

6.2 Preparation and modification of hematite photoanodes

6.2.1 α-Fe_2O_3 thin underlayer (HTL) deposition

$FeCl_3 \cdot 6H_2O$ (0.54 g) was dissolved in DI water (20 mL) and then Polyethyleneglycol Bisphenol A Epichlorohydrin Copolymer (0.54 g) was added under gentle stirring to avoid the formation of bubbles. The solution was spin coated onto FTO glass (1000 rpm for 9 seconds and 2000 rpm for 30 seconds). After every spin coating cycle the glass slide was annealed at 550 °C for 15 minutes in air. Spin coating cycles were repeated for 1, 2, 3 and 4 times leading to the HTL-1-4 type electrodes (Figure 6.1).

6.2.2 Mesoporous α-Fe_2O_3 film (MPH) deposition

Mesoporous α-Fe_2O_3 was electrophoretically deposited on either FTO glass or on HTL samples following a literature procedure.[7] Briefly, in a Teflon beaker $FeCl_3 \cdot 6H_2O$ (0.55 g) was dissolved in a mixed solution of ethanol (20 mL) and water (5 mL) and then sodium acetate (0.8 g) was added. The beaker containing the dark brown solution was capped with Teflon tape and put in a steel autoclave at 180 °C for 12 hours. The autoclave was cooled down at room temperature and the resulting red powder was

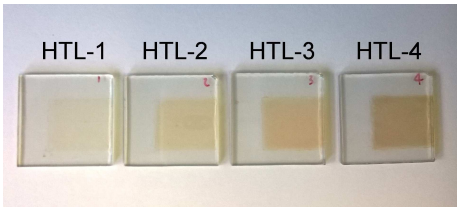

Figure 6.1. Top-view images of HTL-1-4 samples.

first washed several times with water and acetone and then suspended in acetone (50 mL). To a sample of this colloidal solution (5 mL), iodine (20 mg) and acetone (45 mL) were added, mixed in an ultrasonic bath for ten minutes and used for the electrophoretic deposition of iron oxide nanoparticles. FTO slides and HTL samples were immersed in the colloidal solution and polarized at 10 V in two electrode configuration (a bare FTO glass was used as counter electrode at a distance of ca. 0.8 cm) for 35 seconds. The nanoparticles were deposited at the negative electrode, resulting in a homogeneous red coating. The electrodes were washed with acetone and then annealed first at 550 °C for 1 hours and then at 800 °C for 20 minutes in air. The addition of iodine to the acetone solution of iron oxide nanoparticles led to the in-situ generation of protons according to Scheme 6.1. The neutral iron oxide nanoparticles can be thus protonated, probably on hydroxyl groups present on their surface, and they become positively charged, experiencing the effect of the electric field during the electrophoretic deposition process.

6.2.3 Fe(III) Oxygen Evolving Catalyst (OEC) deposition

HTL-3-MPH electrodes were functionalized with iron(III) hydrous oxide (Fe-OEC) by using a ten cycle SILAR procedure. Each cycle consisted in the dipping of the electrode in a $FeCl_3 \cdot 6H_2O$ aqueous solution (50 mM) and then in NaOH (0.1 M). After each cycle the electrode was rinsed with abundant distilled water and, upon completion of the 10 cycles, annealed at 200 °C for 20 minutes in air.

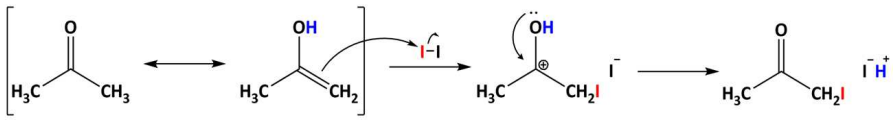

Scheme 6.1. Iodination of acetone

6.3 Morphology of pristine and modified hematite samples

The HTL was prepared with an aqueous $FeCl_3$ precursor modified with a polyethylenglycol (PEG) polymer by spin-coating over FTO glasses followed by annealing at 550 °C. Sol-gel based procedures employing spin coating technique have been successfully applied in the years to prepare thick un-doped and doped hematite photoanodes characterized by reasonable photocatalytic performances.[8-10] In our cases we limited the spin coating process to the formation of a thin layer (few nm) which would serve as a host for the subsequent nanoparticles deposition aimed at the formation of a thicker film tasked with the quantitative absorption of suitable energy photons. SEM cross sectional views of HTL-3 (Figure 6.2 a-b) show a quite-uniform conformal coverage of the larger FTO crystallites by nanometric grains of iron oxide of the size of ca. 10-12 nm (Figure 6.1-b), filling up the gaps between the FTO plates. HTL substrates, although characterized by discernible features due to the aggregation of single substructures of estimated size < 5 nm, retain a quite compact morphology corroborated by a lower roughness factor (15) with respect to the mesoporous α-Fe_2O_3 (MPH) samples (25). The repetition of subsequent spin coating cycles increases the FTO coverage by the α-Fe_2O_3 layer, as can be appreciated from SEM imaging (Figure 6.2 c-d).

The deposition of the mesoporous α-Fe_2O_3 film (MPH) was carried out according to an electrophoretic procedure,[7] which was selected as a fast, scalable and cost effective method for obtaining porous hematite electrodes, by applying 10 V to either FTO or HTL samples immersed in a colloidal suspension of hydrothermally grown Fe_2O_3 nanoparticles. The subsequent annealing at 550 °C yields a crystalline hematite film. After MPH deposition, the HTL-3, with an estimated thickness of 32 ± 6 nm (Table B1 in Appendix B),

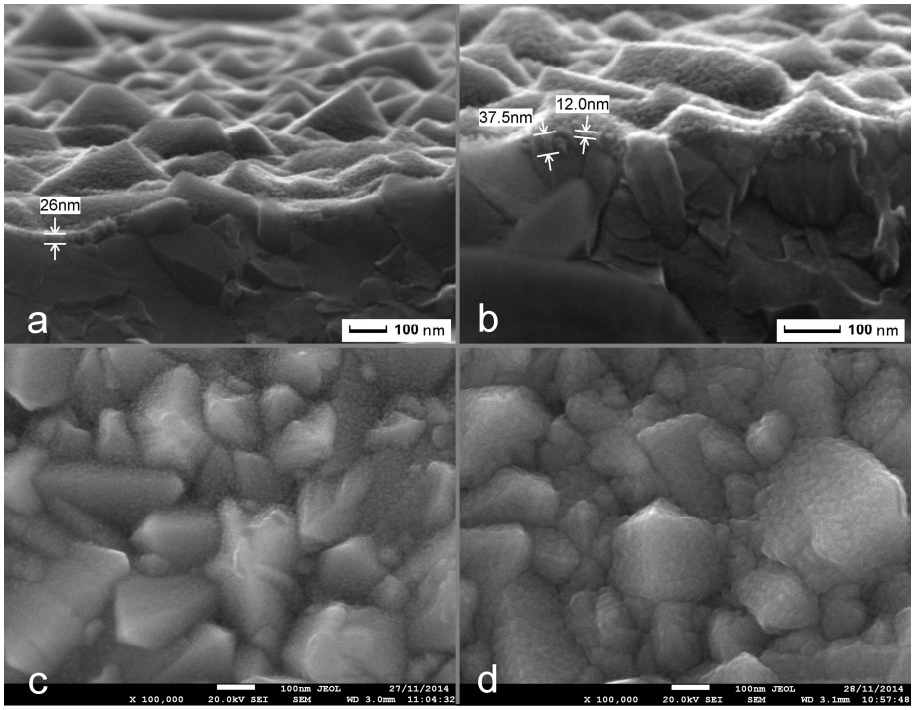

Figure 6.2 Cross sectional SEM images of (a, b) HTL-3 sample and top-view SEM images of (c) HTL-1 and (d) HTL-4 samples.

is still distinctly visible under the mesoporous α-Fe_2O_3 prolate particles (Figure 6.3-a) forming a film with a thickness varying in the range of 300-400 nm (Figure 6.3-b). After 800 °C activation of the electrodes the morphology of the MPH film changes, showing the growth and increased necking of partially fused spheroidal nanoparticles whose diameter ranges between 60 and 100 nm (Figure 6.3 c-d). The presence of the underlying HTL does not seem to have large repercussions on the necking of the mesoporous nanoparticles upon 800 °C annealing compared to MPH alone directly deposited on FTO (Figure 6.4).

The cross sectional energy dispersive analysis (Figure B1 in Appendix B), carried out to monitor possible changes in the elementary composition of the photoactive film, reveal, within the sensitivity of the technique, a similar tin concentration profile in the hematite layer before and after the 800 °C activation step, suggesting that the major impact of high temperature activation is related to the improvement of the electrical contacts across the mesoporous film. Estimation of the doping density (*vide infra*) carried out by MS analysis corroborates this indication showing a relatively low doping level of hematite.

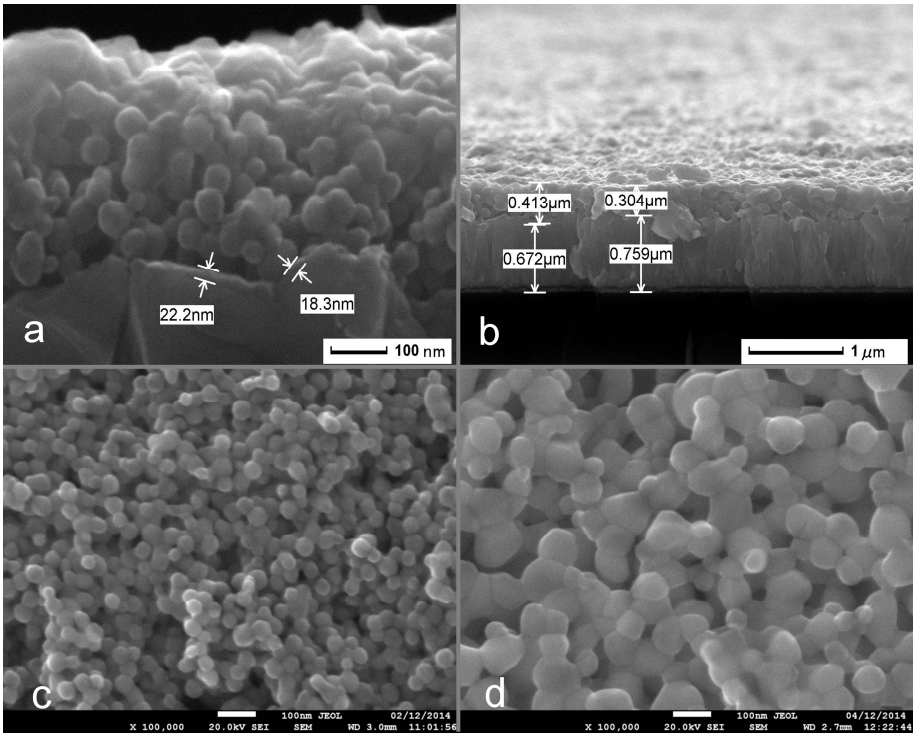

Figure 6.3. Cross sectional SEM images of MPH electrophoretically deposited over HTL-3 and annealed at (a) 550 °C and (b) 800 °C. After activation at 800 °C for 20 minutes it is more difficult to distinguish the discontinuity between HTL-3 and MPH layers. Top-view SEM images of MPH deposited over HTL-3 and annealed at (c) 550 and (d) 800 °C.

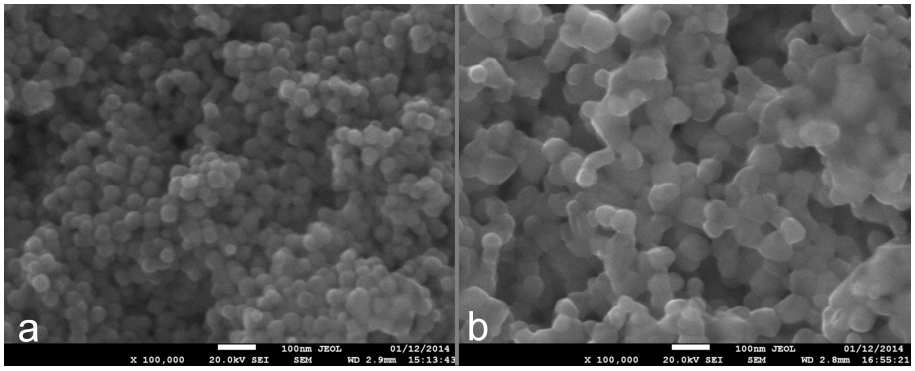

Figure 6.4. Top-view SEM images of MPH deposited over FTO and annealed at (a) 550 °C and (b) 800 °C.

The α-Fe_2O_3 crystalline phase of MPH cast over bare FTO or HTL is clearly identified by Micro-Raman analysis showing the characteristic hematite modes at 229, 295, 414 cm^{-1},[11] displaying similar relative ratio regardless of the underlying substrate (Figure 6.5). A similar Raman signature is present in the HTL layers (Figure 6.6), even though for the

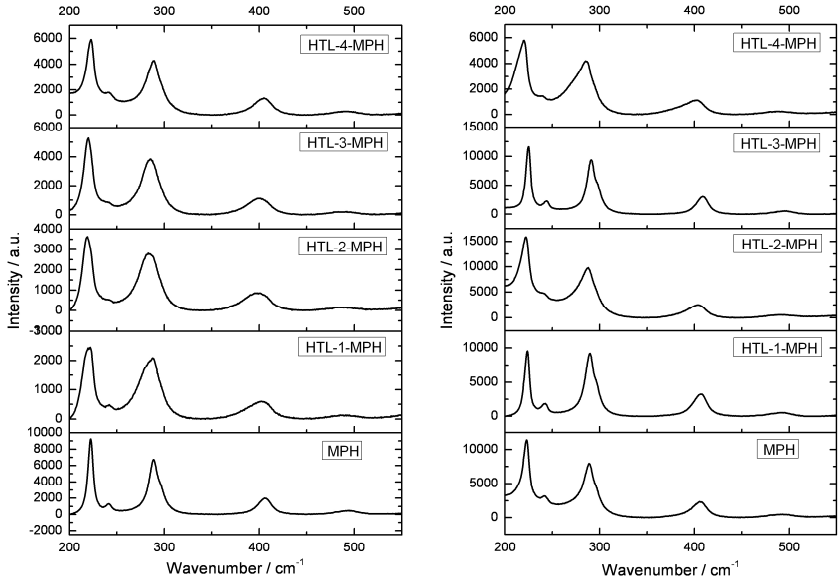

Figure 6.5. Micro-Raman spectra of MPH deposited on FTO (MPH) and on HTL-1-4 before (left) and after (right) annealing at 800°C. Besides characteristic hematite modes (229, 295, 414 cm^{-1}), minor peaks are present at: 249, 500, 615, 660 and 1320 (second order) cm^{-1}. For this reason, all spectra are reported in the range 200-500 cm^{-1}.

HTL-1 sample a complete deconvolution of the hematite response from the FTO background is not possible, due to the very low thickness of the hematite film and incomplete coverage of the FTO. Differently from the effect reported with Nb_2O_5 underlayer, resulting in improved crystallinity correlated to enhanced photocatalytic properties of ALD deposited hematite,[5] we did not observe a substantial improvement of the crystallinity of the MPH film in the presence of HTL, based on the comparative width and intensity of the Raman signals (Figure 6.5), which instead reveal after 550 °C annealing a broader shape of hematite main peaks. The crystallinity of the surface is however recovered and brought at comparable levels after the 800 °C treatment. XRD analysis, more sensitive than Raman to the bulk properties of the material, carried out on the MPH and HTL-MPH films (Figure 6.7), confirmed the similar crystalline nature of the two samples.

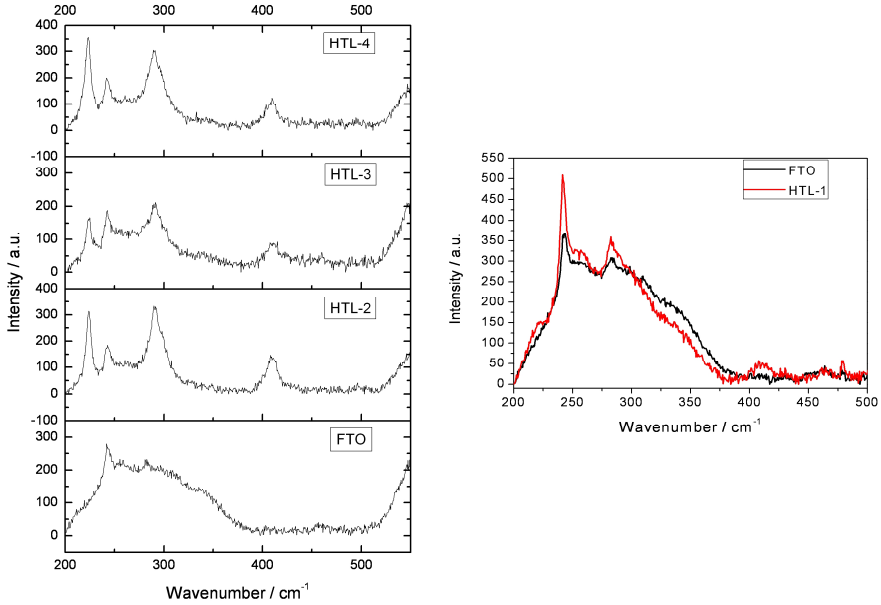

Figure 6.6. (left) Micro-Raman spectra of HTL-2-4 samples and bare FTO (shown for reference). (right) Micro-Raman spectra of HTL-1 (red line) and bare FTO (black line). Spectra for HTL-1-4 show a convolution of the hematite signal with the underlying FTO signal n particular for HTL-1 (right), where a clear identification of hematite on the surface is not possible.

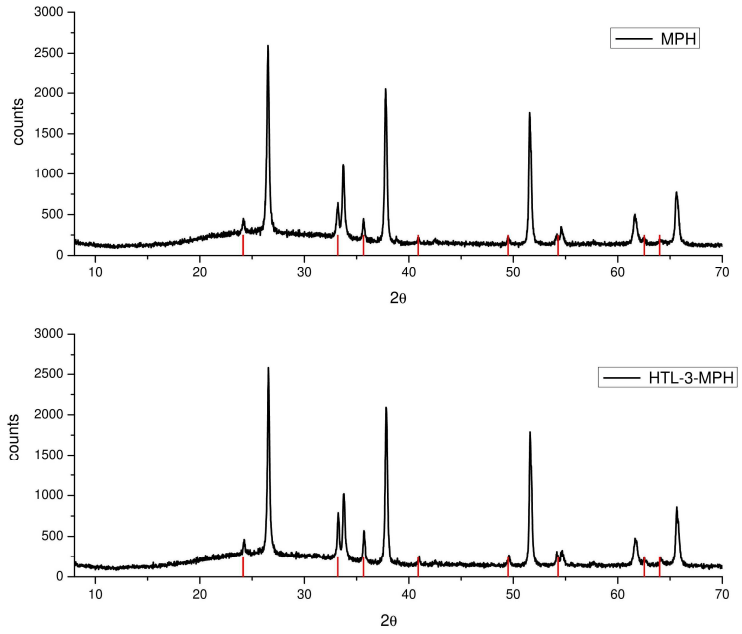

Figure 6.7. XRD of MPH and HTL-3-MPH samples after 800 °C annealing. Red bars in the diffractograms indicate α-Fe_2O_3 signals.

6.4 Optical properties of pristine and hematite samples

The absorption spectra further confirm the hematite nature of the HTL and MPH films, showing the two characteristic bands at 535-540 and 385 nm[12] (Fig. 6.8 a-b). In the case of MPH electrode, the absorption saturates at λ < 420 nm, reaching optical densities > 2.5 and allowing a quantitative absorption of photons with λ < 550 nm. The optical absorption depths (α^{-1} in nm) extracted from the absorption spectra using Equation 6.1**,** where *A* is the background subtracted absorbance at 550 nm and *x* is the film thickness (nm), estimated by cross sectional SEM images, yield coherent values of 111 and 117 nm^{-1} for HTL-3 and HTL-3-MPH in good agreement with reported values for hematite.[13]

$$A = \alpha \cdot x \cdot 2.3 \tag{6.1}$$

The absorption of the HTL, ranging from 0.13 (HTL-1) to 0.4 (HTL-4) increases in an almost linear fashion with the first three spin coating runs, starting to reach a plateau at the fourth spin coating cycle, probably corresponding to a complete coverage of the FTO substrate. The absorbance of the combined HTL-MPH electrode is superior to the additive contribution of MPH and HTL, reflecting a more favourable interaction of the hematite nanoparticles with the HTL layer, leading to a denser and closely packed porous film whose thickness is, however, comparable to that of MPH on bare FTO (Figure 6.9).

6.5 Effect of HTL on the photoelectrochemical performance

The presence of HTL improves the photoanodic activity of the hematite electrodes, with the best performance observed with MPH deposited over HTL-3 sample (Figure 6.10-a). The photoanodic current at 0.65 V vs. SCE reaches 0.95 mA cm^{-2} under 1 sun illumination in 0.1 M NaOH, producing a 4-fold enhancement with respect to MPH deposited directly on FTO, limited to just 0.23 mA cm^{-2} at the same potential. In the presence of the Fe(III)-OEC,[14,15] which does not alter the absorption profile of the

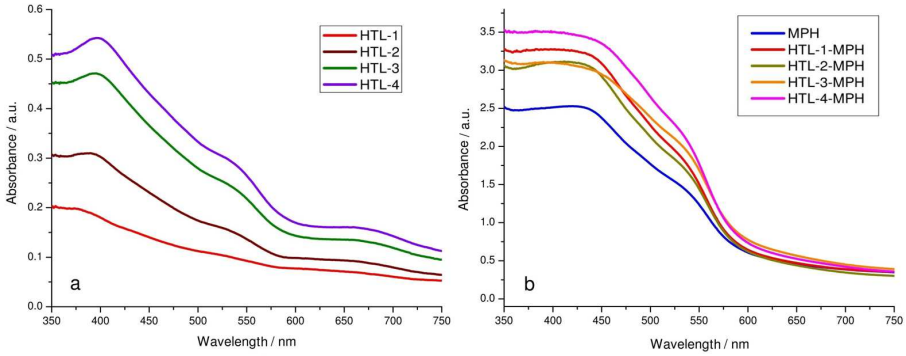

Figure 6.8. Absorption spectra of (a) HTL-1-4 spin coated on FTO and (b) MPH deposited on FTO (blue line) and on HTL-1-4 samples.

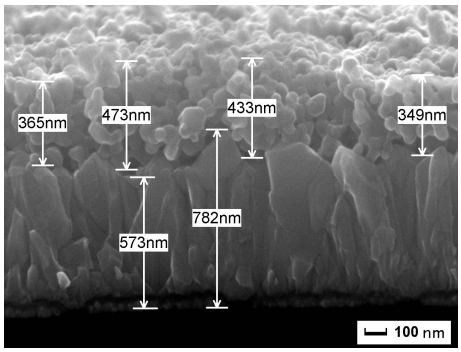

Figure 6.9. Cross sectional view of MPH deposited on bare FTO and annealed at 800 °C.

electrode, a further enhancement of the photocurrent response is observed, reaching 1.5 mA cm^{-2} at 0.65 V vs. SCE (Figure 6.10-b). There is not, however, a discernible cathodic shift of the photoanodic threshold between the samples, placed in every case around -0.05 V vs. SCE. The shuttered *J-V* curves in the presence of the Fe(III) catalyst show rectangular shaped photoanodic transients starting from 0.2 V vs. SCE indicating improved rectifying properties of the SCLJ in the presence of both the catalyst and the HTL-3 (Figure 6.10-b). Compared to the photoanodic plateau value, the relative intensity of the cathodic spikes is reduced in HTL-MPH type electrodes compared to MPH, suggesting, in the former, a lower extent of recombination occurring at the FTO/hematite interface. The appearance of transient features in the -0.2/-0.1 V vs. SCE interval is consistent with the photoanodic threshold evaluated under steady state conditions, providing a first approximate estimate of the flat band potential (-0.2 V vs. SCE) of these

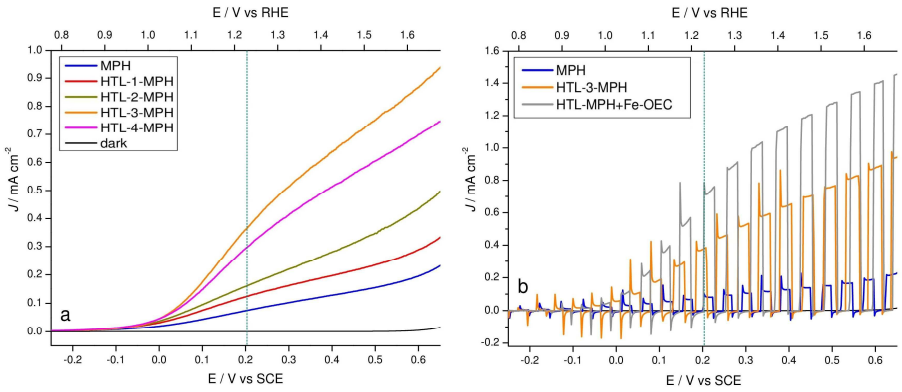

Figure 6.10. (a) *J-V* curves under continuous illumination of MPH deposited on FTO (blue line) and over HTL-1-4 samples (colored lines). (b) *J-V* curves under shuttered illumination of MPH deposited on FTO and HTL-3-MPH electrode before (orange line) and after (grey line) functionalization with Fe-OEC under AM 1.5 G illumination in NaOH 0.1 M (pH 13.3). The dotted vertical bar in (b) represents water oxidation potential at working pH value (1.23 V vs. RHE).

hematite electrodes at pH 13.3. All samples show an excellent stability under prolonged operating conditions (Figure 6.11-a), ruling out photocorrosion and degradation of the materials. The procedures used to assemble the single iron oxide structures (HTL, MPH and Fe-OEC) in the final device reveal a very good reproducibility with reference to the *J-V* response (Figure 6.11-b), considering that all the preparative steps involve solution based techniques.

The APCE (APCE=IPCE/LHE) spectra recorded at 0.6 V vs. SCE confirm the marked superiority of the HTL-3-MPH type electrodes, producing a quadruple internal quantum yield with respect to simple MPH. The presence of the catalyst further increases the quantum yield to ca. 20 % at 360 nm (Figure 6.12-a). The APCE spectra, being normalized for the LHE, confirm the intrinsic ability of the HTL-3-MPH electrodes to achieve a superior charge separation and collection over the MPH layer. It is interesting to note that the combined HTL-3-MPH electrode produces, at longer wavelengths (> 500 nm), APCEs comparable to that of the much thinner HTL-3 alone, whose nanometric thickness should allow for improved electron collection of charge carriers having short diffusion length.[16] Indeed, the HTL-3 is able to produce respectable performances, despite of the modest LHE, generating limiting photocurrents of the order of 0.65 mA cm^{-2} at 0.65 V vs. SCE by converting mostly high energy photons having short penetration depths (Figure 6.12-b).

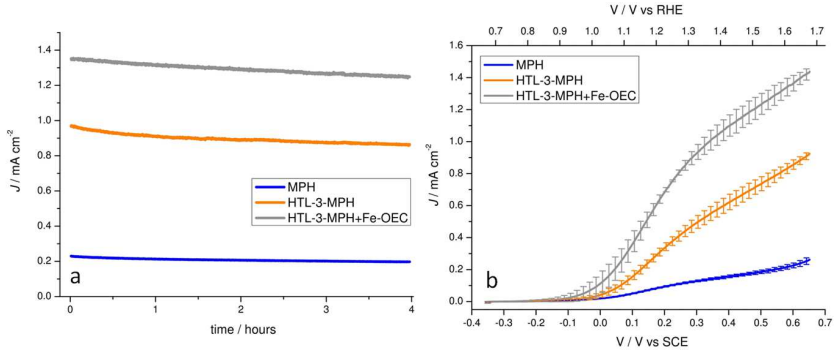

Figure 6.11. (a) Chronoamperometry of MPH, HTL-3-MPH and HTL-3-MPH+Fe-OEC recorded in NaOH 0.1 M (pH 13.3) under continuous AM 1.5G illumination at 0.6 V vs. SCE (b) Average *J-V* response with their relative error bars mediated over 12 different electrodes.

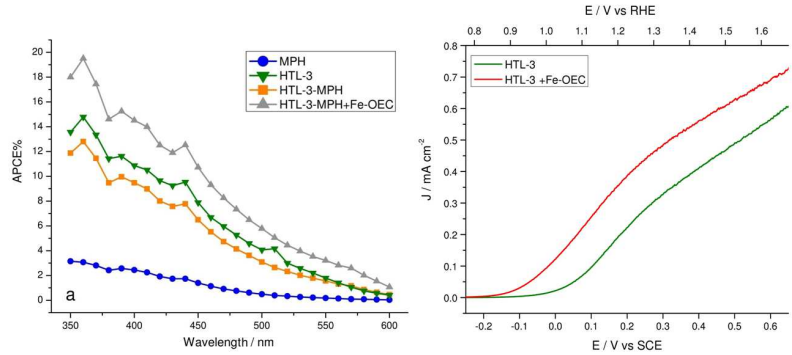

Figure 6.12. (a) APCE spectra recorded at 0.6 V vs. SCE in NaOH 0.1 M (pH 13.3) of MPH, HTL-3 and HTL-3-MPH with and without Fe-OEC. (b) *J-V* curves of HTL-3 sample before (green line) and after (red line) functionalization with Fe-OEC recorded in NaOH 0.1 M.

HTL performance varies in the order HTL-1 < HTL-2 < HTL-3 > HTL-4 (Figure B2). Thus in our conditions HTL-3 represents the best compromise between FTO coverage, thickness compatible with the short hole diffusion length and light harvesting properties. The addition of the catalyst directly onto the HTL-3 sample improves only slightly the photoactivity, with an overall current limited to ca. ½ of that obtained with the combined electrode, HTL-3-MPH, due to an insufficient harvesting of long wavelength photons (Figure 6.12-b).

6.5.1 Current-voltage behaviour with monochromatic light

We note that the initial individual performance of bare HTL cannot be compared to its performances after coverage by MPH, simply because the amount of HTL surface exposed to the electrolyte will vary in an unknown way and will be certainly reduced, decreasing its direct hole transfer pathways. The monochromatic *J-V* characteristics recorded both at 550 and at 600 nm (Figure 6.13 a-b), where the absorption of the HTL layer is negligible against photons having a penetration depth > 110 nm, reveal a distinct advantage of the combined HTL-3-MPH substrate generating from ca. x 2 to × 5 increase in photocurrent with respect to the sum of the separate contributions of HTL-3 and MPH. Thus, a substantially higher fraction of charge carriers, generated within the MPH layer, is able to reach the electron collector in the presence of HTL, indicating that the performance of the combined photoelectrode is not simply the superposition of the performances of the two distinct layers.

J^2-V plots, recorded under different monochromatic illumination wavelengths (350, 360, 550 and 600 nm) show a distinct linear dependence for HTL-3 and HTL-3-MPH substrates whereas for MPH on FTO the behaviour shows a more sigmoidal feature (Figure 6.14 a-b). Linear J^2-V plots, according to an approximation of the Gärtner model,[17] valid when the diffusion length of holes is small compared to the depletion length, as in the case of hematite,[18] is indicative of a mechanism of charge separation occurring within the space charge layer of the Schottky junction (Equation 6.2).[19]

$$J^2 = \Phi_0 \cdot \alpha^2 \frac{2 \cdot e \cdot \varepsilon \cdot \varepsilon_0}{N} (V - V_{fb}) \qquad (6.2)$$

This is quite reasonable for a thin layer of relatively compact oxide (HTL), which could be entirely depleted, but it is not necessarily obvious for the porous layer, which indeed, in the case of the MPH substrate alone, does not show a convincing dependence within the framework of the Gärtner approximation.

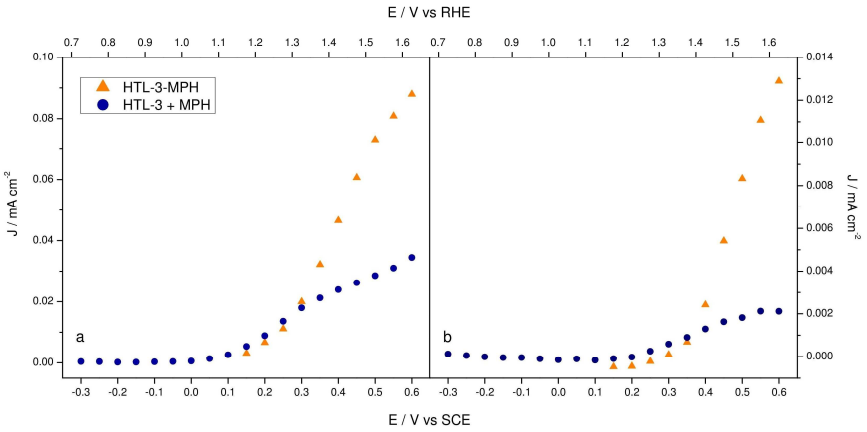

Figure 6.13. *J-V* curves of HTL-3-MPH and sum of the separate response of MPH and HTL-3 (navy circles) recorded with a (a) 550 and (b) 600 nm monochromatic light in NaOH 0.1 M.

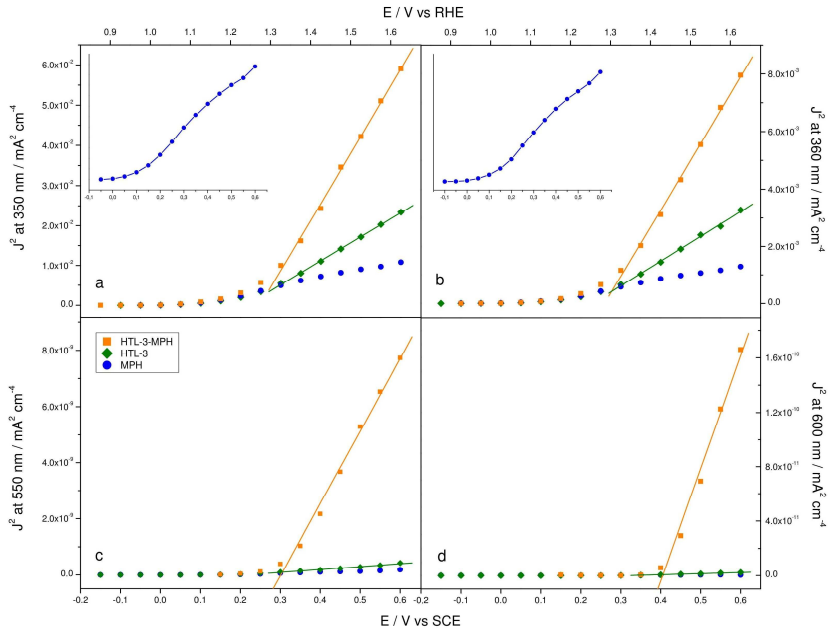

Figure 6.14. J^2 *-V* plot recorded with a monochromatic light at (a) 350 nm, (b) 360, (c) 550 and (d) 600 nm for MPH, HTL-3 and HTL-3-MPH samples in NaOH 0.1 M (pH 13.3). Insets in graphs (a) and (b) reported a magnification of MPH plot, showing its sigmoidal behaviour.

6.5.2 Photovoltage decays studies with a red-ox shutter

Photovoltage transients measured in the presence of a reversible red-ox couple $[Fe(CN)_6]^{4-}/[(Fe(CN)_6]^{3-}$ in which a defined formal potential is varied between 270

and 150 mV (vs. SCE), by changing the Fe(III)/(II) ratio (Figure 6.15), show that both the HTL-3 and HTL-3-MPH are capable of delivering a similar photovoltage (55-60 mV) which decreases 10 mV by reducing the formal potential of the redox couple from 270 to 210 mV, a behaviour expected in the case of formation of a built in potential due to voltage drop within the semiconductor. By contrast, the photovoltage generated by the MPH layer alone is essentially independent of the formal potential of the redox couple, reaching values of 4-6 mV, suggesting Fermi level pinning on surface states rather than potential drop within the space charge. Clearly these data have to be considered with caution since the Fe(II)/Fe(III) couple participates to recombination and hole scavenging events on the semiconductor surface and can alter, through kinetic processes, the final photovoltage value attained by the junction. Indeed, a further reduction of the formal potential to 150 mV, by introducing a 10-fold excess of Fe(II) with respect to Fe(III), leads to an increase in photovoltage for all substrates under investigation (80 and 100 mV for HTL-3 and HTL-3-MPH and 14 mV for MPH) probably due to improved hole scavenging by the Fe(II). In any case, photopotential measurements are consistent with improved charge separation in HTL-3 and in HTL-MPH type electrodes in the presence of a kinetically facile redox couple, evidencing superior SLCJ rectification properties. This is compatible with the presence of a substantial depletion layer within both the thin film alone (HTL-3) and the combined substrates (HTL-3-MPH).

6.6 Electrochemical Impedance Spectroscopy: analysis of the interfaces

The charge transfer dynamics of the modified hematite substrates were investigated primarily by scanning reverse potentials along the *J-V* curves under AM 1.5G illumination in the 10 mHz-100 kHz frequency interval, in order to individuate and characterize the active mechanisms responsible for the photocurrent generation. Typical Nyquist plots of hematite under illumination present two flattened arcs in the complex plane, having respectively maxima at low (0.1-1 Hz) and high frequency (100-1000 Hz) (Figure 6.16). Circuital models selected for the EIS data fitting reproduced accurately in all

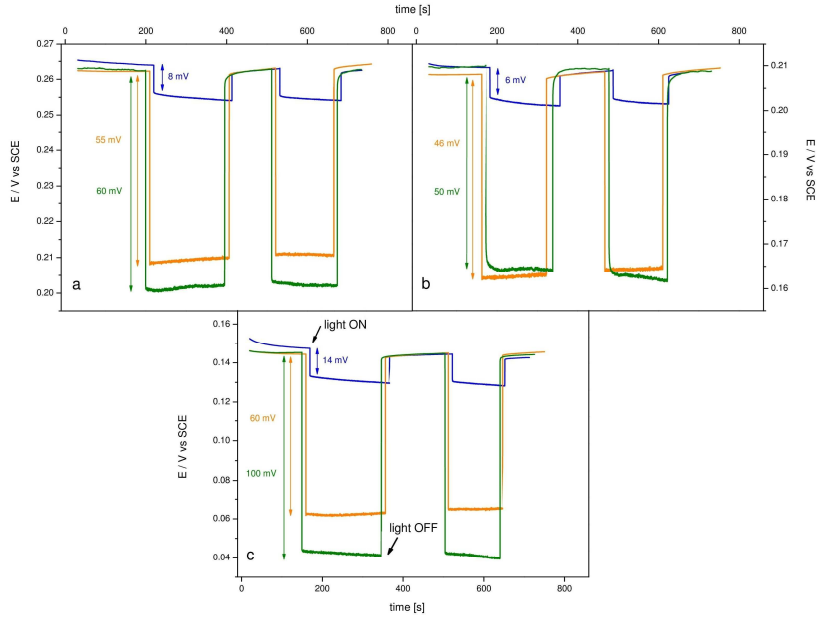

Figure 6.15. Photovoltage decays of MPH (blue line), HTL-3 (green line) and HTL-3-MPH (orange line) samples recorded at open circuit condition under shuttered illumination (100 mW cm^{-2}, AM 1.5G) in a KOH solution (0.1 M, pH 13.4) of $K_4[Fe(CN)_6]/K_3[Fe(CN)_6]$ at three different concentrations: (a) 20 mM Fe(II)/200 mM Fe(III); (b) 100 mM Fe(II)/100 mM Fe(III); (c) 200 mM Fe(II)/20 mM Fe(III).

cases (HTL-3, MPH, HTL-3-MPH with and without Fe-OEC) the *J-V* response, as can be appreciated from the excellent correlation between the inverse of the total resistance ($R_{tot} = \sum_{i=1}^{3} R_i$) obtained from EIS data and the derivative of the respective *J-V* curves (Figure 6.17).

In the case of samples where the iron oxide underlayer is present (HTL-3 and HTL-3-MPH with and without Fe-OEC) the circuital model comprises a nested mesh describing both the charge transfer across the depletion layer (R2-CPE1) and the Helmholtz layer (R3-CPE2) (inset 1 in Figure 6.16). In the HTL-3-MPH electrode the major contribution to the total resistance is determined by the interfacial charge transfer resistance at the solid/electrolyte interface (R3), reaching a minimum in correspondence with the inflection point of the *J-V* curves (maximum slope, Figure 6.18). The capacitance associated with the interfacial charge transfer process (modeled by Constant Phase Element, CPE2) follows a bell shaped distribution, peaking at 0.1 V vs. SCE and exhibiting a chemical capacitance behavior consistent with hole trapping in surface states exposed

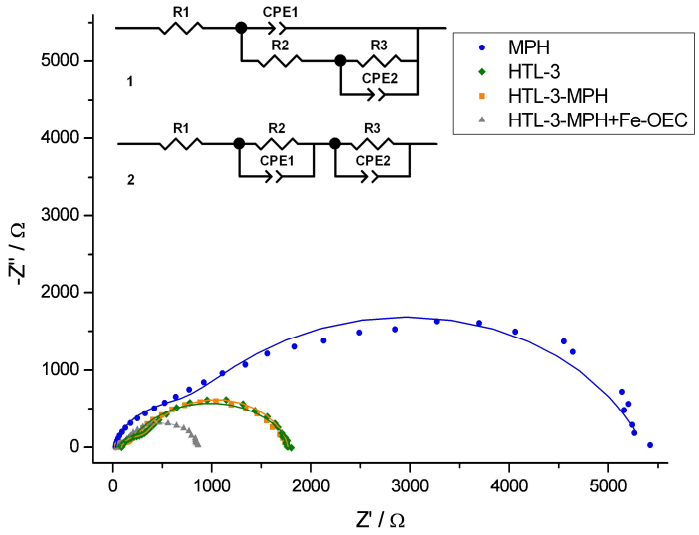

Figure 6.16. Nyquist plot recorded at 0 V vs. SCE under AM 1.5G illumination in NaOH (0.1 M, pH 13.3). (inset) Equivalent circuits used for fitting EIS data of (1) HTL-3 and HTL-3-MPH with and without Fe-OEC and (2) MPH electrodes. CPE2 represents the non ideal capacitance.

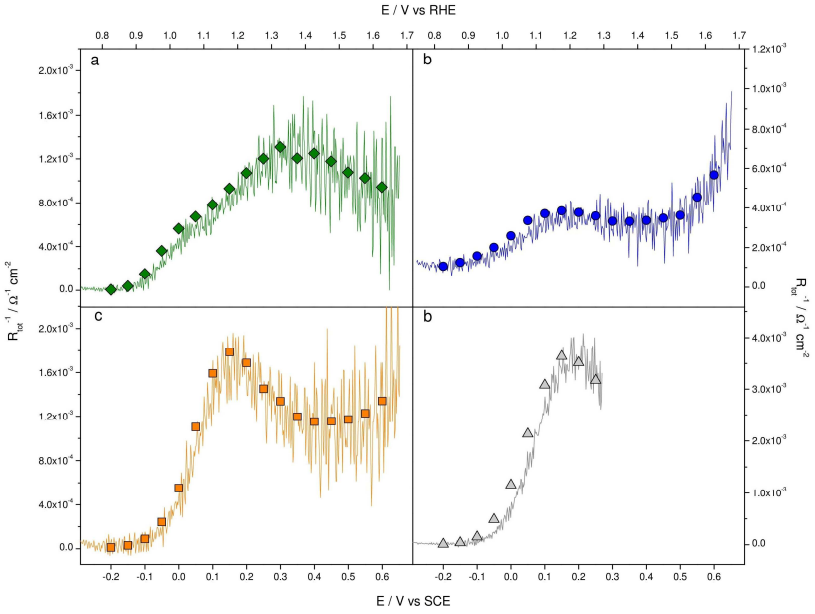

Figure 6.17. Derivative of the *J-V* curve (lines) compared to R_{tot}^{-1} obtained from EIS data (triangles) with models reported in Figure 6.16 for (a) HTL-3, (b) MPH, (c) HTL-3-MPH and (d) HTL-3-MPH with Fe-OEC samples.

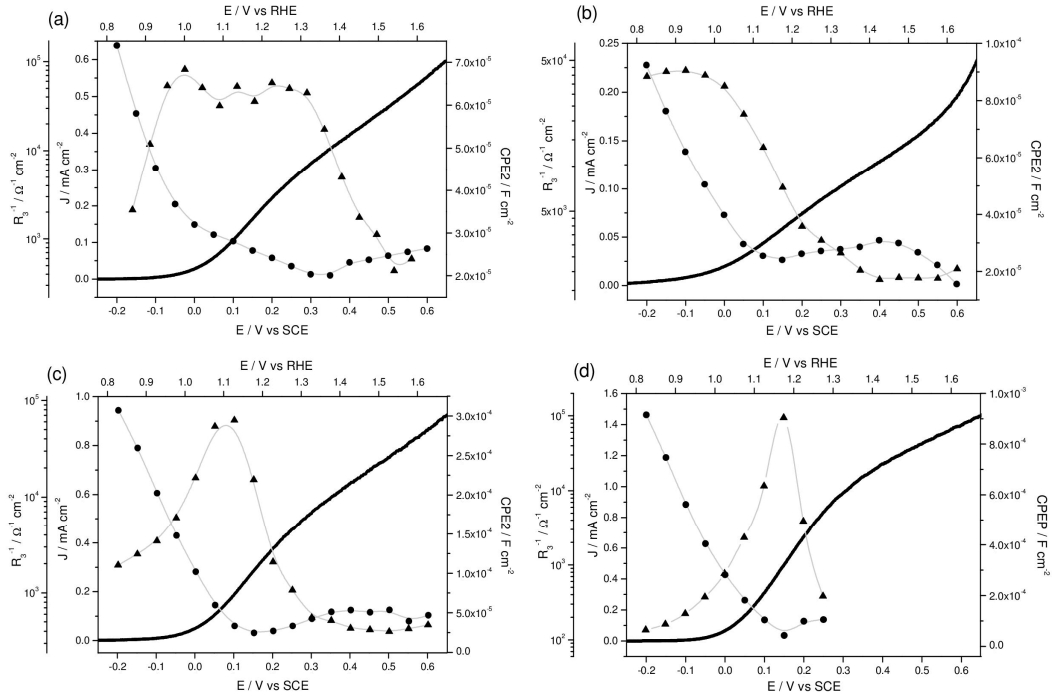

Figure 6.18. Plot reporting *J-V* curve (solid line), R_3 (circles) and CPE2 (triangles) values obtained for (a) HTL-3, (b) MPH, (c) HTL-3-MPH and (d) HTL-3-MPH with Fe-OEC under AM 1.5 G illumination.

to the electrolyte, that probably leads to the formation of highly valent iron species responsible for the water oxidation process.[20,21] Indeed, the chemical capacitance of the combined HTL-3-MPH electrode (0.3 mF cm^{-2}) is superior to the simple sum of the individual contributions of HTL-3 and MPH (0.15 mF cm^{-2}) (Figure 6.19-a), consistent with a superior charge separation and hole trapping capability, corroborating the indications from the monochromatic analysis of *J-V* characteristics. It can be further observed an additional substantial increase in chemical capacitance magnitude, from ca. 0.3 mF cm^{-2} to 1 mF cm^{-2} (Figure 6.19-a), in the presence of discontinuous islands of amorphous Fe(III) catalyst (HTL-3-MPH sample with Fe-OEC). This effect is also associated to a sharpening of the distribution and to a ca. 100 mV peak shift to more anodic potential, in agreement with the presence of surface species capable to capture and store photogenerated holes (Figure 6.18).[14] The MPH electrode alone, without the iron oxide thin underlayer, roughly parallels the behaviour already described for the HTL-3-MPH, although its interfacial capacitance values (max. 0.09 mF cm^{-2}) are much lower compared with the HTL-3 MPH and are associated to a considerably higher charge transfer resistance (2400 Ω cm^{-2} for

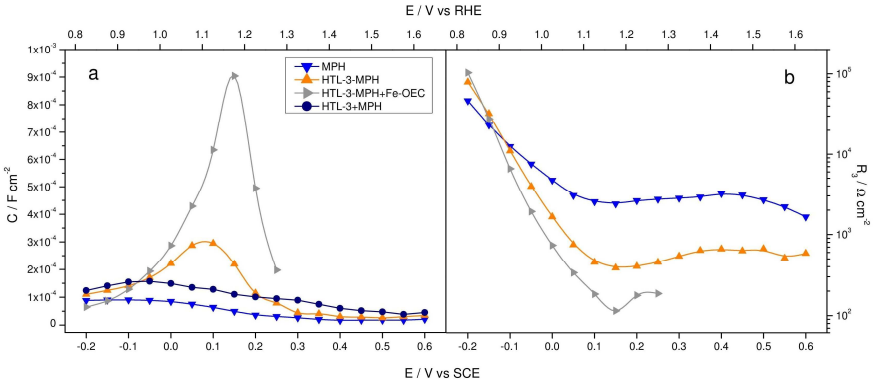

Figure 6.19. (a) CPE2 and (b) R_3 plot of MPH and HTL-3-MPH with and without Fe-OEC recorded under AM 1.5G illumination in NaOH (0.1 M, pH 13.3). In (a) is also reported the sum of the separate response of MPH and HTL-3 as navy circles.

MPH and 380 Ω cm^{-2} for HTL-3-MPH, Figure 6.19-b). These figures are in agreement with the lower photoelectrochemical performance of MPH, indicating that, in this latter case, the carriers are less capable to escape recombination and be directed to their respective interfaces where they are either collected or injected into the electrolyte.

The comparative analysis of the capacitance in the high frequency region (1 kHz) of HTL-3 and the HTL-3-MPH electrodes show a convincing Mott-Schottky behaviour with a linear portion providing a doping density of the order of $1.6 \pm 0.3 \cdot 10^{17}$ cm^{-3} (Equation 6.3), consistent with donor densities of un-doped hematite (Figure 6.20 a-b).[6]

$$N_D = \frac{2}{q \cdot \varepsilon_0 \cdot \varepsilon_{\alpha\ Fe_2O_3} \cdot b} \qquad (6.3)$$

With $\varepsilon_0 = 8.854 \cdot 10^{-12}$ F m^{-1}, $\varepsilon_{\alpha\text{-}Fe2O3} = 32$,[22] $q = 1.610 \cdot 10^{-19}$ C and b= slope of the linear section of Mott-Schottky plots ($A^2\,C^{-2}$ vs. V). Despite of some high frequency dispersion of the capacitive response of the junction, probably due to microroughness of the FTO/semiconductor/electrolyte interfaces,[6,23] reasonable values of flat band potentials, in agreement with those estimated by the photocurrent transients, were found with values ranging from -0.11 to -0.34 V vs. SCE (Table 6.1). The observation of a systematic positive shift of the flat band potential of the HTL-3-MPH electrode upon illumination,

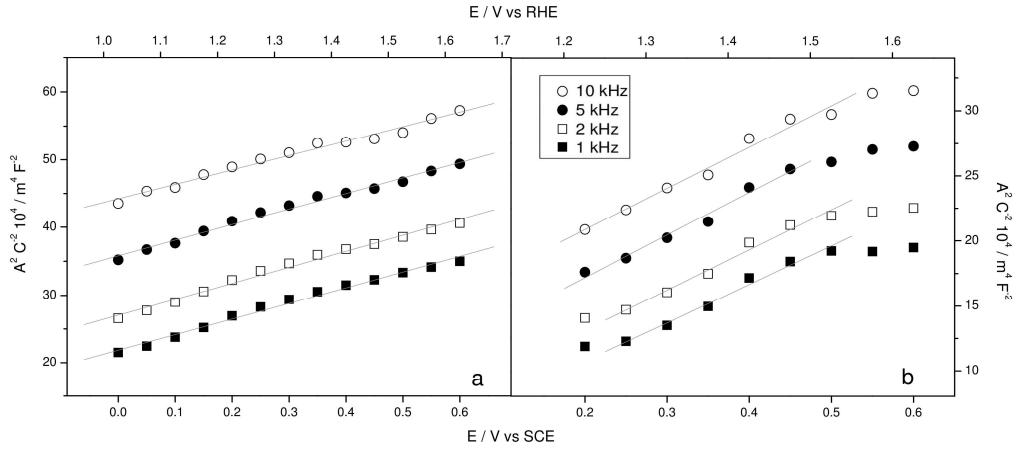

Figure 6.20. Mott-Schottky plot of (a) HTL-3 and (b) HTL-3-MPH recorded under AM 1.5G illumination in NaOH (0.1 M, pH 13.3) at different frequency (1, 2, 5 and 10 kHz).

Table 6.1. Values of flat band potential (V_{fb}) and charge carrier concentration (N_D) of HTL-3 and HTL-3-MPH. explainable by a potential drop within the Helmholtz layer caused by surface hole trapping, agrees with previous literature reports.[20]

	HTL-3		HTL-3-MPH			
	dark		dark		AM 1.5G	
Frequency kHz	V_{fb} V vs. SCE	N_D 10^{17} cm^{-3}	V_{fb} V vs. SCE	N_D 10^{17} cm^{-3}	V_{fb} V vs. SCE	N_D 10^{17} cm^{-3}
1	-0.73	1.66	-0.30	1.03	-0.11	1.48
2	-0.93	1.68	-0.36	1.04	-0.17	1.43
5	-1.25	1.65	-0.51	1.06	-0.27	1.34
10	-1.14	2.43	-0.68	1.03	-0.34	1.27

By contrast the MPH layer does not show any MS dependence associated with the high frequency arc, showing essentially a random distribution of the high frequency capacitance with the applied voltage under illumination, indicating that in this case the high frequency capacitive response is essentially decoupled from the dynamic processes responsible for photocurrent generation. Likely, the high frequency capacitance could be due to geometric factors (i.e. electrode porosity) or to a passive interface which does not play an active role in photocurrent generation, as confirmed by the associate resistance which is nearly potential independent. For this reason, the equivalent circuit used for

describing its impedance response is comprised of two separated RC meshes (inset 2 in Figure 6.16). The MS analysis carried out in the dark for the HTL-3 and HTL-3-MPH samples are still consistent with the formation of a depletion layer extending into the hematite material, providing a donor density similar to that obtained under illumination (ca. 10^{17} cm^{-3}), whereas the MPH electrode was characterized by a linear MS behaviour with substantially different doping density, of the order of 10^{21} cm^{-3} (Figure 6.21), attributed to a narrow depletion layer developing into conductive FTO[24] which, under illumination, does not have active participation in the charge separation dynamics within porous hematite. The depletion length calculated with the hematite donor densities extracted from the MS plots yields values of the order of 130 nm at 0.2 V vs. SCE (1.23 V vs. RHE), indicating that even photons having a deep penetration in the porous layer have considerable chance to generate charge carriers experiencing an electric field which assists charge separation, directing electron to the back contact and holes to the surface where trapping occurs. This allows to well explain both the enhanced photoanodic response of the hematite electrodes modified with the thin underlayer (HTL-3-MPH) to excitation wavelengths > 500 nm and the increased interfacial hole trapping capacitance. Clearly, the performance of the compact HTL-3 alone is also satisfactory, in relation to its poor light absorption capabilities, due to the fact that this film is most probably entirely depleted and charge carriers are generated within a distance from the collector which is compatible with their short diffusion lengths.

Thus the EIS analysis corroborates the indications obtained from DC photoelectrochemical experiments: in the MPH sample alone, the Fermi level is probably pinned on surface states which could be created during deposition and annealing of Fe_2O_3 nanoparticles on FTO, due to lattice mismatching between these two materials, preventing the possibility of controlling the formation of a depletion layer which would assist charge separation. This effect is largely reduced by the use of the HTL, which, acting as a buffer layer between the porous photoactive layer and FTO, reduces the possibility of trap states formation, consequently avoiding, at least to a sufficient extent, pinning of the Fermi level on defects. The elimination of defects and grain boundaries at the hematite-FTO interface was invoked by Isatomi *et al.* as the main role played by ultrathin

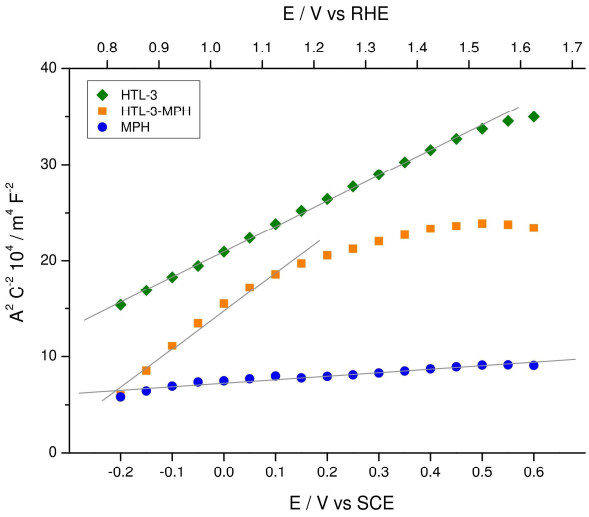

Figure 6.21. Mott-Schottky plot of MPH, HTL-3 and HTL-3-MPH recorded in the dark at 1 kHz in NaOH (0.1 M, pH 13.3). For MPH, the roughness factor was considered the same as that of HTL (15), given that the latter is essentially conformal to the FTO, and $\varepsilon = 10$[25] in the donor density calculations from MS fitting.

6.7 Photoluminescence analysis

To further support the role of the HTL layer in the prevention of trap state formation, photoluminescence spectra (PL) have been recorded (Figure 6.22). It has been shown that the reduction of the amount of surface trap states in hematite photoanodes after overlayer deposition or solution passivation results in an enhancement of photoluminescence,[26,27] since these states behave as non radiative recombination centres of excitons.[28] The difference emission spectra of HTL-3-MPH and MPH (520 nm excitation light) shows a relatively broad emission peaking at 615-620 nm, consistent with earlier reports of luminescence arising from passivated hematite electrodes, corroborating a decreased defect density induced by HTL acting as buffer later between MPH and FTO.

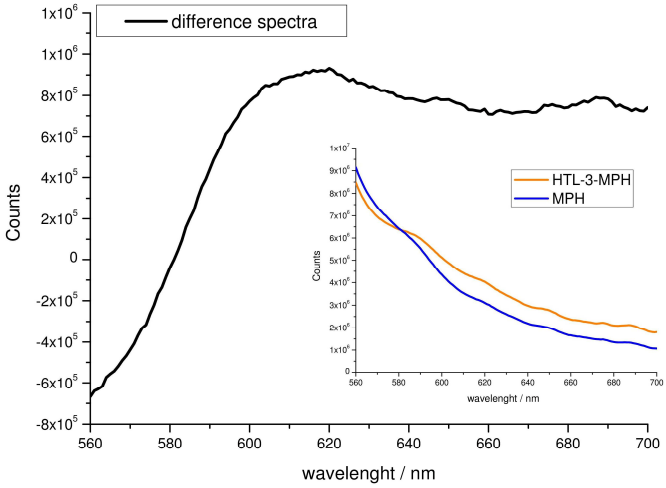

Figure 6.22. Difference photoluminescence emission spectra (PL) of HTL-3-MPH and MPH. (Inset) PL spectra (520 nm excitation light) of MPH and HTL-3-MPH.

6.8 Conclusions

The photoelectrochemical effect of a thin layer of spin coated crystalline hematite acting as a host surface for the electrophoretic deposition of mesoporous Fe_2O_3 nanoparticles was explored. The new combined hematite photoanode, entirely obtained with wet solution methods and without introduction of external dopants, exhibits a four-fold improvement in photoactivity over the simple hematite mesoporous film, reaching a stable limiting photocurrent density of ca. 1 mA cm^{-2} at 0.65 V vs. SCE under AM 1.5G illumination. The improved performance results in part from the individual properties of the two layers, in which the thin underlayer, efficient in charge collection, captures mostly high energy photons while the thicker mesoporous layer harvests longer wavelength visible radiation.

However, the photoelectrochemical response of the combined HTL-MPH electrode is not the simple superposition of the properties of the two materials, as can be revealed by the improved charge separation and collection observed upon excitation with deeply penetrating photons, (α^{-1}_{λ} > 100 nm) generating carriers mostly in the thick porous film. The combination of DC and EIS indicates that the electric field within a depletion layer, extending for a substantial fraction of the whole HTL-MPH electrode, has a role in driving

the charge carriers towards the two different interfaces, where they are collected (electrons at FTO) or trapped in reactive states and transferred to the electrolyte (holes). This observation is consistent with the presence of the HTL that, acting as a buffer layer between the porous photoactive hematite film and FTO, can reduce the possibility of trap states and grain boundaries formation avoiding pinning of the Fermi level on defects.

This mechanism of action of the thin host underlayer, which contrary to other literature approaches, is transparent to conduction band electrons, is different from those reported for other semiconductor oxides acting as insulating/tunneling junctions, and may represent a convenient scalable method to improve the selectivity of the interfaces to the respective charge carriers in sol-gel hematite photoelectrodes. A further improvement to a photoanodic limiting value of 1.5 mA cm^{-2} at 0.65 V vs. SCE is observed after decoration of the hematite surface with an Fe(III)-OEC, representing one of the highest photocurrent values for un-doped all-iron based photoelectrodes entirely realized with simple wet solution procedures.

6.9 References

1 L. Steier, I. Herraiz-Cardona, S. Gimenex, F. Fabregat-Santiago, J. Bisquert, S. D. Tilley and M. Grätzel, *Adv. Funct. Mater.*, **2014**, *24*, 7681.

2 F. Le Formal, M. Grätzel and K. Sivula, *Adv. Funct. Mater.*, **2010**, *20*, 1099.

3 T. Hisatomi, J. Brillet, M. Cornuz, F. Le Formal, N. Tétreault, K. Sivula and M. Grätzel, *Faraday Discuss.*, **2012**, *155*, 223.

4 C. Zhang, Q. Wu, X. Ke, J. Wang, X. Jin and S. Xue, *Int. J. Hydrogen Energ.*, **2014**, *39*, 14604.

5 O. Zandi, J. A. Beardslee and T. Hamann, *J. Phys. Chem. C*, **2014**, *118*, 16494.

6 Y. Liang, C. S. Enache and R. van de Krol, *Int. J. Photoenergy*, **2008**, *2008*, 1.

7 X. Zong, S. Thaweesak, H. Xu, Z. Xing, J. Zou, G. Lu and L. A. Wang, *Phys. Chem. Chem. Phys.,* **2013**, *15*, 12314.

8 F. L. Souza, K. P. Lopes, P. A. P. Nascente and E. R. Leite, *Sol. Energy Mater. Sol. Cells*, **2009**, *93*, 362.

9 J. Frydrych, L. Machala, J. Tucek, K. Siskova, J. Filip, J. Pechousek, K. Safarova, M. Vondracek, J. H. Seo, O. Schneeweiss, M. Grätzel, K. Sivula and R. Zboril, *J. Mater. Chem.*, **2012**, *22*, 23232.

10 C. Aydın, S. A. Mansour, Z. A. Alahmed and F. Yakuphanoglu, *J. Sol-Gel Sci. Technol.*, **2012**, *62*, 397.

11 A. M. Jubb and H. C. Allen, *ACS Appl. Mater. Interfaces*, **2010**, *2*, 2804.

12 L. A. Marusak, R. Messier and W. B. White, *J. Phys. Chem. Solids*, **1980**, *41*, 981.

13 K. Itoh and J. O. Bockris, *J. Electrochem. Soc.*, **1984**, *131*, 1266.

14 N. Dalle Carbonare, V. Cristino, S. Berardi, S. Carli, R. Argazzi, S. Caramori, L. Meda, A. Tacca and C. A. Bignozzi, *ChemPhysChem.*, **2014**, *15*, 1164.

15 V. Cristino, S. Berardi, S. Caramori, R. Argazzi, S. Carli, L. Meda, A. Tacca and C. A. Bignozzi, *Phys. Chem. Chem. Phys.*, **2013**, *15*, 13083.

16 B. Klahr, A. B. Martinson and T. W. Hamann, *Langmuir*, **2011**, *27*, 461.

17 D. Guyomard, *Journal de Chimie Physique*, **1986**, *83*, 355.

18 J. H. Kennedy and K. W. Frese, *J. Electrochem. Soc.*, **1978**, *125*, 709.

19 In Equation 6.2, J is the photocurrent density, Φ_0 the incident photon flux, α the absorption coefficient, ε_0 and ε the vacuum and semiconductor permittivity, N the donor density, V the applied potential and V_{fb} the flat band potential.

20 B. M. Klahr, S. Gimenez, F. Fabregat-Santiago, T. Hamann and J. Bisquert, *J. Am. Chem. Soc.*, **2012**, *134*, 4294.

21 B. Klahr, S. Gimenez, F. Fabregat-Santiago, J. Bisquert and T. W. Hamann, *Energy Environ. Sci.*, **2012**, *5*, 7626.

22 J. A. Glasscock, P. R. F. Barnes, I. Plumb, A. Bendavid and P. J. Martin, *Thin Solid Films*, **2008**, *516*, 1716.

23 G. Oskam, D. Vanmaekelbergh and J. J. Kelly, *J. Electroanal. Chem.*, **1991**, *315*, 65.

24 A. Bak, W. Choi and H. Park, *Appl. Catal., B*, **2011**, *110*, 207.

25 G. Boschloo and D. Fitzmaurice, *J. Phys. Chem. B*, **1999**, *103*, 3093.

26 F. Le Formal, N. Tétreault, M. Cornuz, T. Moehl, M. Grätzel and K. Sivula, *Chem. Sci.*, **2011**, *2*, 737.

27 M. Zhang, W. Luo, N. Zhang, Z. Li T. Yu and Z. Zou, *Electrochem. Comm.*, **2012**, *23*, 41.

28 B. S. Zou and V. Volkov, *J. Phys. Chem. Solids*, **2000**, *61*, 757.

CHAPTER 7

ADDITION OF TITANIUM(IV) BUTOXIDE DURING ELECTROPHORETIC IRON OXIDE DEPOSITION: EFFECT ON HEMATITE PHOTOACTIVITY

7.1 Introduction

In the previous Chapters, we have employed different strategies to enhance the efficiency of hematite towards the water oxidation reaction, including (i) nanostructuring to alleviate the high recombination rate of the photogenerated carriers and to accommodate the short hole diffusion distance, (ii) modification of the surface with co-catalyst base on iron(III) to overcome the slow kinetics of water oxidation causing the high overpotential and (iii) introduction of a thin iron oxide layer at the FTO/hematite junction that drives the charge carriers towards the two different interfaces, where they are collected (electrons at FTO) or trapped in reactive states and transferred to the electrolyte (holes) avoiding recombination.

Among these strategies, additional efforts toward improving the charge collection efficiency consist of intentionally incorporating impurity atoms into the hematite lattice. There are numerous examples on improved water splitting activity upon the introduction of high levels of impurities such as Si, Pt, Mn, Cr, Al, Ge, W, Rh and Ag.[1-9] The term 'doping' is conventionally used for large loading typically employed (1–10 atomic%), whereas formally in semiconductor physics it is only referred to very small relative amounts (sub-ppm concentration). Doping has been mostly achieved by sputtering,[1] chemical deposition,[10] pulsed laser deposition (PLD)[11] and hydrothermal methods,[12] showing in all cases a significant photocurrent increase.

Regarding Ti doping, there are several ways by which the dopant can improve, in principle, the performance of hematite films, although the specific cause of any improvement has not been unambiguously determined. In particular, the dopant could increase the electronic density and thus the conductivity of the pristine semiconductor, but also the minority carrier mobility and/or their lifetime, allowing more holes to reach the semiconductor/electrolyte interface. For example, Wang *et al.*[10] noticed that titanium acts as n-type dopant causing an increase of the electron concentration, while Hahn *et al.*[13] attributed the high efficiency of titanium-doped hematite films to both the improved electron transport within the bulk of the film and the suppression of the recombination at the SC-electrolyte interface because of a stronger electric field near the surface. Furthermore, Rioult *et al.*[14] observed an increase of the carrier concentration combined with higher carrier diffusion lengths in Ti-doped epitaxial hematite thin films. Dopants can also improve the crystallinity of the hematite lattice or act as structural directing agents to produce more suitable nanostructured architectures with better capability in light absorption properties. Miao *et al.*[15] reported that Ti doping induces a change in nanostructure size and shape and Deng *et al.*[16] a modification of the type of hematite nanostructure and crystallographic orientation. However, it seems more likely that the overall effect should be ascribed to a combination of different effects, both on morphology and bulk properties, as suggested by Zandi *et al*.[17]

Alternatively, the dopants can passivate surface states and/or grain boundaries, thus reducing surface state recombination. Franking *et al.*[18] used a Ti post-doping treatment

through drop casting of a Ti(IV) precursor onto hematite electrodes, showing both an increased carrier density and surface state passivation. Actually, post synthetic treatments followed by high temperature annealing, are more likely responsible for the formation of TiO_2 pure (titania) or mixed phases on the hematite surface, probably due to the diffusion of titanium to the hematite surface and its successive oxidation. Ahmed *et al.*[19] has recently reported improvement in the photoactivity of hematite after deposition of a thin TiO_2 layer using a water-soluble titanium complex, due to the suppression of surface electron−hole recombination. These overlayers should be thin enough (< 5-10 nm) to allow a tunneling charge transfer from the semiconductor to the solution, due to the energetic mismatch between hematite and titania energy bands. In 2015, Morante *et al.*[20] prepared hematite/titania composite thin films with different molar ratio (from 0% to up 20%), claiming that both the improved conductivity and the presence of a pseudo-brookite (Fe_2TiO_5) phase on the hematite surface were the responsible for the improved performances of doped samples. These results show that it is not possible to exclude a multiple effect of titanium, that can act both as a real doping agent, in terms of substitution of iron cations within the hematite lattice, and as a passivating oxide overlayer, facilitating the hole transfer throughout the SCLJ. In fact, the surface modification of semiconductor photoelectrodes with passivating overlayers is an effective strategy to improve the charge-separation and charge-transfer processes across the SCLJ. For instance, the stability and the efficiency for water oxidation of Si, GaAs and GaP photoanodes can be greatly enhanced by coating their surfaces with a TiO_2 overlayer using atomic layer deposition (ALD).[21]

We thus decided to modify our previously reported electrophoretic deposition methodology to investigate the effect of the incorporation of titanium in mesoporous hematite films, by using Ti(IV) butoxide as dopant precursor. This solution-based procedure allows us to easily vary the amount of titanium added, obtaining different nominally doped samples Besides being easy to implement and scale up, this procedure could be flexibly employed to screen other metal dopants in the form of soluble precursor. All Ti(IV) modified hematite samples show an improved photoactivity with respect to the un-modified electrode, reaching the best performance with a 5% of

titanium incorporation (exhibiting a 4-fold photocurrent enhancement with respect to the un-treated electrode). AFM and XPS analysis reveal the presence of a TiO_2 phase on the semiconductor surface, that covers the iron oxide nanoparticles, probably reducing grain boundaries increasing charge transport, as corroborated also by EIS. Nevertheless, Mott-Schottky plots of the high frequency capacitance show a 3-fold increase in donor density in the 5%-Ti modified sample with respect to un-modified hematite, ascribable to the introduction of titanium ions in the hematite lattice. Preliminary results thus confirm that improvement in the photoactivity can be directly ascribed to the titanium, acting both as doping agent and as a passivating overlayer in the form of the corresponding oxide.

7.2 Modification of the electrophoretic deposition procedure

For the preparation of mesoporous hematite electrodes we have employed the same electrophoretic methodology described in Chapter 6, without any modification, as well as for the SILAR deposition of the iron(III) water oxidation catalyst. For the preparation of titanium-modified hematite samples, different amounts of a 10^{-2} M titanium (IV) butoxide solution in ethanol was added to the iron oxide deposition solution just before the application of the 10 V potential. The nominal concentration of the added titanium(IV) added was 0, 1, 2, 5 and 10% with respect to the molar concentration of iron, considering quantitative the conversion of $FeCl_3 \cdot 6H_2O$ in Fe_2O_3 nanoparticles during the hydrothermal growth. Different volumes of ethanol were added to the deposition solution to keep constant the acetone/ethanol ratio (49:1). After the deposition, samples were rinsed with acetone and sintered in air at 550 °C for 2 hours, followed by a 800 °C annealing step for 10 minutes. The use of absolute ethanol was necessary to avoid the hydrolysis of titanium(IV) butoxide and the consequent formation of TiO_2 nanoparticles in case of contamination by water traces.

7.3 Effect of titanium on the morphology and composition of the surface

Detailed mapping of the un-modified and the 10%-Ti modified hematite samples are presented in Figure 7.1. Morphological differences of the semiconductor surface are evident from both the top-view AFM images and the 3D maps taken for a 5 x 5 µm area. In the un-modified sample, the surface is quite homogeneous, with iron oxide rods aligned perpendicularly to the basal plane with a diameter estimable < 100 nm and clustered together in bigger domains. Although the hydrothermal growth of iron oxide nanoparticles does not allow to rigorously control the dimension of the nanoparticles, AFM images reveal that the rods seems to be quite homogeneously distributed in both shape and size. When titanium is added, the nanoparticles appear more intimately sintered together, resulting in bigger lumps having a rounder and smoother shape. These features may lead to a better charge transport across the fused nanostructures through the reduction of grain boundaries.

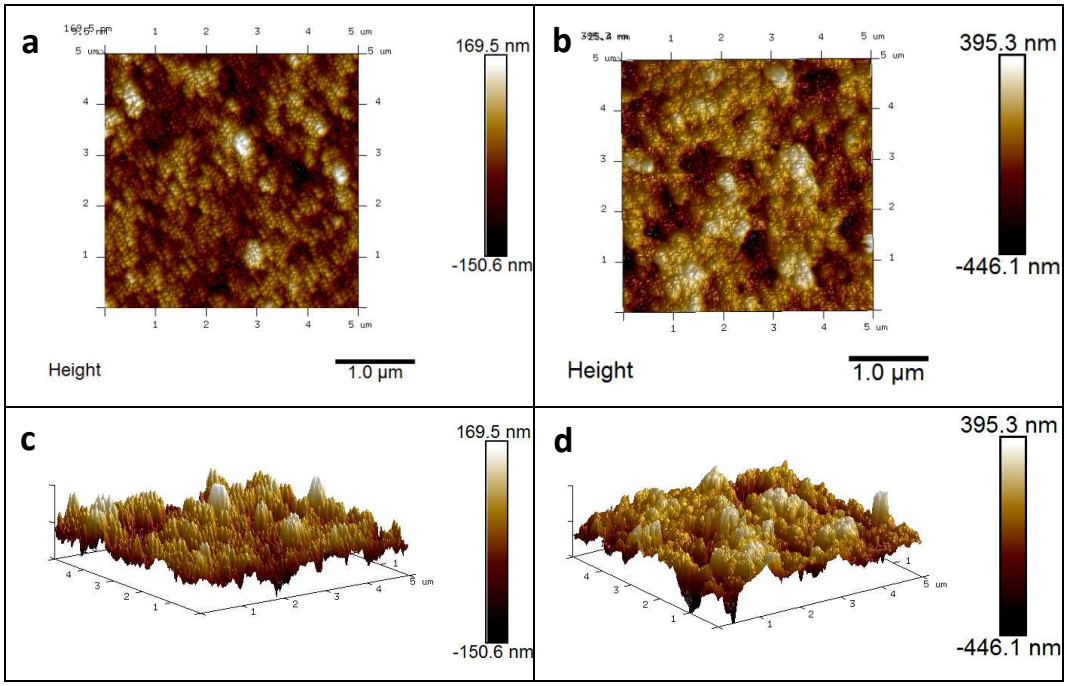

Figure 7.1. AFM top view images and 3D maps of un-modified (a, c) and 10%-Ti modified (b, d) hematite surface.

In order to analyze the surface of the material in search of changes upon Ti incorporation, both un-modified and Ti modified (5 and 10%) hematite films have been investigated by XPS (Figure C1 in Appendix C). Binding energies were calibrated on C 1s peak (B.E. = 284.8 eV) (Figure C2). The XPS spectra of the Fe 2p core are reported in Figure 7.2. They exhibit binding energies of 711.3 and 725.0 eV corresponding to the Fe $2p_{3/2}$ and Fe $2p_{1/2}$ lines, respectively. Typical Fe^{3+} shake-up satellites appear correctly separated by 8 eV from the main Fe 2p peaks (dotted bars in Figure 7.2),[23] indicating that Fe^{3+} is the dominant ionic species in all the films. The absence of detected Fe^{2+} species excludes polaron hopping in Ti-modified hematite samples (orange and black lines) due to incorporation of titanium in the hematite lattice ($Fe^{3+} + Ti^{4+} \rightarrow Fe^{2+} + Ti^{3+}$).[24] Furthermore, Fe 2p signals do not suffer from peak shifts upon Ti incorporation, clue that the Fe^{3+} cations experienced the same chemical neighbourhood in both the modified and un-modified samples. Figure 7.2 also shows the Ti 2p core signal for the modified samples, splits into the $2p_{3/2}$ (B.E. = 458.7 eV) and $2p_{1/2}$ (B.E. = 464.4 eV) peaks. No peaks are detected in this region for the un-modified hematite film (blue line in Figure 7.2). The presence of the two Ti 2p components is consistent with the valence of Ti^{4+} in the TiO_2 phase.[19] Ti 2p peak shows a progressive relative intensity increase with the doping level with reference to the Fe 2p signal, calculated as 50% and 31% respectively for the 10% and the 5%-Ti modified samples, indicating a thicker TiO_2 surface layer for the 10%-Ti sample. The relative Ti/Fe intensity only slightly changes when analyzing the electrodes with a 20° take off angle. The ratio is nearly constant in the 5% sample while it increases of about 15% with respect to the 45° measurement, suggesting the formation of a thicker TiO_2 layer in the 10%-Ti sample.

The XPS analysis confirmed the presence of a TiO_2 phase onto the hematite surface, with a thickness that roughly depends on the initial amount of precursor used during the deposition step: the higher is the concentration of titanium(IV) butoxide and the higher is the amount of TiO_2 detected. No evident proofs of the incorporation of titanium inside the hematite lattice are deducible at this stage. The presence of a thin layer of titanium dioxide can be explained by the surface adsorption and hydrolysis of the titanium(IV) precursor during the high temperature annealing. Furthermore, the presence of titanium does not seem to have any effect on the orientation of the iron oxide nanoparticles on

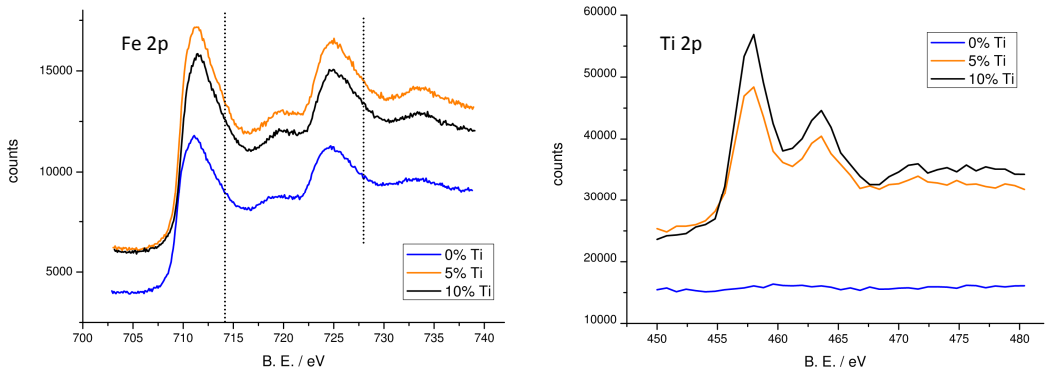

Figure 7.2. (left) Fe 2p and (right) Ti 2p core level XPS spectra for un-modified (black line), 5% (orange line) and 10%-Ti modified (black line) hematite samples. Dotted bars in the Fe 2p spectra indicate Fe^{3+} shake-up peaks. Measurements have been performed with a 45° take off angle.

the FTO. Iron oxide nanoparticles obtained after the first hydrothermal step already show good crystallinity (see Chapter 6). The presence of a thin TiO_2 shell on the top of the films is consistent with the smoother morphology observed from AFM images, helping to fill the gaps between the nanoparticle domains and forming larger conglomerates with improved adhesion and sintering of the nanoparticles, consistent with the spectrophotometric results. UV-Visible spectra (Figure 7.3) show indeed increased absorption related in a non-linear fashion to the nominal concentration of titanium butoxide employed with respect to the un-modified sample. The typical α-Fe_2O_3 absorption features are preserved in the modified samples, showing in all cases the same absorption threshold, indicating no change in the band gap of hematite by introducing Ti(IV).

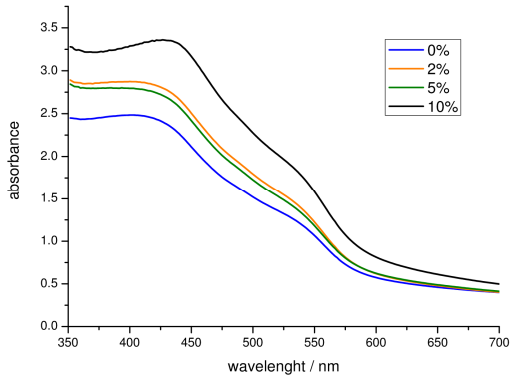

Figure 7.3. UV-Visible spectra of un-modified and Ti-modified hematite electrodes.

7.4 Photoelectrochemical properties

In order to understand the effect of the Ti-treatment, we compared the water oxidation photocurrent density *vs.* potential recorded in 0.1 M NaOH (pH 13.3) under AM 1.5G continuous illumination (100 mW cm^{-2}) shining from the FTO side. Interestingly, the introduction of titanium(IV) butoxide during the electrophoretic deposition of the films results in a significant enhancement of the anodic photocurrent for all the modified hematite samples in comparison with the un-modified hematite (Figure 7.4-a). As the percentage of titanium precursor is increased from 0% to 5%, the photocurrent increases from ca. 0.25 mA cm^{-2} up to 1.0 mA cm^{-2} at 0.65 V vs. SCE, decreasing again at larger percentages. The performance of un-doped hematite is in excellent agreement with previous results obtained using the same deposition technique (Chapter 6), with a very good reproducibility among different samples (Figure 7.5).

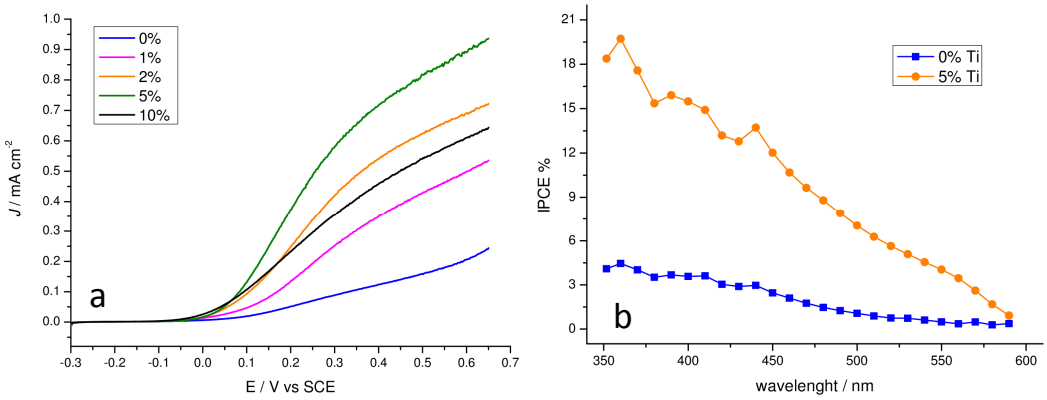

Figure 7.4. (a) *J-V* response of doped and un-modified hematite samples under AM 1.5G illumination (100 mW cm^{-2}) in NaOH 0.1 M. (b) IPCE spectra of un-modified and 5% Ti-modified hematite electrodes recorded at 0.6 V vs. SCE.

IPCE spectra recorded at 0.65 V vs. SCE confirmed the superiority of the 5%-Ti, producing a 4-fold improvement of the quantum internal yield with respect to simple hematite (Figure 7.4-b), in good agreement with the *J-V* behavior. Given that the absorption at wavelength < 600 nm are for both the samples quantitative (Figure 7.3), differences in

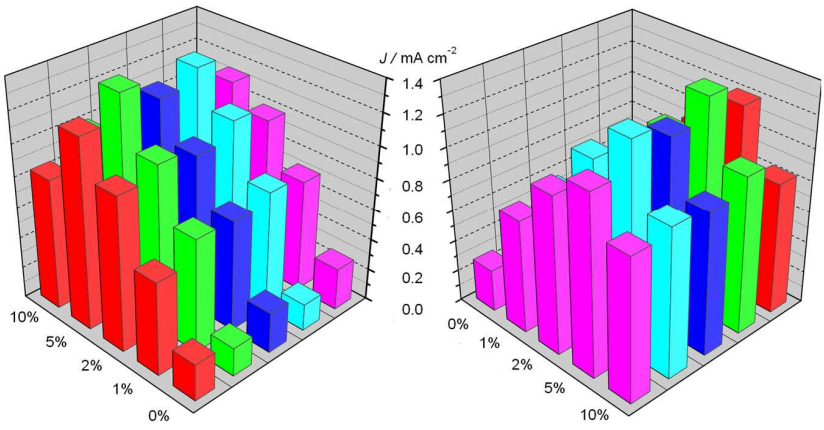

Figure 7.5. Comparison of the photoactivity of different batches (colored bars) of modified and un-modified hematite electrodes measured under AM 1.5 illumination. The histogram is shown from two different perspectives for clarity. Nominal titanium concentrations are reported in the x-axis.

IPCE values are thus ascribable to different capability in charge transfer properties, with a lower degree of photogenerated carriers lost by recombination in the Ti-modified sample. Illumination from the electrolyte side (front side) reduced dramatically the photocurrent in the un-doped hematite, limited to less than 0.1 mA cm^{-2} at 0.6 V vs. SCE, while this effect is less pronounced in the 5%-Ti modified samples (Figure 7.6-a). Given that the light penetration depth of hematite is reported to be 118 nm, illumination from the electrolyte side generates charge carriers far from the FTO contact resulting in a poor electron collection ability. The presence of titanium significantly alleviates this problem, probably by both increasing the hematite conductivity and passivating surface trap states. After the SILAR deposition of the iron(III) water oxidation catalyst, a 40% increased photocurrent is achieved at 0.6 V vs. SCE, coupled with a ca. 100 mV cathodic shift on the onset potential (Figure 7.6-b). As already described in the previous chapters, the presence of discontinuous amorphous iron oxide on the hematite surface have a beneficial effects thank to the possibility to store oxidizing equivalents in reactive states exposed to the electrolyte. Both the enhancement of the limiting current plateau and the decreased photocurrent onset potential testify a more favorable transfer of photogenerated holes to the solution, avoiding losses of charge carriers due to recombination mainly in surface trap states.[24]

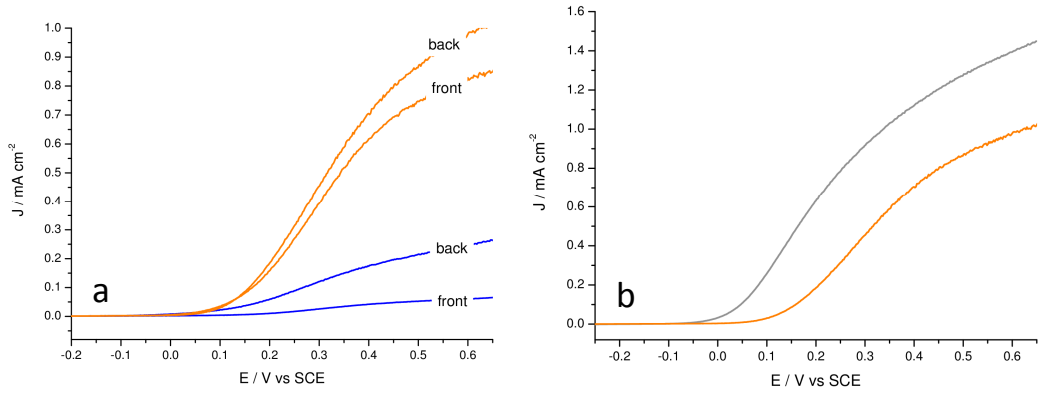

Figure 7.6. (a) Comparison between back (FTO side) and front (electrolyte side) illumination for un-doped (blue lines) and 5%-Ti doped (orange lines) hematite electrodes. (b) *J-V* curves of 5%-Ti doped hematite before (orange line) and after (grey line) functionalization with Fe-OEC.

7.5 Impedance analysis of the un-modified and the 5%-Ti modified electrodes

EIS was performed under illumination for un-modified and 5%-Ti modified samples in order to understand the role of titania and to address the active elements responsible for charge generation and separation by scanning the *J-V* in the potential region between -0.1 and 0.6 V vs. SCE. Physical model comprises a nested circuit where two parallel meshes model the charge transfer across the space charge region and the hole transfer through surface trapped intermediates (Figure 7.8-b). Typical Nyquist plots for the two samples are exemplified in Figure 7.7, where three different representative potentials along the *J-V* curve were chosen: close to the photocurrent onset (0 V vs. SCE), the rising part of the *J-V* curves (0.2 V vs. SCE) and the proximity of the thermodynamic potential of the oxygen evolution reaction (0.6 V vs. SCE). Two arcs can be distinguished for the lower potentials (0 and 0.2 V), at low and high frequencies (on the right and left side of the plot respectively). Near the onset of the photocurrent generation (0 V vs. SCE), where charge transfer resistance is too high to develop any detectable photocurrent, the low frequency arc dominates over the high frequency one. At more anodic potentials, at which photocurrent starts to be noticeable, the low frequency loop decreases for both samples and, in agreement with *J-V* plots, the associated resistance is lower for the 5%-Ti doped sample with respect to the un-doped electrode. At higher potential (0.6 V), the two arcs merge.

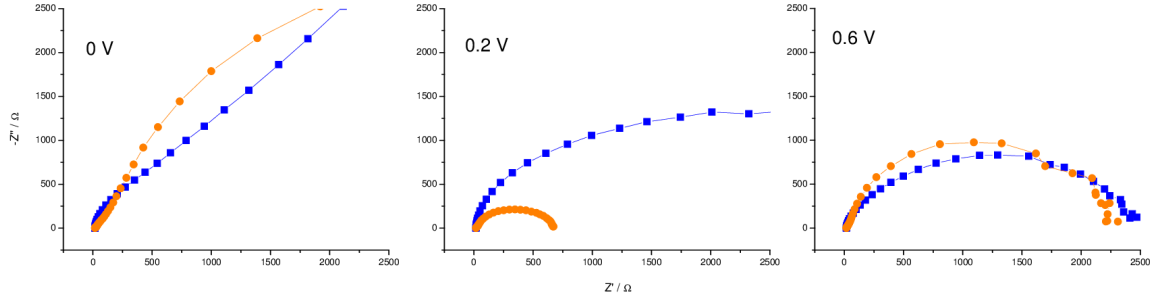

Figure 7.7. Nyquist plots recorded under AM 1.5G illumination in NaOH 0.1 M (pH 13.3) of un-modified (blue squares) and 5%-Ti modified (orange circles) hematite electrodes at different potentials vs. SCE. Fitting with circuital model reported in Figure 7.8-b is represents by the solid lines.

The inverse of R3, that is the resistance associated to the low frequency arc, obtained by the fitting of EIS data, is in excellent agreement with the differential resistance obtained by the derivative of the *J-V* curves ($\frac{\partial J}{\partial V}$) for both the samples (Figure 7.8-a), indicating that the low frequency loop, which models the interface, is the mainly responsible of the photocurrent generation and it is thus associated to hole transfer from surface trap states. The trap capacitances (CPE2) show the expected maximum in correspondence of the minimum reached by the charge transfer resistance (R3) for both the un-modified and modified samples (Figure 7.9). The capacitance shows only a moderate increase in the

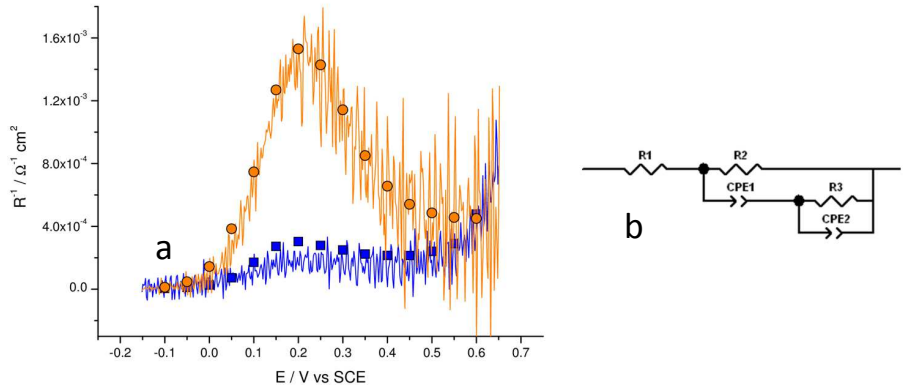

Figure 7.8. (a) Derivatives of the *J-V* curve ($\frac{\partial J}{\partial V}$, solid lines) plot together with the inverse of R3 values (symbols) obtained from the EIS data fitting of the low frequency loop for the un-modified (blue) and 5%-Ti modified (orange) samples. (b) Circuital model used for the EIS data fitting.

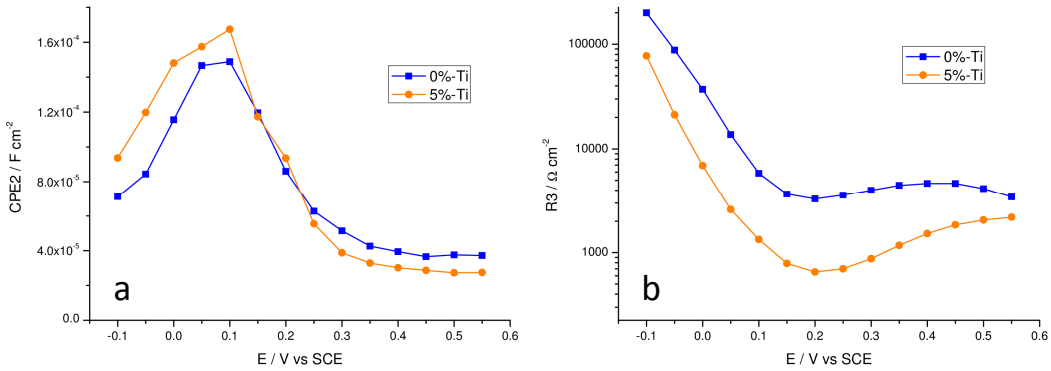

Figure 7.9. (a) CPE2 and (b) R3 plot of un-modified (blue squares) and 5%-Ti modified (orange circles) hematite electrodes recorded under AM 1.5G illumination in NaOH (0.1 M, pH 13.3).

5%-Ti doped sample with respect to the un-modified one (Figure 7.9-a), while in the former a ca. 5-fold reduction associated to the charge transfer resistance occurs (Figure 7.9-b), in agreement with increased photocurrent magnitude observed in the *J-V* curves. Although the slight increase in photogenerated holes capacitance can be explain by a passivating effect of the TiO_2 phase, the important decrease in charge transfer resistance cannot be easily described by such effect, for which an opposite behaviour would be expected due to the insulating nature of TiO_2. It is thus possible that this effect partly arises from better charge transport property of hematite, due to an increase in conductivity. Indeed, high frequency capacitance follows a M-S behaviour from which the doping density can be extracted (Figure 7.10), resulting 3 times higher for the 5%-Ti modified sample with respect to the un-modified hematite ($5.04 \cdot 10^{18}$ and $1.87 \cdot 10^{18}$ cm^{-3} respectively).[25] It is also possible that, at low titanium incorporation percentage, a iron-titanate phase is formed on the hematite surface instead of a pure TiO_2 inducing a cascade of charge transfer processes that reduce charge recombination and enhance photocurrent. According to literature, this mixed oxide phase cannot be clearly detected by XPS giving similarity in B.E. with pure TiO_2.[20] The positive shift of the flat band potential, of the 5%-Ti modified hematite with respect to the un-modified sample, estimable from the intersection with the *x* axis (Figure 7.10), is consistent with the retard photoanodic response which could be observed by exploring the transient *J-V* curve transients in the -0.35 - 0 V vs. SCE interval (Figure 7.11). This feature cannot be explained

with increased donor density, which would implied a negative shift of the Fermi level rather than the observed positive shift. This result could be consistent with the formation of a surface phase with increased dipole momentum resulting in a stabilization of the Fermi level: the presence of this surface dipole may participate to the faster charge transfer kinetic.

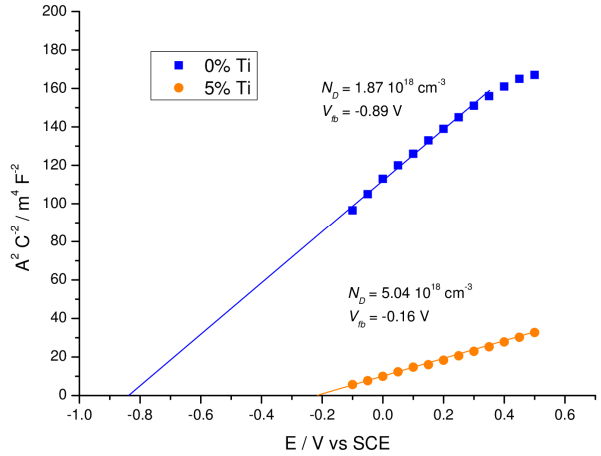

Figure 7.10. Mott-Schottky plot of un-modified (blue squares) and 5%-Ti modified (orange circles) sample recorded at 100 Hz under AM 1.5 G illumination in NaOH 0.1 M (pH 13.3). Fitting lines and extrapolated values of donor density and flat band potential arte reported.

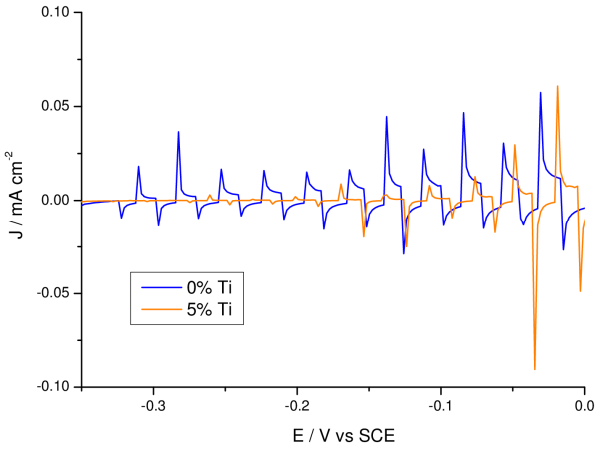

Figure 7.11. Magnification of the *J-V* curves recorded under shuttered illumination of un-modified (blue line) and 5%-Ti modified (orange line) hematite electrodes under AM 1.5 G illumination in NaOH 0.1 M (pH 13.3).

7.6 Conclusions

Modification of the electrophoretic deposition technique by the addition of Ti(IV) butoxide to the iron oxide nanoparticle solution results in improvement of the photoactivity of all the modified electrodes, with the best performance recorded for the 5%-Ti modified sample, which shows a 4-fold photocurrent enhancement with respect to the un-treated electrode reaching ca. 1.0 mA cm^{-2} at 0.65 V vs. SCE in NaOH 0.1 M (pH 13.3). Successive SILAR functionalization with amorphous iron oxide OEC led to photocurrent on the order of 1.5 mA cm^{-2} at the same potential, one of the highest achieved with only solution based procedure and without the addition of precious elements. AFM and XPS morphological investigation reveal the formation of a Ti(IV) containing phase on the hematite surface, with a thickness that depends on the initial amount of the titanium precursor added, that reduces the surface state recombination and enhances the charge transfer rate, rather than modifies the surface states density, as confirmed by EIS analysis. M-S plot testified a 3-fold increase in the donor density in the 5%-Ti modified sample, indicating a better conductivity, which may also contribute to explain the enhanced photoactivity. Thus, Ti(IV) probably plays multiple role, acting both as an interfacial modifier, resulting in improved kinetics, and as a lattice dopant, although this latter role may be secondary with respect to the former.

7.7 References

1 J. A. Glasscock, P. R. F. Barnes, I. C. Plumb and N. Savvides, *J. Phys. Chem. C*, **2007**, *111*, 16477.

2 Y.-S. Hu, A. Kleiman-Shwarsctein, A. J. Forman, D. Hazen, J.-N. Park and E. W. McFarland, *Chem. Mater.*, **2008**, *20*, 3803.

3 Gurudayal, S. Y. Chiam, M. H. Kumar, P. S. Bassi, H. L. Seng, J. Barber and L. H. Wong, *ACS Appl. Mater. Interfaces*, **2014**, *6*, 5852.

4 A. Kleiman-Shwarsctein, Y.-S. Hu, A. J. Forman, G. D. Stucky and E. W. McFarland, *J. Phys. Chem. C*, **2008**, *112*, 15900.

5 P. Kumar, P. Sharma, R. Shrivastav, S. Dass and R. V. Satsangi, *Chemistry of Phytopotentials: Health, Energy and Environmental Perspectives*, **2012**, Springer Berlin Heidelberg, Berlin.

6 J. Liu, C. Liang, G. Xu, Z. Tian, G. Shao and L. Zhang, *Nano Energy*, **2013**, *2*, 328.

7 T.-H. Kim, H. S. Kim, I.-C. Hwang and K. B. Yoon, *Phys. Chem. Chem. Phys.*, **2014**, *16*, 21936.

8 S. Munetoshi, Y. Hiroyasu and T. Hitoshi, *Appl. Phys. Express*, **2012**, *5*, 115801.

9 S. Shen, J. Zhou, C.-L. Dong, Y. Hu, E. N. Tseng, P. Guo, L. Guo and S. S. Mao, *Sci. Rep.*, **2014**, *4*, 6627.

10 G. Wang, Y. Ling, D. A. Wheeler, K. E. N. George, K. Horsley, C. Heske, J. Z. Zhang and Y. Li, *Nano Lett.*, **2011**, *11*, 3503.

11 T. S. Atabaev, M. Ajmal, N. H. Hong, H.-K. Kim and Y.-H. Hwang, *Appl. Phys. A*, *2014*, **118**, 1539.

12 Z. Fu, T. Jiang, Z. Liu, D. Wang, L. Wang and T. Xie, *Electrochim. Acta*, **2014**, *129*, 358.

13 N. T. Hahn and C. B. Mullins, *Chem. Mater.*, **2010**, *22*, 6474.

14 M. Rioult, H. Magnan, D. Stanescu and A. Barbier, *J. Phys. Chem. C*, **2014**, *118*, 3007.

15 C. Miao, T. Shi, G. Xu, S. Ji and C. Ye, *ACS Appl. Mater. Interfaces*, **2013**, *5*, 1310.

16 J. Deng, J. Zhong, A. Pu, D. Zhang, M. Li, X. Sun and S.-T. Lee, *J. Appl. Phys.*, **2012**, *112*, 084312.

17 O. Zandi, B. M. Klahr and T. W. Hamann, *Energ. Environ. Sci.*, **2013**, *6*, 634.

18 R. Franking, L. Li, M. A. Lukowski, F. Meng, Y. Tan, R. J. Hamers and S. Jin, *Energ. Environ. Sci.*, **2013**, *6*, 500.

19 M. G. Ahmed, I. E. Kretschmer, T. A. Kandiel, A. Y. Ahmed, F. A. Rashwan and D. W. Bahnemann, *ACS Appl. Mater. Interfaces*, **2015**, ***7***, 24053.

20 D. Monllor-Satoca, M. Bartsch, C. Fabrega, A. Genc, S. Reinhard, T. Andreu, J. Arbiol, M. Niederberger and J. R. Morante, *Energ. Environ. Sci.*, **2015**, *8*, 3242.

21 S. Hu, M. R. Shaner, J. A. Beardslee, M. Lichterman, B. S. Brunschwig and N. S. Lewis, *Science*, **2014**, *344*, 1005.

22 X. Yang, R. Liu, C. Du, P. Dai, Z. Zheng and D. Wang, *ACS Appl. Mater. Interfaces,* **2014**, *6*, 12005.

23 T. Fujii, F. M. F. de Groot, G. A. Sawatzky, F. C. Voogt, T. Hibma and K. Okada, *Phys. Rev. B*, **1999**, *59*, 3195.

24 J. Augustynski, B. D. Alexander and R. Solarska, *Top. Curr. Chem.*, **2011**, *303*, 1.

25 Details of the extrapolation of the donor density and the flat band potential values from MS plot for electrophoretical hematite electrodes are reported in Chapter 6.

CHAPTER 8

PLD DEPOSITION OF A TRANSPARENT IRON OXIDE CATALYST FOR THE WATER OXIDATION REACTION

8.1 Introduction

A critical issue in the implementation of catalysts with photoactive semiconductors (both for the hydrogen and oxygen production) is the parasitic light blocking effect by catalysts deposited on the absorber surface:[1,2] in the case of metal oxides OEC deposited on photoanodes, the effect of optical losses on the overall efficiency is so severe that in a recent investigation the best performance was obtained with a sub-nanometer film thickness.[3] On the other hand, higher catalyst mass loading is generally beneficial in terms of overpotential performance. This trade-off between optical losses and catalyst loading limits the application of earth-abundant, cheap and scalable alternatives to noble-metal based catalysts, since the replacements generally have lower catalytic activity and higher quantities would be needed to produce comparable performances.[4,5]

In collaboration with Id.E.A. Laboratories of the University of Trento, we decided to take advantage of the versatility of PLD technique to investigate the optical and electrochemical responses of nanosized iron oxide catalyst films to a systematic variation of film morphology, ranging from a low-transmittance compact layer to a porous nanoparticle-assembled coating which resulted to be highly transparent. To demonstrate the potential for application of this approach, we functionalized the surfaces of mesoporous hematite photoanodes with the best catalyst morphologies and studied the photoactivity of the integrated absorber-catalyst with different absorbing materials. Preliminary results pointed out that, in the case of transparent catalyst layer, a two-fold increase in the photocurrent with respect to unmodified hematite is obtained, whereas the compact catalyst layer decreased the response of the integrated absorber-catalyst photoanodes.

As already reported in the previous chapters, the surface functionalization of hematite electrodes with iron(III) hydrous oxides led to a notable improvement of the catalytic activity of the photoanodes towards the water oxidation reaction, confirming the role of these oxides as suitable oxygen evolving catalysts for the photoinduced water splitting process. Apart from the overall good catalytic performances, iron oxides are nontoxic, environmentally safe and based on one of the most earth-abundant elements. In our opinion, these are fundamental aspects to take into account for the future development of a technology dedicated to the sustainable production of fuels from the decomposition of water molecules. For the deposition of the catalyst onto the hematite surface we have previously employed a simple SILAR procedure (Successive Ionic Layer Adsorption and Reaction), consisting on the successive dipping of the electrode first in an iron(III) salt solution and then in aqueous NaOH. This technique is fast and cheap, it requires only common laboratory glassware and it can be easily scaled up to large surfaces. Some disadvantages arise from the difficulty to obtain complete and homogeneous surface coverage, and it also grants no control over morphology of the deposited catalyst. Electrodeposition, which could lead to nanostructured surfaces, suffers from similar problems.[6,7] Photo-chemical metal-organic deposition (PMOD)[8] is also a versatile technique to obtain amorphous metal and mixed-metal oxides by spin coating solutions

of metal–organic precursors followed by UV irradiation. However, the resulting films present smooth and featureless surfaces, whereas a high roughness is generally beneficial in catalysis.

Pulsed Layer Deposition (PLD) is a vapor deposition technique where a high-power pulsed laser beam is focused inside a vacuum chamber to strike a target of the material that has to be deposited: the material is firstly vaporized from the target in a plasma plume of a mixture of vapor/liquid nanodroplets and then it deposits on the substrate. The process can occur also in the presence of a background gas, such as oxygen for the deposition of oxides using metal targets. PLD could present some significant advantages over the methods listed above: (i) precise control of the quantity of the deposited material, (ii) enhanced adhesion due to the energetic nature of the process, and, most importantly, the possibility of nanostructuring the electrode surface by the deposition of nanoparticles.[9-11] Additionally, being essentially a physical deposition method, it is suitable for all kind of substrates because it does not require the immersion of the sample in solution. The main drawback of the PLD technique is the need for specialized equipment, although this is already employed in industrial applications.[12]

8.2 Amorphous iron oxide pulsed laser deposition

Amorphous iron oxides were deposited on commercial quartz and p-type Si substrates (for UV-Vis, Raman and scanning electron microscopy characterization), as well as FTO and mesoporous hematite photoanodes (for electrochemistry and photoelectrochemistry experiments) by means of pulsed laser deposition technique, using a KrF excimer laser (Lambda Physik LP 220i) with an operating wavelength of 248 nm, pulse duration of 25 ns, repetition rate of 20 Hz and laser fluence of 2.0 J cm^{-2}. The deposition chamber was evacuated up to a base pressure of 10^{-4} Pa, then oxygen gas was backfilled into the chamber through a mass flow controller. Deposition was performed at a constant pressure of 45 Pa. The distance between the iron disc and substrates was set to 5.5 cm and the number of pulses was fixed (2000 pulses), to ensure that all samples

have the same quantity of material. Substrate temperatures were either room temperature (RT) or 300°C (DEP-300°C). A more detailed description of the pulsed laser deposition apparatus is available elsewhere.[13] For comparison, some samples were deposited at room temperature and then annealed at 300°C and 550°C in air in a tubular furnace. These are labelled AN-300°C and AN-550°C respectively. The heating rate was set to 10 °C min^{-1} and the desired temperature was kept constant for two hours.
Mesoporous hematite film (MPH) was deposited using the electrophoretic procedure described in Chapter 6.

8.3 Morphological investigation

SEM analysis of RT samples revealed a complex morphology with scattered particles of diameter in the range of ca. 30 - 300 nm, randomly distributed on the surface covered by a porous structure made of smaller particles assembled in irregular wires (Figure 8.1-a). As the size of these latter particles approaches the spatial resolution of the SEM apparatus (2 nm), a conservative estimation for their average diameter is 5 ± 2 nm. It is not possible to define a layer thickness due to the high rough morphology, although the coverage seems to be complete (Figure 8.1-b).
Annealing of RT at 300 °C (AN-300°C) results in a partial collapse of the porous structure by aggregation of the smaller particles (Figure 8.2-b), which becomes complete with

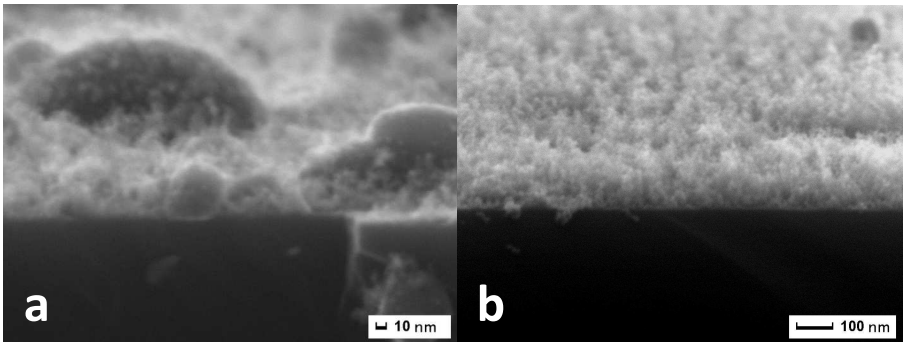

Figure 8.1. Cross-section SEM analysis of samples RT deposited on Si substrate at different magnifications.

annealing at 550°C (AN-550°C, Figure 8.2-c). Deposition on the substrate heated at 300 °C (DEP-300°C) results in a more compact nanoparticles assembled layer (Figure 8.2-d and 8.3-b), due to the higher kinetic energy and thus higher mobility of the particles when they hit the heated substrate, leading to aggregation and the formation of bigger and partially-fused particles, mostly of diameter > 10 nm.

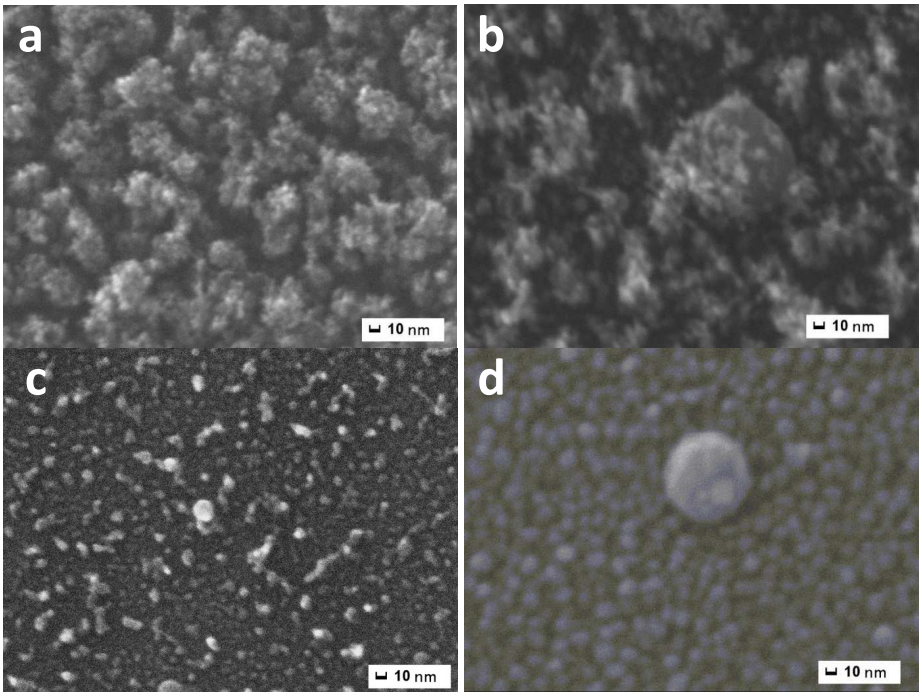

Figure 8.2. Top view SEM images of: (a) RT, (b) AN-300 °C, (c) AN-550 °C and (d) DEP-300°C.

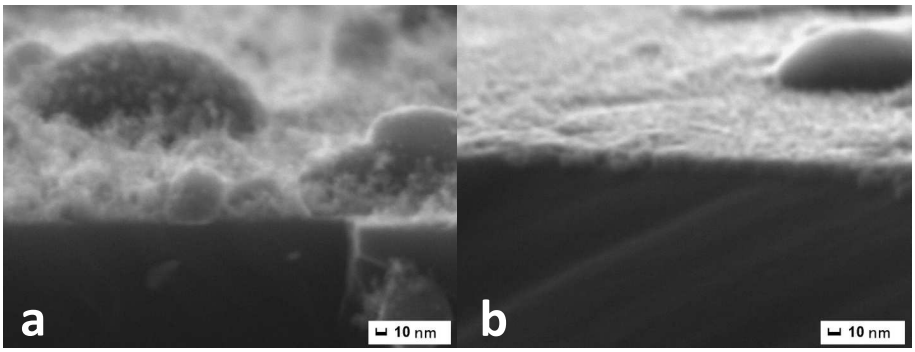

Figure 8.3. Cross-section SEM images at same magnification of (a) RT and (b) DEP-300 °C samples.

Raman analysis (Figure 8.4) reveals the presence of the crystalline hematite main peaks at 226 and 292 cm^{-1} [14] only in the case of the sample annealed at 550°C. All other samples show spectra with features not clearly different from the FTO reference. This is an indication of the largely amorphous nature of the deposited material, which is known to yield better OER catalysis performances than the crystalline phase.[8] In all cases XPS analysis shows binding energies (Fe (2p) peak; BE = 710.2 ± 0.5 eV (Figure 8.4) which are consistent with oxidation states of the Fe_2O_3 stoichiometry. Thus, locally, the films display a chemical composition similar to hematite, but, with the exception of AN-550°C, they lack long range order typical of well crystallized phases, resulting in a poor Raman response.

8.4 Optical quantum confinement effect

From the analysis of UV-Vis absorption spectra on quartz substrates (Figure 8.5-a), three important observations emerge: (i) the sample DEP-300°C shows a much higher absorbance in all the investigated range; (ii) the absorbance correlates with morphology

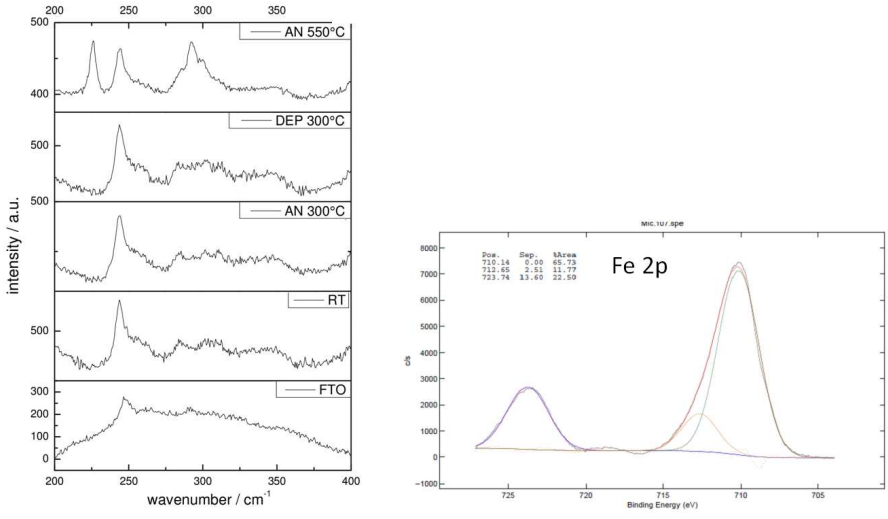

Figure 8.4. (left) Raman spectra of samples on FTO substrates. (right) XPS peaks for Fe (2p) of RT sample.

in the direction of higher values for more compact films and (iii) the absorption band edge is markedly blue-shifted for RT, as more evident in the normalized spectra in Figure 8.5-b. Given that the quantity of deposited material at a given pressure is essentially set by the number of pulses, which is kept constant for all depositions, the difference between RT and DEP-300°C is all the more striking. The reason for this behavior probably lies in the different morphology of the films. While DEP-300°C is essentially a bi-dimensional thin-film, although with a nanostructured surface, RT exhibits a tridimensional architecture with scattered big particles and a substantial fraction of the material composed of very small particles (5 ± 2 nm). In this latter case, a reasonable hypothesis, supported by the blue-shift of the absorption onset, is that a size effect in the form of optical quantum confinement dominates the optical properties, as reported for other materials[15] and for other nanosized hematite.[16,17] A recent investigation observed a remarkable blue-shift of up to 0.3 eV for both direct and indirect transitions when decreasing an hematite film thickness from 20 to 4 nm, leading to an high degree of transparency in the visible region.[18] The effect is size-dependent and ascribed by the authors to quantum confinement. While reducing hematite dimensions to this level could help alleviate the problem of a very short hole-diffusion length, lying in the nanometer range,[19] the resulting low absorption is an issue in the design of photoactive devices based on a single material. On the other side, this feature can be used for the synthesis of catalytic species coupled with photoactive materials, where the absorption of light of the former has to be avoided to not interfere with the absorption of the photoactive material.

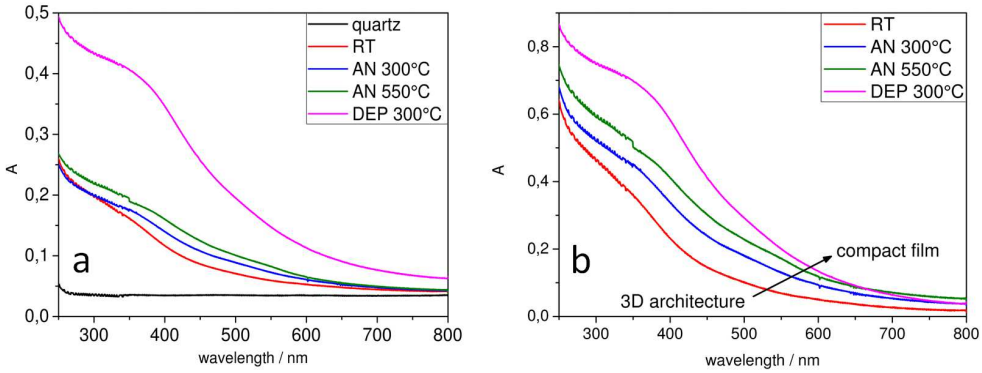

Figure 8.5. (a) UV-Vis absorption spectra on quartz substrates and (b) normalized version.

8.5 Electrochemical characterization of iron oxide samples

Since Fe_2O_3 is stable in alkaline environment (pH > 9.8),[20] electrochemical water oxidation experiments were performed at pH 14 (1 M KOH) to ensure a well defined electrochemistry. Oxygen evolution at this pH is expected at potential:

$$E^0_{O_2/H_2O} = 1.23 - (0.059 \times pH) = 0.40V \text{ (}vs.\text{ RHE)} \quad [21] \qquad (8.1)$$

Figure 8.6-a illustrates the current responses of all iron-modified samples along with an FTO reference. The linear scan reveals that all samples are active towards water oxidation, with both DEP-300°C and AN-300°C showing considerable electroactivity with overpotentials of 408 and 433 mV, respectively (taken at current density J = 0.2 mA cm^{-2}). However, the current response of RT decreased considerably after 1 hour of constant potential applied of 1 V vs. RHE, designed to test stability closer to operational conditions (Figure 8.6-b). The current density loss for RT is of 44%, while DEP-300°C is substantially stable with only a 6% loss. AN-300°C shows an intermediate stability with a 11% decrease, close to the 10% of AN-550°C. In the case of RT, the performance degradation is irreversible and is due to detachment of active material, as observed by SEM images taken after prolonged electrocatalysis (Figure 8.7). Conversely, the initial performance of AN-300°C was restored after rinsing the electrode with abundant water and heating at 80 °C in air for 2 hours, as can be observed from *J-V* experiments (Figure 8.7). In this case, the current decrease during electrolysis may originate by adsorption of molecular oxygen, of ions or oxidation intermediates, limiting the active surface of the electrode, rather than by detachment of material from the electrode. From an electrocatalytic point of view, DEP-300°C is the best electrode, with J = 41.2 mA cm^{-2} at 1.7 V vs. RHE, while AN-550°C is limited to 36 mA cm^{-2} at same potential value, confirming that the amorphous material is a better catalyst than crystalline hematite, as reported by recent literature.[8,22]

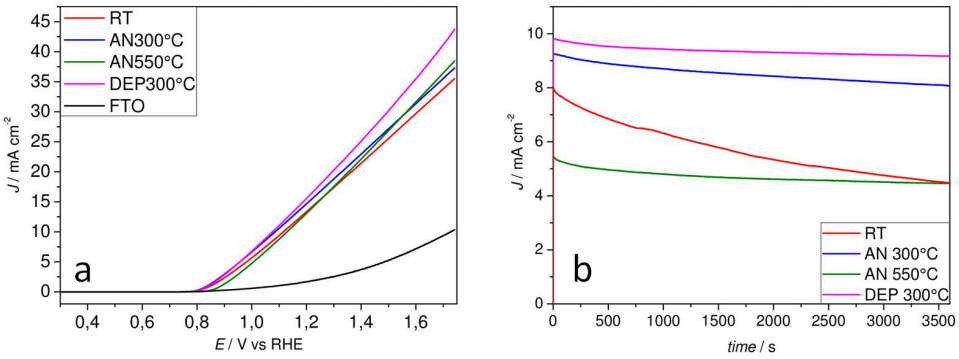

Figure 8.6. (a) *J-V* curves and (b) chronoamperometries at 1 V vs. RHE of iron samples deposited on FTO recorded in 1 M KOH (pH 14). *J-V* are recorded with a rate speed of 10 mV s^{-1}.

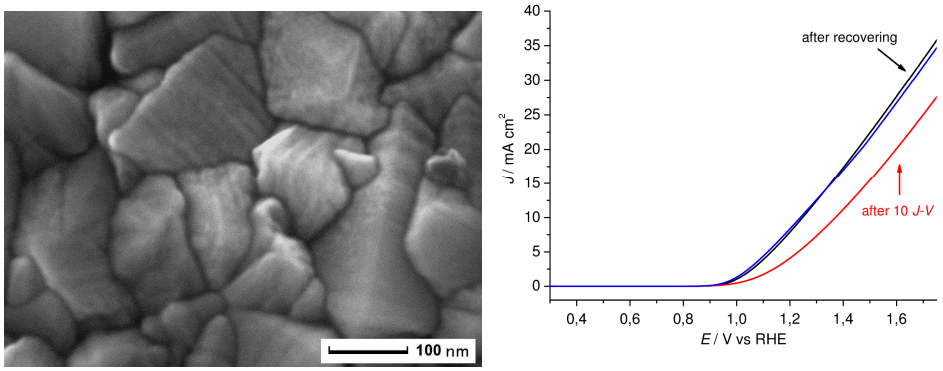

Figure 8.7. (left) Top-down SEM imaging of RT sample after 1 hour of electrocatalysis at 1 V vs. RHE. The morphology is typical of FTO and no nanostructures ascribable to iron oxide are present. (right) Initial *J-V* response of AN-300°C in 1 M KOH (blue), after 10 scans (red) and after restoring the electrode (black).

8.6 Hematite photoanodes modififed with PLD-deposited iron oxides

These findings indicate that the more compact iron oxide assembled film of DEP-300°C is a better electrocatalyst, due to both a higher stability and improved performance. However, when integrated over a mesoporous hematite photoanode (MPH) the effect on the photocurrent is detrimental, partlially due to light losses through the catalyst film. However the ca. 200 mV anodic shift of the photocurrent onset and a slowly rising *J-V* characteristic are also indicative of slow charge transfer or increased electron/hole recombination (Figure 8.8-a). By contrast, functionalization with AN-300°C,

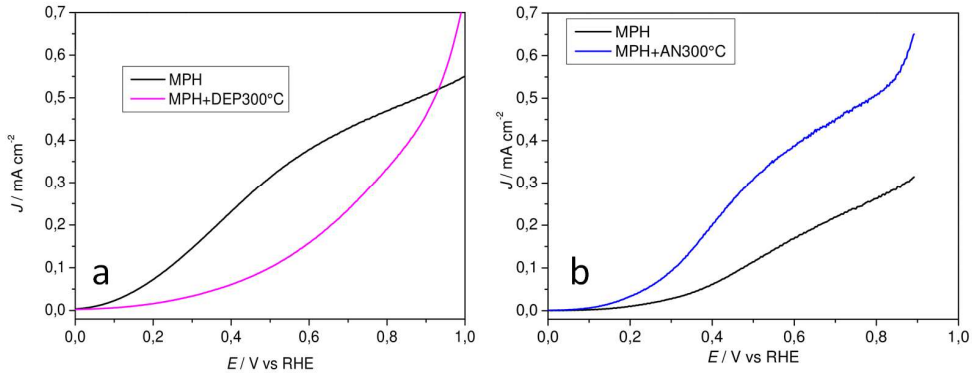

Figure 8.8. Photocurrent response of mesoporous hematite photoanode modified with (a) DEP-300°C and (b) AN-300°C in 0.1 M NaOH (pH 13.3) under AM 1.5G illumination (100 mW cm^{-2}).

selected as the best compromise between stability and transparency, leads to a ca. 25% increase in photocurrents in all the explored range (Figure 8.8-b). The steeper increase in photoanodic current in the presence of the quantum sized catalyst compared to the decreased response in the presence of DEP-300°C may suggests that, differently from the compact DEP-300°C film, the former may form an adaptive junction with the semiconductor, where changes in the Fermi level of the porous catalysts are prevalently assisted by movement of charge compensating ions.[23]

8.7 Conclusions

Reducing the dimensions of an iron oxide catalyst to induce optical quantum confinement is proved to be a feasible strategy to obtain transparent coatings, which retains their activity but are unstable under long-term electrocatalytic conditions. A simple low-temperature thermal treatment was found to improve their stability, enabling the successful application of these catalyst coatings to hematite photoanodes, resulting in a substantial increase in the photocurrents registered in a photoelectrochemical cell. By contrast, functionalization of the photoanodes with a more compact catalyst thin-film, exhibiting better stability and performances in electrocatalysis together with an higher absorbance, leads to a decrease in the photocurrents. These findings offer a strategy to

circumvent the problem of parasitic light absorption in integrated absorber-catalyst photoelectrodes, currently limiting the development of solar water splitting devices, and opens up the possibility to employ higher mass-loadings of catalyst, which would be beneficial especially for earth-abundant, cheap and scalable materials, such as iron oxides.

Further work will be aimed at investigating more in details if the different morphology of the catalysts affects only the absorption properties of the hematite film or if there is also a modification in the charge transfer dynamics at the semiconductor surface. Another issue to solve is the low stability of the most transparent RT structures without resorting to the post-deposition thermal treatment, e.g. by exploring deposition temperatures lower than 300 °C. Finally, we would like to extend the methodology to more intrinsically-active species, like mixed-metal oxides, that have shown excellent electrocatalytic properties towards the water oxidation reaction.[8]

8.8 References

1 S. Y. Reece, J. A. Hamel, K. Sung, T. D. Jarvi, A. J. Esswein, J. J. Pijpers and D. G. Nocera, *Science,* **2011,** *334*, 645.

2 J. R. McKone, N. S. Lewis and H. B. Gray, *Chem. Mater.,* **2014,** *26*, 407.

3 L. Trotochaud, T. J. Mills and S. Boettcher, *J. Phy. Chem. Lett.* **2013,** *4*, 931.

4 E. J. Popczun, J. R. McKone, C. G. Read, A. J. Biacchi, A. M. Wiltrout, N .S. Lewis and R. E. Schaak, *J. Am. Chem. Soc.,* **2013,** *135*, 9267.

5 J. R. McKone, B. F. Sadtler, C. A. Werlang, N. S. Lewis and H. B. Gray, *ACS Catal.,* **2013,** *3*, 166.

6 G. Zotti, G. Schiavon, S. Zecchin and U. Casellato, *J. Electrochem. Soc.,* **1998**, *145*, 385.

7 R. Schrebler, K. Bello, F. Vera, P. Cury, E. Munoz, R. del Rio, H. Gomez Meier, R. Cordova and E. A. Dalchiele, *Electrochem. Solid-State Lett.,* **2006**, *9*, C110.

8 R. D. Smith, M. S. Prevot, R. D. Fagan, Z. Zhang, P. A. Sedach, M. K. Siu, S. Trudel and C. P. Berlinguette, *Science,* **2013,** *340*, 60.

9 T. Warang, N. Patel, A. Santini, N. Bazzanella, A. Kale, A. Miotello, *Appl. Catal. A,* **2012**, *423-424*, 21.

10 M. E. Shaheen, J. E.; Gagnon and B. J. Fryer, *J. Appl. Phys.,* **2013**, *114*, 083110.

11 Q. Guo, S. Wangzhou, F. Liu, M. Arita, Y. Ikoma, K. Saito, T. Tanaka and M. Nishio, *J. Alloys Compd.,* **2013**, *552*, 1.

12 M. C. Gower, *Opt. Express,* **2000**, *7*, 56.

13 M. Bonelli, C. Cestari and A. Miotello, *Meas. Sci. Tech.,* **1999,** *10*, N27.

14 A. M. Jubb and H. C. Allen, *ACS Appl. Mater. Interfaces*, **2010**, *2*, 2804.

15 D. Raymand, T. J. Jacobsson, K. Hermansson and T. Edvinsson, *J. Phy. Chem. C,* **2012,** *116*, 6893.

16 K. Sivula, R. Zboril, F. Le Formal, R. Robert, A. Weidenkaff, J. Tucek, J. Frydrych and M. Grätzel, *J. Am. Chem. Soc.*, **2010**, *132*, 7436.

17 L. Vayssieres, C. Sathe, S. M. Butorin, D. K. Shuh, J. Nordgren and J. Guo, *Adv. Mater.,* **2005,** *17*, 2320.

18 M. Fondell, T. J. Jacobsson, M. Boman and T. Edvinsson, *J. Mater. Chem. A,* **2014,** *2*, 3352.

19 B. Klahr, A. B. Martinson and T. W. Hamann, *Langmuir*, **2011**, *27*, 461.

20 V. Cristino, S. Berardi, S. Caramori, R. Argazzi, S. Carli, L. Meda, A. Tacca and C. A. Bignozzi, *Phys. Chem. Chem. Phys.,* **2013**, *15*, 13083.

21 R. van de Krol, *Photoelectrochemical Hydrogen Production*, Springer US, **2012**, Boston.

22 R. D. Smith, M. S. Prevot, R. D. Fagan, S. Trudel and C. P. Berlinguette, *J. Am. Chem. Soc.,* **2013,** *135*, 11580.

23 F. Li and S. W. Boettcher, *Nature Mater.,* **2014**, *13*, 81.

CHAPTER 9

CHARACTERIZATION TECHNIQUES: EXPERIMENTAL DETAILS AND THEORETICAL ASPECTS

9.1 Electrochemical and photoelectrochemical setup

All AC/DC electrochemical and photoelectrochemical measurements have been performed at atmospheric pressure and ambient temperature in a three electrodes configuration cell (Figure 9.1) using an Eco Chemie Autolab PGSTAT 302/N electrochemical work-station. The working electrode (WE) was the hematite photoanode, clamped directly to a copper wire using a portion of the bare FTO: to ensure a good electric contact, usually aluminium tape was employed to cover the portion of the clamped FTO. A platinum electrode was used as counter electrode (CE) and a saturated calomel electrode, SCE, as the reference (RE).

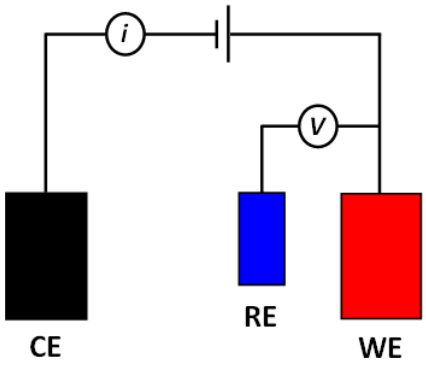

Figure 9.1. Three-electrode setup for electrochemical and photoelectrochemical measurements.

With this setup, the current flows between the CE and the WE. The potential across the electrochemical interface at the WE is measured with respect to the RE and it is equal to the potential difference specified by the user. The necessity to use a reference electrode is determined by the impossibility to know where the interfacial potential difference occurs when the external bias is changed in a two electrode configuration (WE and CE): it might be on both electrodes and not at the one under examination (i.e. WE). The cell employed was a glass cuvette with a square geometry open at the top. Different electrolytes have been tested using always deionized water as solvent (NaOH, KOH, Na_2CO_3, sodium borate buffer, $K_4[Fe(CN)_6]$, $K_3[Fe(CN)_6]$): concentrations and pH values are specified in the text. Only the portion of the WE covered with the hematite film was immersed in the solution and, if not specified, the electrode was illuminated from the hematite side (e.g. front side) and the active area was 1 cm^2. Experiments under illumination were performed using an ABET solar simulator equipped with an AM 1.5G filter and the illumination power output on the electrode was calibrated to be 100 mW cm^{-2} (1 sun of illumination) using a digital Agilent power-meter. When the applied potential is reported vs. the Reversible Hydrogen Electrode (RHE) the conversion from the SCE values follows Equation 9.1.

$$E_{RHE} = E_{SCE} + 0.059(V) \times pH + 0.241V \qquad (9.1)$$

9.2 DC photoelectrochemical techniques

To characterize the performance of the photoanodes, the current density as a function of potential in the dark and under illumination was measured (*J*-*V* curve) by linearly scanning the bias region between the open circuit voltage under illumination and potential values at which the thermal current rose up at a scan speed of 20 mV s^{-1}: scans were repeated until stabilization of the current. Being hematite a n-type semiconductor, the current associated with the oxidation of water (Faradaic process) arises with the increasing of the potential in the positive direction (i.e. anodic): photoinduced anodic current involves the transfer of photo-generated holes from the semiconductor to the solution.

Monochromatic *J*-*V* curves were recorded using a monochromatic illuminated light source generated by an applied photophysics monochromator (10 nm bandwidth) coupled to a 175 W Xe lamp (Luxtel) with a spot illuminated area on the electrodes of 0.2 cm^2.

Shuttered *J*-*V* curves were recorded while illumination was turned on and off using an Oriel manual shutter, in order to gain qualitative information about the dynamics of water oxidation and charge recombination at the hematite/electrolyte interface. Briefly, when light reaches the sample, photogenerated holes travel to the SCLJ and accumulate because of the slow OER kinetics or because they are trapped mainly in surface states. This induces a sharp anodic current spike that decays as the accumulation process perturbs the charge distribution of the space charge region until equilibrium is eventually reached between water oxidation and charge recombination (stable current): large anodic spikes are thus indication of high degree of recombination on the semiconductor surface. Conversely, the cathodic transient peak observed when the light is turned off is assigned to electrons diffusing from the external circuit and recombining with the accumulated holes at the SCLJ. The appearance of transients diminishes at higher potential as a larger

proportion of holes have sufficient potential to oxidize water and a qualitatively evaluation of the rectifying properties of different samples can be done by the comparison of the magnitude of the anodic spikes (Figure 9.2).

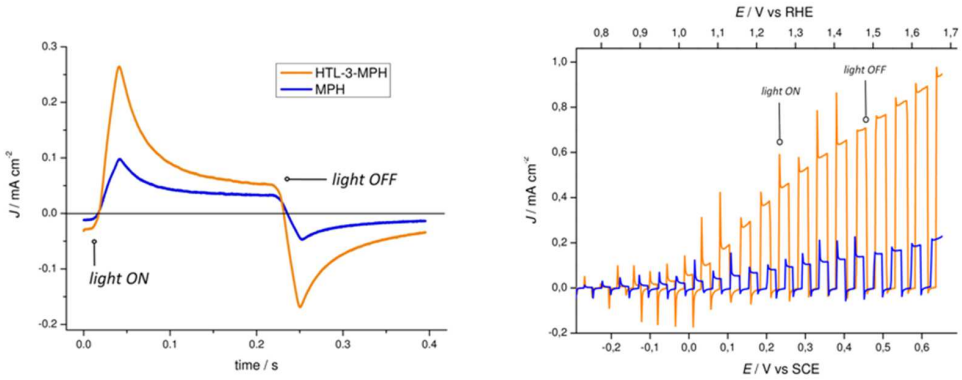

Figure 9.2. Examples of photocurrent transients of different hematite samples recorded at (left) constant potential of 0 V vs. SCE and (right) during a linear potential scan.

Chronoamperometry was employed to asses the stability of the sample under the operating conditions, recording the photocurrent under constant illumination and constant potential bias, typically applied for time > 4 hours. No stirring was used during the experiments to dissipate the bubbles generated on the hematite surface.

9.3 Photoaction spectra: IPCE and APCE

Another approach to measure the performance of a photoanode (or a PEC cell) is to determine the photocurrent as a function of wavelength: a common figure of merit is the Incident Photon-to-Current Conversion Efficiency (IPCE), that represents the number of photogenerated electron per number of incident photons (Equation 9.2). Photoaction spectra report IPCE% values vs. the wavelength of the monochromatic incident light.

$$IPCE\% = \frac{n°electrons}{n°photons}\% \qquad (9.2)$$

IPCE is obtained by the following equation:

$$IPCE = \frac{hc}{e}\frac{J_\lambda(\mu A cm^{-2})}{\lambda(nm)P_\lambda(Wm^{-2})} = 1.24\times10^{-3}(Vm)\frac{J_\lambda(\mu A cm^{-2})}{\lambda(nm)P_\lambda(Wm^{-2})} \quad (9.3)$$

where J_λ is the photocurrent density obtained under monochromatic irradiation and λ (nm) and P_λ (W m^{-2}) are, respectively, the wavelength and the irradiance, respectively, of the external monochromatic light.

The IPCE is also given by:

$$IPCE = \varphi_{c.g.}\eta LHE \quad (9.4)$$

where:

- $\varphi_{c.g.}$ is the charge generation efficiency;
- η is the electron collection efficiency, i.e. the ability to extract electrons from the photoanode;
- *LHE* is the Light Harvesting Efficiency ($1-10^{-A(\lambda)}$) and depends on the intrinsic ability of the material to absorb light at a certain wavelength.

So, ideally, a material that is able to avoid recombination and thus to efficiently separate electron and holes after their photogeneration, should have IPCE% values close to 100% in a spectral region where its absorbance is > 1. This means that all the photons that the material absorbs are converted in an equal number of electrons that are extracted from the electrode to generate current: the same number of holes are thus transferred to the solution. In the previous chapters, maximum IPCE values for modified hematite electrodes do not exceed 25%: thus, 75% of the electrons photogenerated are lost by recombination (considering a unitary LHE for hematite at ca. 400 nm).

The apparatus for the measurement of the IPCE is composed by a 150 W Xenon lamp (LX), coupled with a heat reduction system to avoid superheating of the lamp over long periods. The light passes first through a monochromator (M) to select the required

wavelength and then through a collimating lens (L) that focuses the light in a squared spot of 0.2 cm^2 onto the semiconductor surface (S). The incident monochromatic irradiance was measured with a calibrated silicon photodiode (Centronic ASD100-7Q). The photoanodic current was recorded every 10 nm from 350 and 600 nm on a PGSTAT 30 electrochemical workstation (A/V) at a fixed applied potential (Figure 9.3).

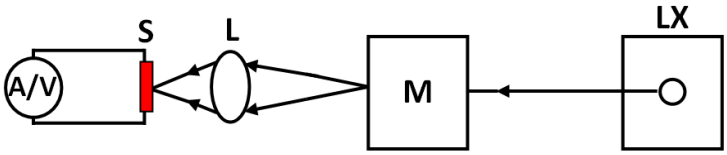

Figure 9.3. Scheme of the apparatus to record IPCE spectra.

IPCE data can be converted in APCE according to:

$$APCE\% = \frac{IPCE\%}{1 - 10^{-A(\lambda)}} \tag{9.5}$$

where *A(λ)* is the background subtracted absorbance. The APCE spectra, being normalized for the LHE, describe the ability of a material to achieve a better charge separation and collection efficiency independently of the amount of light absorbed.

9.4 AC technique: Electrochemical Impedance Spectroscopy

Electrochemical Impedance Spectroscopy (EIS) has become in the years a powerful tool in the study of corrosion, semiconductors, and batteries. EIS experiments provide data on both electrode capacitance and charge-transfer kinetics, giving valuable mechanistic information. The main advantage of EIS is the possibility to use a purely electronic model to represent an electrochemical cell: an electrode interface undergoing

an electrochemical reaction is typically analogous to an electronic circuit consisting of specific combinations of resistors and capacitors. Taking advantage of this analogy, it is possible to use the established AC circuit theory to characterize the electrochemical system in terms of its equivalent circuits. In practice, the correlation of an impedance plot obtained for a given electrochemical system with one or more equivalent circuits provides information for the verification of a particular mechanistic model for the system, correlating physical properties with circuit elements and extracting numerical values by fitting the data to the circuit model.

As a modulation technique, EIS consists of applying a time-dependant signal to the electrode, usually a sinusoidal perturbation of bias potential, and measuring the current through the cell. The electrode dark- or photo- current density is typically recorded while applying a modulated voltage signal, with frequency f (0.01 Hz < f < 100 MHz), superimposed on the bias potential. The excitation signal is usually a small potential (ca. 1 - 10 mV), so that the cell response is pseudo-linear: the current response to a sinusoidal potential will be a sinusoid at the same frequency but shifted in phase. By varying the excitation frequency, processes with different time constants can be resolved. Electrochemical cells are not linear: in fact, doubling the voltage will not necessarily double the current, but they can be consider pseudo-linear focusing on a small portion of the *J-V* curve (Figure 9.4). The further analysis of the frequency-dependent response using an electronic model can separate the different aspects of charge transport, charge trapping, and charge transfer at the interface with the electrolyte.

The excitation signal, expressed as a function of time, has the form:

$$E_t = E_0 \sin(\omega t) \tag{9.6}$$

where E_t is the potential at time t, E_0 is the amplitude of the signal and ω is the angular frequency, related to the frequency expressed in hertz (f) by:

$$\omega = 2\pi f \tag{9.7}$$

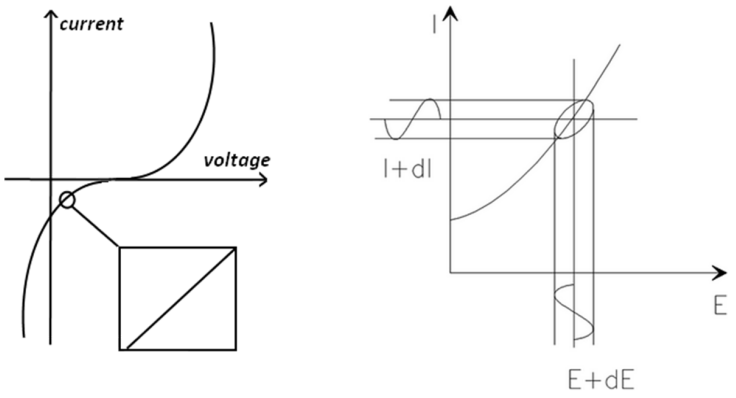

Figure 9.4. (left) Current vs. voltage curve showing pseudo-linearity for little potential perturbation. (right) Graphical interpretation of the "Lissajous Figure".

In a linear system, the response signal, I_t is shifted in phase (φ) and has a different amplitude than I_0

$$I_t = I_0 \sin(\omega t + \varphi) \tag{9.8}$$

The term *impedance (Z)* denotes the opposition to the flow of electrons and so, in analogy to Ohm's law, it can be written as:

$$Z = \frac{E_t}{I} = \frac{E_0 \sin(\omega t)}{I_0 \sin(\omega t + \varphi)} = Z_0 \frac{\sin(\omega t)}{\sin(\omega t + \varphi)} \tag{9.9}$$

Reporting the sinusoidal signal E_t on the x-axis of the *J-V* plot and the sinusoidal response I_t on the y-axis, the result is an oval known as "Lissajous Figure" (Figure 9.4), the first accepted method for impedance measurements.

Using the Euler's relationship:

$$e^{i\varphi} = \cos\varphi + j \sin\varphi \tag{9.10}$$

the impedance can be also represented as a complex number:

$$Z(\omega) = Z_0 e^{j\varphi} = Z_0(\cos\varphi + j\sin\varphi) \tag{9.11}$$

(*j* is used by electrochemists instead of *i* to define $\sqrt{-1}$ to avoid confusion with the current symbol *i*).

Impedance represents thus a more general concept of the resistance defined by the classical Ohm's law: in AC circuits, also capacitors and inductors impede the flow of electrons through the circuit rather than resistors. Let us consider, for example, a simple circuit composed by a resistor in series with a capacitor represented in Figure 9.5.

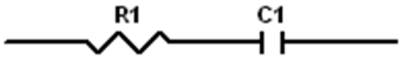

Figure 9.5.

The total impedance of the circuit (Z_{tot}) is given by the sum of the single contributions, Z_R and Z_C for the resistor and the capacitor respectively (Figure 9.6-a).

$$Z_{tot} = Z_R + Z_C = R - jX_C \tag{9.12}$$

where *R* is the classic Ohm resistance and X_C is the capacitive reactance. Notice that the impedance of a resistor is equal to the resistance value: it is independent from frequency and it has no imaginary component because there is no phase-angle shift between the voltage and the current flowing through the resistor (Figure 9.6-b). With only a real impedance component, the current through a resistor stay in phase with the voltage across the resistor. Capacitors have instead only an imaginary impedance component because the current through a capacitor is phase shifted by 90 degrees with respect to the voltage, as can be demonstrated from Equation 9.13 (Figure 9.6-c). The capacitors impedance decreases as the frequency is raised. The impedance of elements in parallel is instead the inverse of the sum of the inverse of impedances.

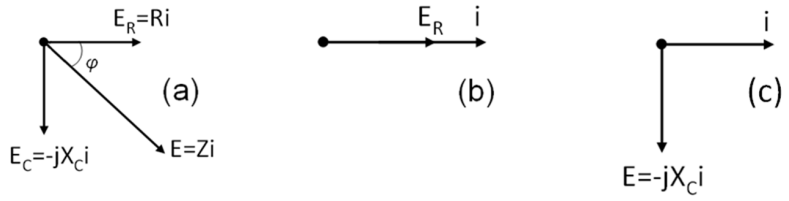

Figure 9.6. Vector representation of the relation between the applied potential and the flowing current (a) in the circuit represented in Figure 9.5, (b) in a resistor and (c) in a capacitor. In a resistor, the phase angle between the potential applied and the current is 0 degrees, so the two vectors are coincident. In a capacitor, the angle is 90 degrees and, reporting the current on the x-axis, the capacitive vector has an imaginary part for convention because coincident with the y-axis.

$$i = C\frac{dE}{dt} = C\frac{d(E_0 \sin(\omega t))}{dt} = \omega C \cos(\omega t) = \frac{E}{X_C}\sin(\omega t + \frac{\pi}{2}) \qquad (9.13)$$

A common way to plot impedance data is the Nyquist plot, where the real part of the impedance is plotted on the x-axis while the imaginary part is plot on the y-axis. In this plot, the y-axis is negative and each point corresponds to the impedance at one frequency. The major shortcoming of this representation is that looking at it is not possible to know at which frequency corresponds a single data point. The Bode plots allow to gain this kind of additional information by plotting the logarithm of the frequency on the x-axis and both the absolute values of the impedance ($|Z|=Z_0$) and the phase-shift angle (φ) on the y-axis. In Figure 9.7 are reported Nyquist and Bode plots for a circuit comprised of a resistor and a capacitor in parallel are reported.

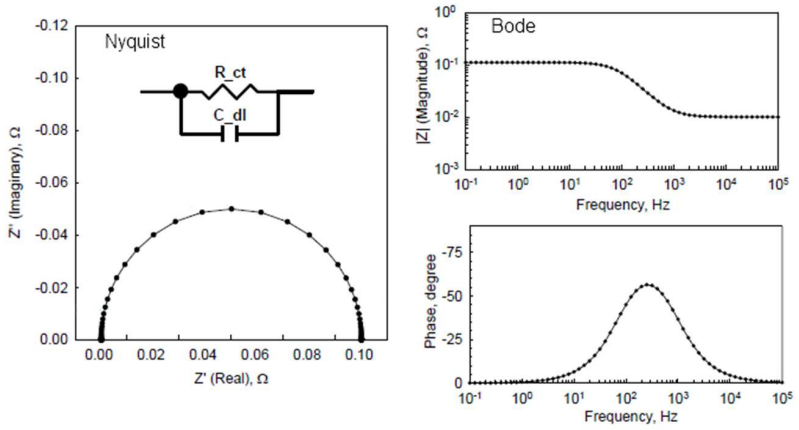

Figure 9.7. Nyquist and Bode plots for the indicated RC circuit.

Once an experiment is complete, the raw data at each frequency measured consist of the real and imaginary component of both the voltage applied and the current generated. From these data it is possible to compute the phase shift (φ) and the total impedance (Z) for each applied frequency, as well as many other impedance functions. An important step in the elaboration process is the choice of the correct circuital model that well describes the system under investigation and then the interpretation of the values related to physical and chemical properties of the system. EIS measurements are usually repeated for different applied potential values to describe the system under operating condition of a PEC cell, that's said potential values at which charge transfer are active both under dark and illumination condition. Although the single circuital elements have a detailed mathematical description, the physical interpretation of these values, and so the association between the different interfaces of the PEC device and the elements of the circuit selected, is probably the most challenging part of the experiment. The physical description of the most common circuital elements are listed below.

- Resistor (R): it can be associated to limitation of electronic conductivity inside the bulk of the material, resistance to the polarization at values different to the open circuit voltage, charge transfer through interfaces and also resistance due to the solution or to the set-up employed for the measurements.
- Capacitor (C): it represents the charge accumulation at the interfaces where a double layer is formed.
- Constant Phase Element (CPE): it represents an interface that acts as a non-ideal capacitor showing a strong dependence to the frequency; this behaviour is probably due to high porosity or non-homogeneity of a surface that generate charge dissipation processes that are not described by an ideal capacitor.
- Warburg element (W): it describes diffusive phenomena inside the solution of red-ox species that are generated on the working electrode.

One fundamental application of EIS technique is the determination of V_{fb} and N_d values of the semiconductor under examination by plotting the inverse of the square of the

capacitance, extrapolated from the fitting, versus the potential applied under dark condition using the well-known MS equation (see Chapter 2.5).

In the studies reported in this thesis, potentiostatic impedance data of photoanodes in the dark and under illumination condition were recorded in the three electrode configuration cell described above in NaOH (0.1 M, pH 13.3). Sample data were obtained from -0.2 to 0.6 V vs. SCE at 50 mV intervals employing a FRA2.v10 frequency response analyzer controlled by Nova 1.10. A 10 mV amplitude sinusoidal perturbation (single sine), whose frequency ranged between 100 000 and 0.01 Hz was adopted. The impedance response was fitted using ZView software with the electric equivalents reported in the discussion section.

9.5 Optical absorption and emission spectroscopy

UV-Visible spectra were recorded with a Cary 300 UV-Visible spectrophotometer (Agilent Technologies) in the 350-750 nm region with a home-made glass support for the electrodes. FTO glass was used as reference sample. Thickness of hematite films can be indirectly evaluated by the absorption of visible light knowing the light penetration depth (α^{-1}) at a certain wavelength.

Photoluminescence spectra were recorded with an Edinburgh Instrument FS920 spectrofluorometer equipped with a 900 W Xe arc lamp as excitation source in the visible region with a 10 nm bandwidth. Solid thin films, placed on dedicated film holders were excited at 520 nm. The emission intensity was optimized by adjusting the angles between the sample, the excitation and the analysis beams, by acting on a micromechanical stage. Emission spectra were averaged over 10 scans and subtracted in order to eliminate spurious contributions arising from Raman scattering. With fluorescence spectroscopy is possible to study deactivation radiative processes by monitoring the emission spectra after the excitation with a proper light. In hematite, the reduction of the amount of

surface trap states results in an enhancement of photoluminescence, since these states behave as non radiative recombination centres of excitons.

9.6 Nanosecond laser flash photolysis

Nanosecond laser flash photolysis is a spectroscopic technique used for time-resolved emission and absorption measurements in a time window from 6-8 ns up to ms. A schematic representation of the apparatus is given in Figure 9.8. Experiments on hematite thin films were carried out with a nanosecond spectrometer based on a Continuum Surelite II NdYAG laser source (355 nm, 20 mJ/cm^2/pulse) and on a pulsed Applied Photophysics Xe lamp which generated the white light analysis beam. Electron/hole recombination kinetics were found to be substantially unchanged within an excitation energy interval of 5-20 mJ/cm^2/pulse. At present, with our spectrometer, 5mJ/cm^2/pulse represents the lower limit for obtaining well defined transients having a reasonable S/N ratio.

The analysis beam passed through the sample, which was immersed in 0.5 M sodium borate buffer solution (pH 11.5) and oriented at a 45° with respect to the probe, before being focused on an Acton SpectraPro 2300i monochromator (50 lines/mm) equipped with a Hamamatsu R3896 phototube. A 420 nm cut off filter was used to avoid UV irradiation of the sample and a 532 nm notch filter prevented scattered laser light to reach the detector. Oscillographic traces were acquired on a LeCroy 9360 oscilloscope, averaged over 10 laser shots and transferred to a PC. A custom made LabVIEW program controlled laser firing, pulse synchronisation and data acquisition.

The transient spectra of either unmodified and Fe-OEC modified hematite electrodes (active surface = 4 cm^2) were measured both in the absence and in the presence of potential bias by using an Autolab PGSTAT 101 controlled by Nova 1.10. In order to avoid interference with the optical path, electrochemical experiments were performed in two electrode configuration by using a thin platinum wire as a counter electrode. The JV curve measured before and after the time resolved measurements were unchanged within the

experimental errors, indicating the absence of electrode degradation even after several hundreds laser shots.

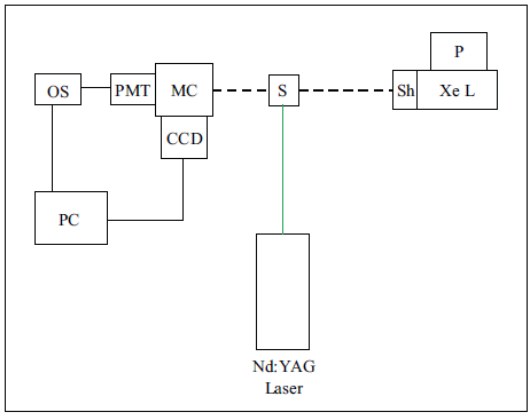

Figure 9.8. Schematic layout of the Nanosecond Laser Flash Photolysis setup: green line, excitation beam; black dashed line, white light probe beam; Xe L, xenon arc lamp; P, Xe lamp pulser; Sh, shutter; S, sample; MC, monochromator, PMT, photomultiplier tube; CCD, CCD camera; OS, oscilloscope; PC, personal computer.

9.7 Investigation of morphology and crystalline structure

Scanning electron microscopy (SEM) was used to analyze the morphology and thickness of films. The surface of the films was analyzed by a JEOL JSM-7001F field effect gun (FEG-SEM) apparatus at 20 keV beam energy. SEM apparatus is equipped with an Energy Dispersive X-ray Spectroscopy detector (EDXS, Oxford INCA PentaFETx3). Working Distance (WD) was maintained between 3 to 8 mm. Surface morphology images were acquired in top-down and tilted mode whereas cross section analysis were performed putting the films on a 90° stub. Energy dispersive x-ray analysis (EDS) was performed in line-scan mode on two different sections of MPH sample before and after 800°C annealing. The beam energy was 15 KeV and the working distance 10 mm.

X-Ray Diffraction (XRD) analysis were carried out with a Philips X'Pert $\theta/2\theta$ optimized for thin films measurements having an incident grazing angle of 1.0°.

Diffractograms were collected with the Cu K_α radiation (λ=1.5416 Å) in the 2θ interval 5°-90° with a 0.02° step (2θ) and an acquisition time of 25 s/step.

Micro-Raman spectroscopy measurements were performed on a Horiba LabAramis setup equipped with a HeNe 633 nm laser as source and a confocal microscope coupled to a 460 mm-focal length CCD-based spectrograph equipped with a PC-controlled four interchangeable gratings-turret. In the range between 450 nm and 850 nm, the wavenumber accuracy is 1 cm^{-1} with the 1800 l/mm grating. The laser power is 15 mW and the maximum spot size is 5 µm. Accumulation number ranges from 10 and an exposure time of 7 s were employed for all measurements except for HTL-1 and its FTO reference, where the exposure time was 10 s and the accumulation number 30.

AFM topographical investigation was performed with a Nanoscope III Scanning Probe Microscope (Digital Instruments) equipped with a silicon tip (model RTESP, resonant frequency 300 KHz) and operated in tapping mode with a scan rate of 1 Hz, 512 points resolution and scanned area of 5 × 5 µm.

XPS was performed using a PHI 5000 VersaProbe II equipped with a mono-chromatic Al Ka (1486.6 eV) X-ray source and a hemispherical analyzer. Electrical charge compensation was required to perform the XPS analysis. The sample surface was sputtered for 30 sec in order to remove any surface oxidation.

9.8 Determination of roughness factor

Roughness factor (RF) of HTL-3, MPH and HTL-3-MPH samples (Chapter 6) was calculated as the ratio between the real surface area and the geometric area of the electrode (1 cm^2). The real surface area has been determined by the absorption of the azo-dye Orange II.[1,2] The electrodes (with the bare FTO portion cover with Kapton tape) were immersed for 15 minutes in a Orange II water solution (1.5 mM, pH 3.5) and then washed with NaOH (1.5 mL, 1 M). The concentration of the dye absorbed onto the film was obtained by measuring the optical density at 454 nm. Considering that at the operating conditions the Orange II dye is expected to form a monolayer on the iron oxide

surface occupying an area of 40 nm^2 per dye molecule, the RF factor calculated is 15 for HTL-3, 25 for HTL-3-MPH and 25 for MPH on FTO.

9.9 List of materials employed in the samples preparation

Chapter 5. FTO glass slides (Fluorine-doped Tin Oxide, TEC 8 Ω cm^{-2}, Hartford Glass), $FeCl_3 \cdot 6H_2O$ (>99%, M.W. 270.3 g mol^{-1}, Sigma Aldrich), $NaNO_3$ (99.5%, M.W. 84.99 g mol^{-1}, Carlo Erba), NaOH (98%, M.W. 40.00 g $mol^{-}1$, Alfa Aesar), deionized water.

Chapter 6. FTO glass slides, $FeCl_3 \cdot 6H_2O$, Polyethyleneglycol Bisphenol A Epichlorohydrin Copolymer (mol wt 15000-20000 Da, Sigma Aldrich), anhydrous sodium acetate (≥98%, M.W. 82.03 g mol^{-1}, Sigma Aldrich), iodine (≥99.8%, M.W. 253.81 g mol^{-1}, Sigma Aldrich), Orange II sodium salt (4-(2-Hydroxy-1-naphthylazo)benzenesulfonic acid sodium salt, dye content ≥85%, M.W. 350.32 g mol^{-1}, Sigma Aldrich), HCl (37%, Sigma Aldrich), EtOH (≥99.8%, Sigma Aldrich), acetone (≥99.5%, Sigma Aldrich), deionized water.

Chapter 7. FTO glass slides, $FeCl_3 \cdot 6H_2O$, titanium(IV) butoxide (97%, M.W. 340.32 g mol^{-1}, density 1 g mL^{-1}, Sigma Aldrich), anhydrous sodium acetate, iodine, EtOH, acetone, deionized water.

Chapter 8. FTO glass slides, quartz substrate (Sigma Aldrich), p-type Si substrate (Sigma Aldrich), metallic iron disc (purity 99.9%, Sematrade), $FeCl_3 \cdot 6H_2O$, anhydrous sodium acetate, iodine, EtOH, acetone, deionized water.

9.10 References

1 J. Bandara, J. A. Mielczarski and J. Kiwi, *Langmuir*, **1999**, *15*, 7670.

2 A. Kay, I. Cesar and M. Grätzel, *J. Am. Chem. Soc.*, **2006**, *128*, 15714.

APPENDIX A

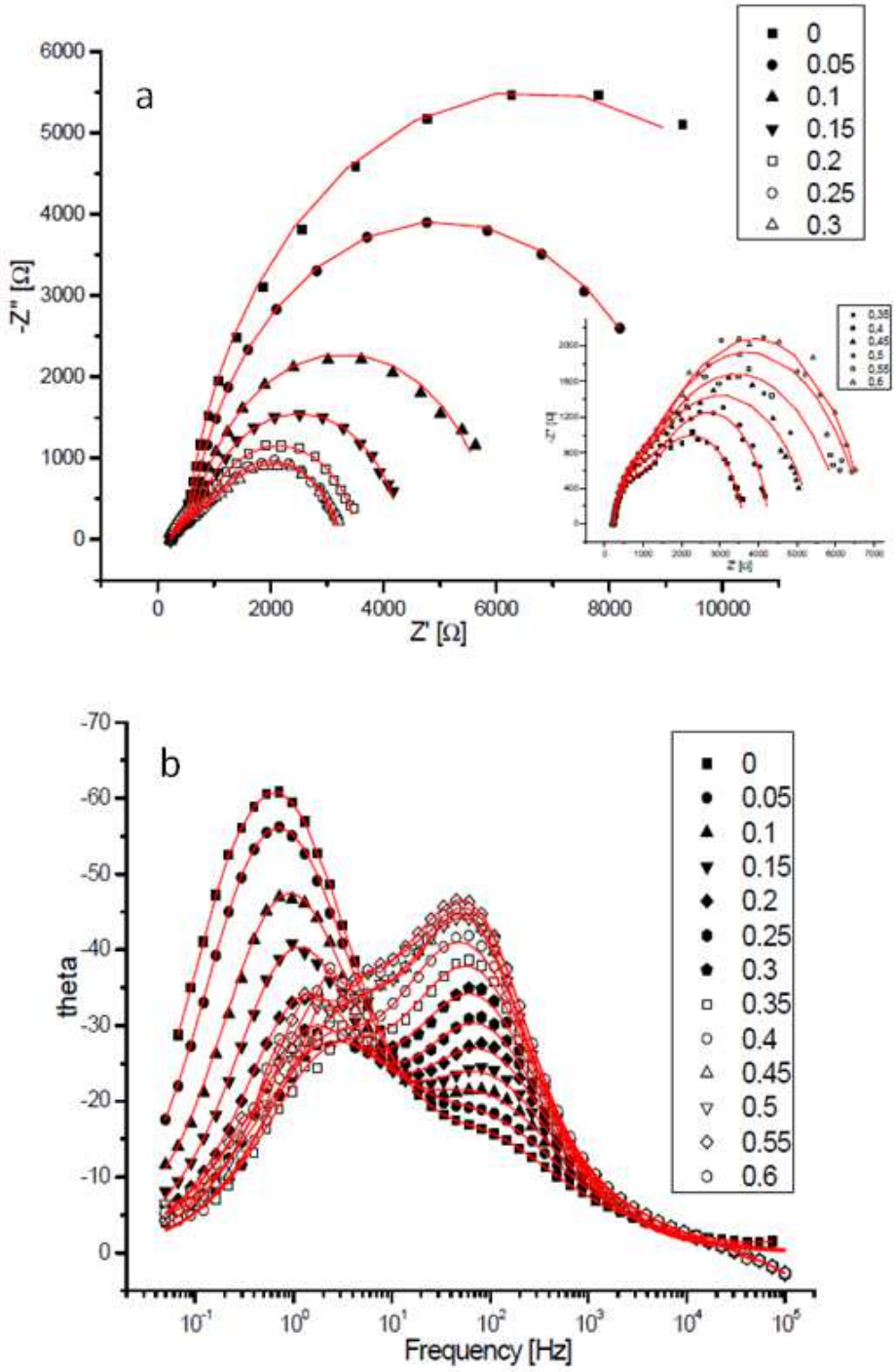

Figure A1. Fitted Nyquist (a) and Bode (b) plots of hematite electrode recorded at 50 mV intervals in the range 0 - 0.6 V vs. SCE in 0.5 M sodium borate buffer (pH 11.5) under AM 1.5G illumination (100 mW cm^{-2}). Inset Figure A1-a: complex plane plots in the 0.4-0.6 V vs. SCE range.

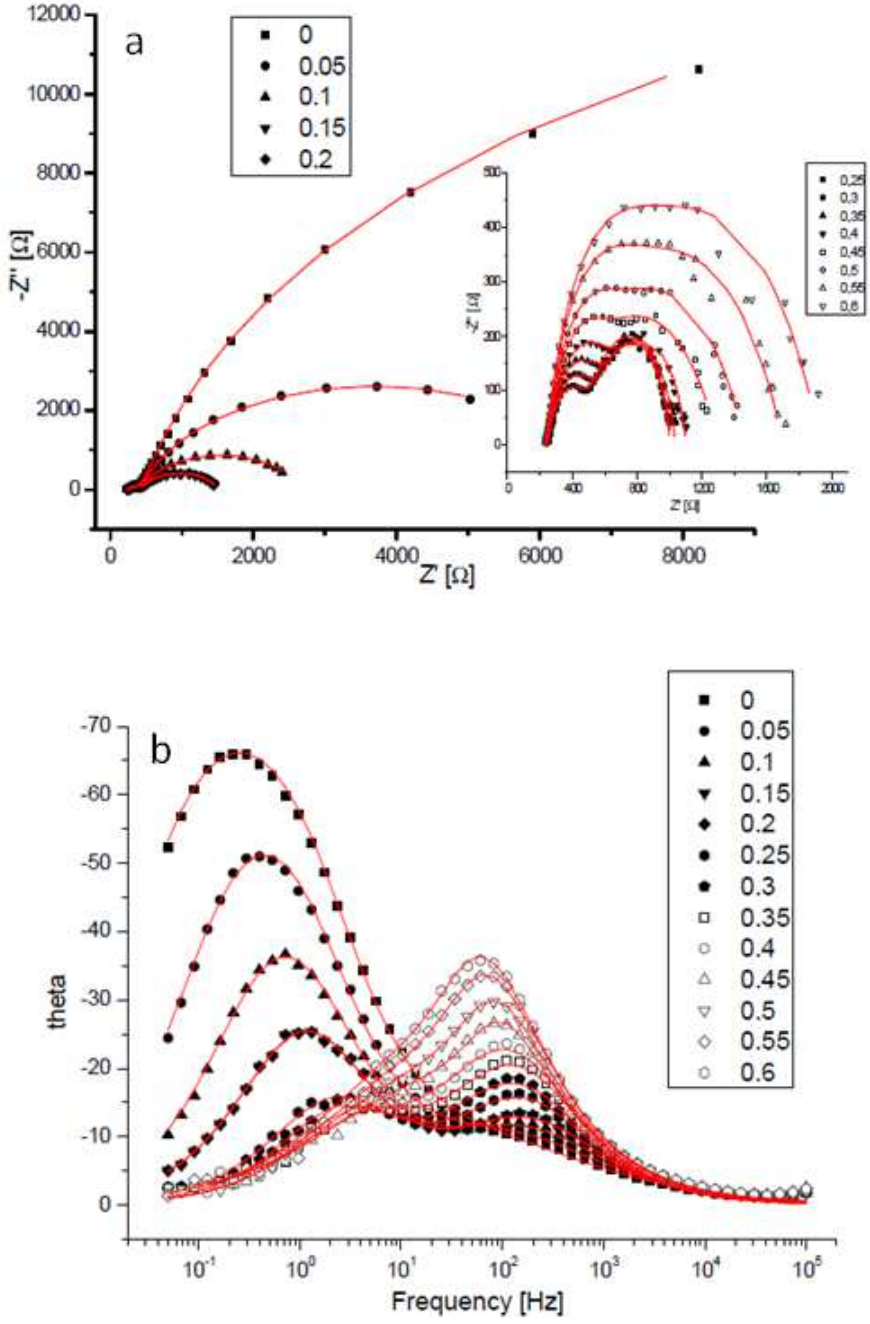

Figure A2. Fitted Nyquist (a) and Bode (b) plots of the hematite electrode of Figure A1 after surface modification with Fe-OEC recorded at 50 mV intervals in the range 0 - 0.6 V vs. SCE in 0.5 M sodium borate buffer (pH 11.5) under AM 1.5G illumination (100 mW cm^{-2}).

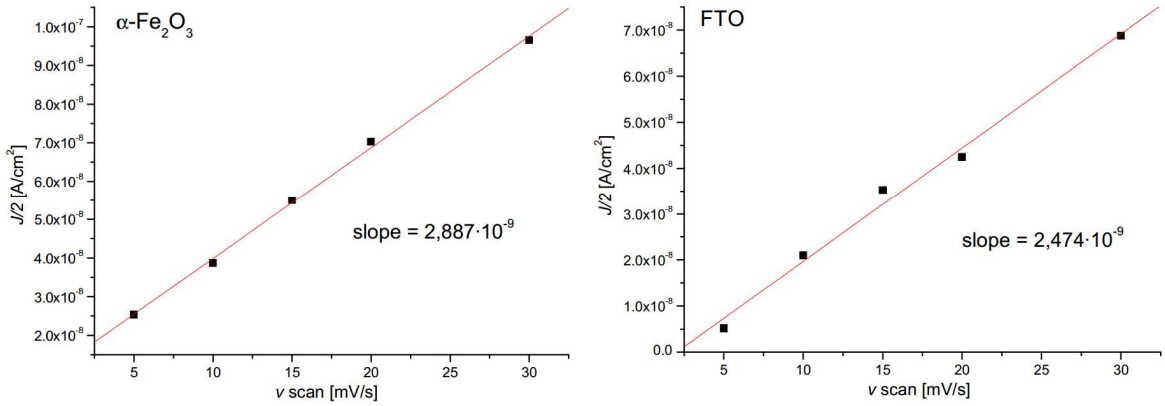

Figure A3. Capacitance of hematite electrode compared to an equivalent FTO electrode (annealed at 800 °C) measured at 0.4 V vs. SCE in the dark .

The capacitance was calculated from the faradic current density according to

$$\frac{J}{2} = C \cdot \frac{dV}{dt} = C \cdot v_{scan} \qquad \text{A1}$$

According to Equation A1 the capacitive current is linear with the scan speed, providing C as a slope. A potential at which no dark faradic process was observed (0.4 V vs. SCE) was selected for this evaluation. It can be observed that both the hematite electrode and the bare FTO provide a very similar capacitance as can be expected in a case where the space charge capacitance C_{sc} is significantly smaller than the capacitance of the Helmholtz layer. Given that

$$\frac{1}{C_{TOT}} = \frac{1}{C_{SC}} + \frac{1}{C_{SC}} \approx \frac{1}{C_{SC}} \quad \text{if } C_{SC} << C_H \qquad \text{A2}$$

The value of capacitance extracted from CV experiments ($2.88 \cdot 10^{-6}$ F cm^{-2}) is in excellent agreement with the capacitance calculated by EIS in the dark at 1 Hz at 0.4 V vs. SCE (indicated by the arrow in Figure A4, $2.94 \cdot 10^{-6}$ F cm^{-2}). Note that even under illumination essentially the same capacitance was obtained at the same voltage.

From the comparison between the FTO and hematite capacitance, the surface area of the photoanode can be estimated in 1.17 times the FTO one.

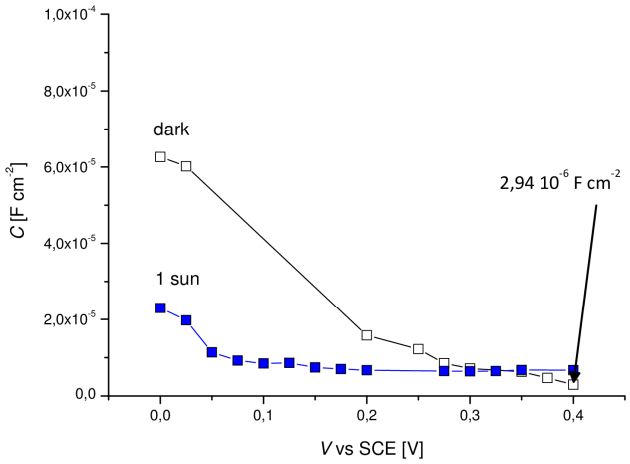

Figure A4. Capacitance of hematite electrode measured in the dark at 1 Hz (empty squares) and under AM 1.5 G illumination (blue squares in 0.5 M sodium borate buffer (pH 11.5). For the data under illumination, maximum capacitance corresponding to the maximum of the first semicircle in the Nyquist plot.

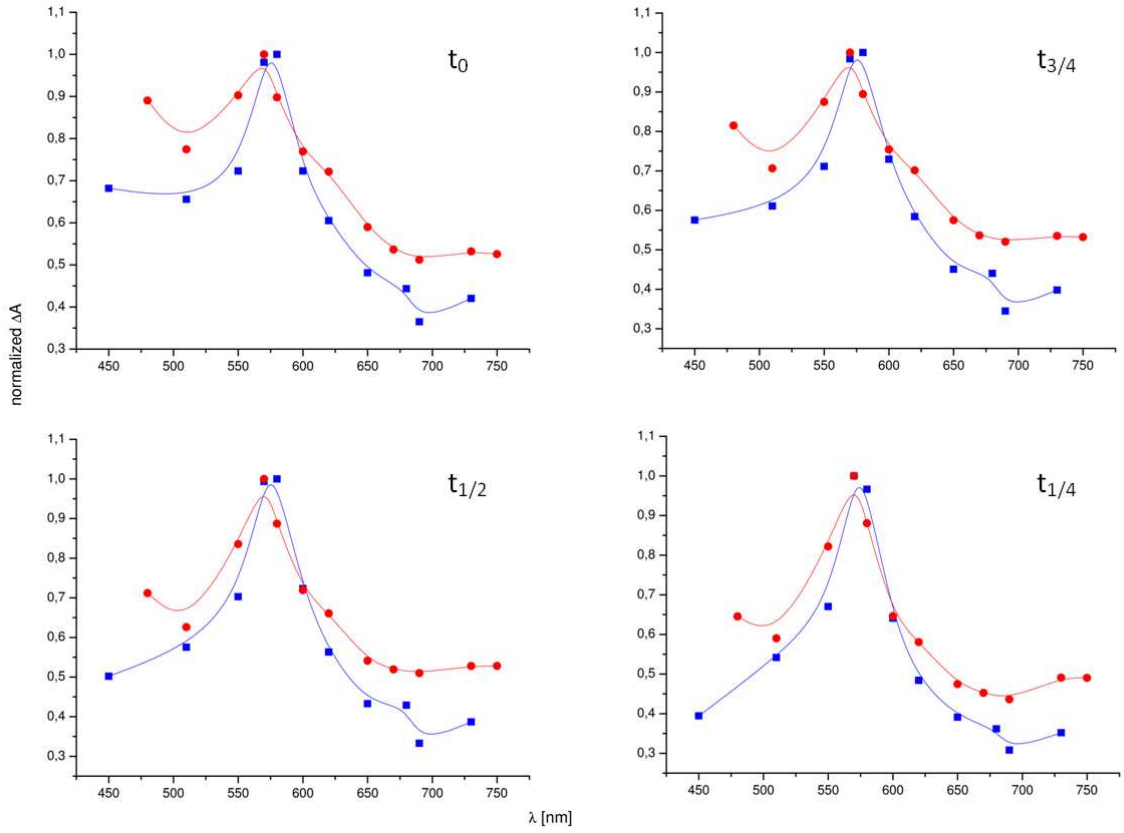

Figure A5. Comparison between the transient normalized differential absorption spectra of hematite (blue squares) and Fe-OEC modified hematite (red circles) under 0.7 V vs. SCE bias in 0.5 M sodium borate buffer (pH 11.5).

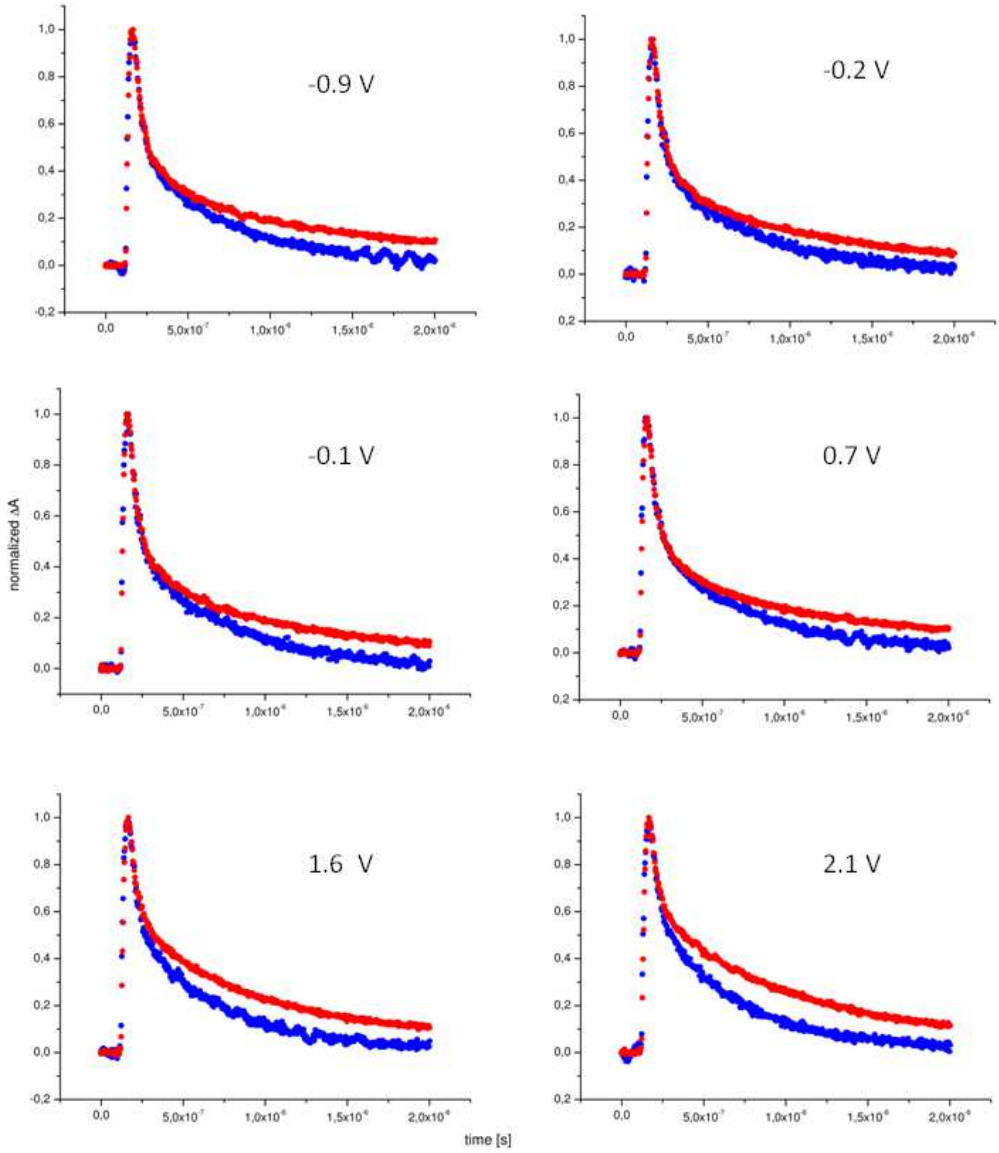

Figure A6. 580 nm differential absorption decays for unmodified hematite (blue symbols) and Fe-OEC modified hematite (red symbols) recorded in the presence of increasingly positive potential bias (vs. SCE) in 0.5 M sodium borate buffer (pH 11.5).

APPENDIX B

Table B1. Analysis of the reproducibility of the thickness of HTL samples measurement with the cross-section SEM analysis. Measurements were taken at a minimum of 3 and a maximum of 5 different locations along the film section. Outliers have not been discarded when calculating Standard Deviation.

Sample	Number of measurements	AverageThickness	Standard Deviation
1	22	14	1.2
2	11	19	1.1
3	18	32	6.2
4	17	40	7.1

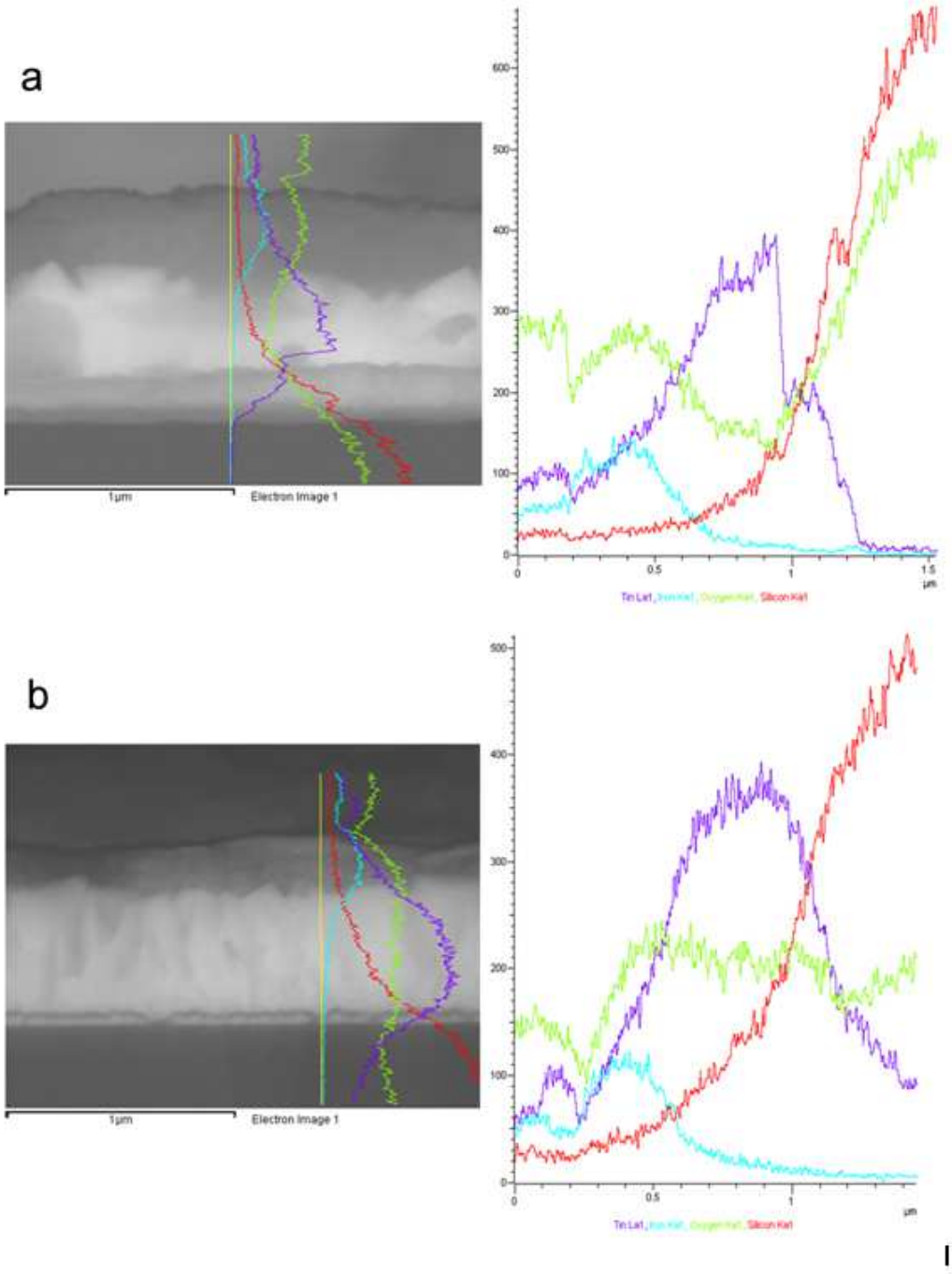

Figure B1. Cross sectional energy dispersive analysis (EDS) of MPH sample (a) before and (b) after 800 °C annealing. The FTO/glass interface can be identified between 0.9 and 1.1 µm and the hematite/FTO interface between 0.5 and 0.7 µm. The interface air/hematite, the actual surface, lies at about 0.1-0.2 µm.

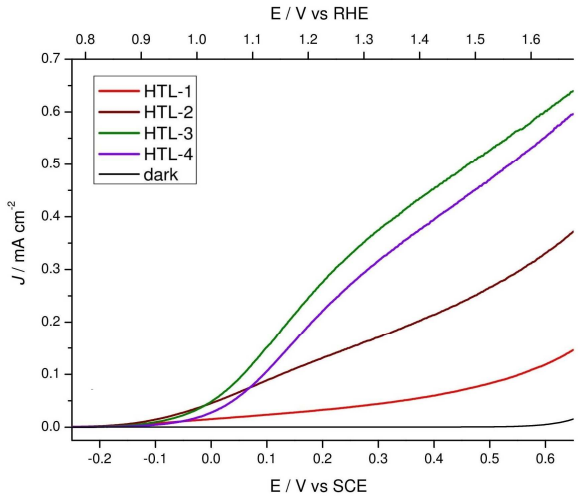

Figure B2. *J-V* curves under continuous illumination of HTL-1 to -4 samples in NaOH 0.1 M (pH 13.3).

APPENDIX C

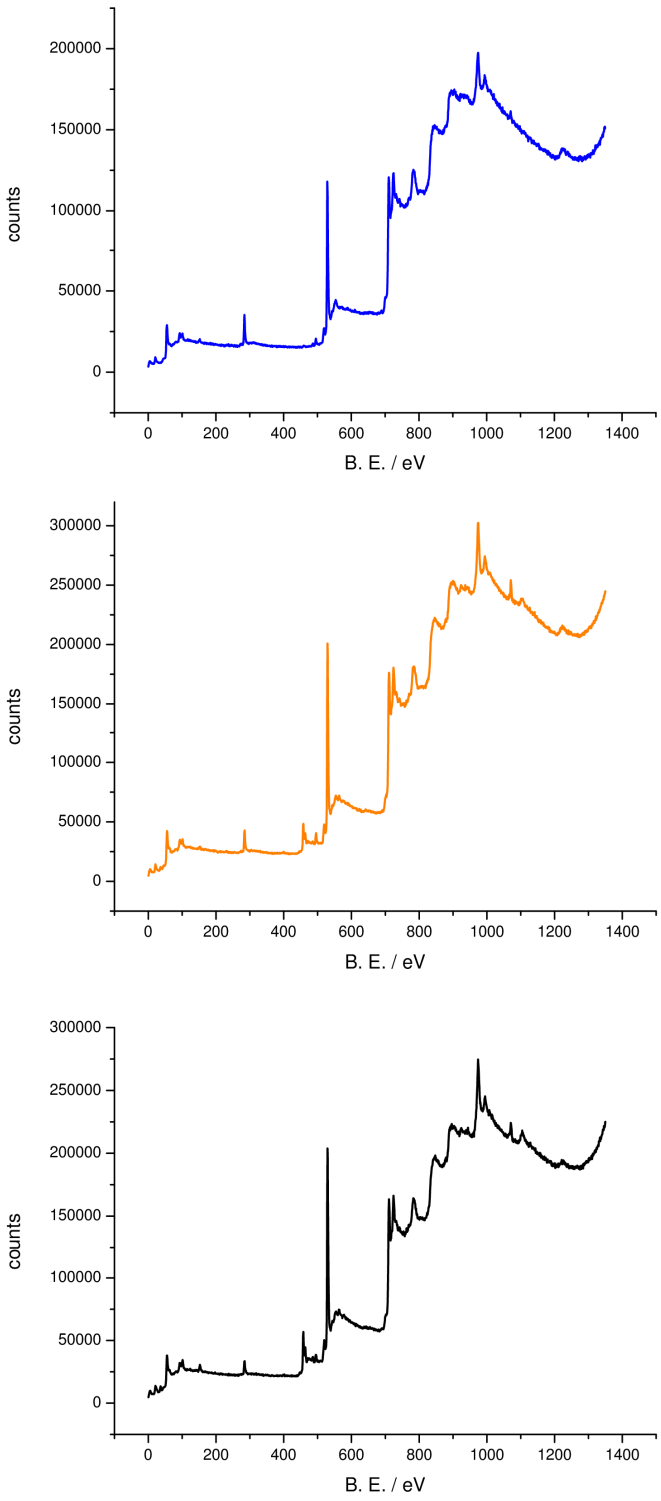

Figure C1. XPS survey spectra of un-doped (blue), 5%-Ti (orange) and 10%-Ti doped (black) hematite samples. Note in the first spectra the absence of signals around 460 eV, diagnostic of the presence of a titanium phase.

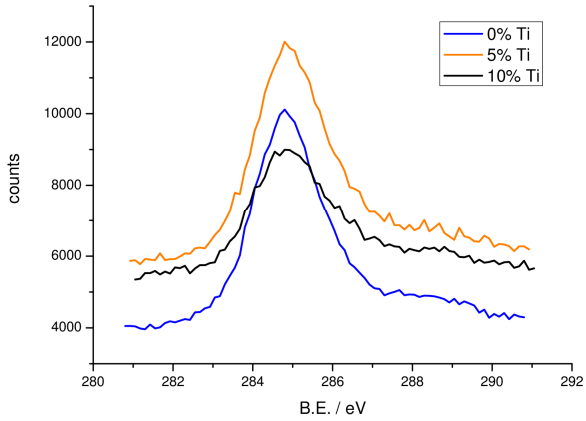

Figure C2. C 1s core level XPS spectra for un-doped and Ti-doped hematite films.